DISSERTATION

COLD POOL PROPAGATION AND COLD POOL-LAND SURFACE INTERACTIONS

Submitted by

Nicholas Michael Falk

Department of Atmospheric Science

In partial fulfillment of the requirements

For the Degree of Doctor of Philosophy

Colorado State University

Fort Collins, Colorado

Spring 2025

Doctoral Committee:

Advisor: Susan C. van den Heever
Co-Advisor: Leah D. Grant

Michael M. Bell
Russ S. Schumacher
Subhas K. Venayagamoorthy

ABSTRACT

COLD POOL PROPAGATION AND COLD POOL-LAND SURFACE INTERACTIONS

Convective cold pools are important components of the Earth system as they influence processes such as deep convective initiation, storm longevity and intensity, surface energy fluxes, and aerosol transport. The overarching goal of the research outlined in this dissertation is to investigate the propagation characteristics of cold pools, as well as the interactions between cold pools and the land surface. The three studies comprising this dissertation use field campaign observations and high-resolution numerical simulations to investigate these cold pool processes.

The first study evaluates a popular density current propagation speed equation using a large, novel set of radiosonde and dropsonde observations. First, data from pairs of sondes launched inside and outside of cold pools, along with the theoretical density current propagation speed equation, are used to calculate sonde-based propagation speeds. Second, radar/satellite-based propagation speeds are calculated by manually tracking the propagation of cold pools and correcting for advection due to the background wind. Comparisons of the propagation speeds calculated in these different ways demonstrate that sonde-based and radar- based propagation speeds are strongly correlated for US High Plains cold pools, suggesting the density current propagation speed equation is appropriate for use in midlatitude continental environments. Sonde-based propagation speeds are largely insensitive to how cold pool depth is defined, since the preponderance of negative buoyancy is near the surface in cold pools. Sonde-based propagation speeds can vary by ~300% based on where and when the sondes were launched, suggesting sub-mesoscale variability could have a major influence on cold pool propagation.

The impacts of topographic slope on daytime haboob propagation speeds and dust lofting are examined in the second study comprising this dissertation, along with how these impacts are modulated by surface roughness length. A suite of 40 idealized, large-eddy simulations are conducted with varied linear topographic slopes and surface roughness lengths. It is found that on flat ground, greater surface roughness increases drag on haboobs and causes haboobs to dissipate faster, thereby decreasing both haboob propagation speeds and associated dust lofting. As the topographic slope is increased, an upslope anabatic wind forms which causes downslope haboob propagation speeds to decrease and upslope haboob propagation speeds to be mostly unchanged. Anabatic winds act to loft dust as well, leading to increased masses of dust being lofted jointly by the haboob and anabatic wind as topographic slopes are increased.

The third study investigates the individual and synergistic impacts of cold pools and land surface heterogeneity on convection initiation. Idealized large eddy simulations of deep convection over the Amazon rainforest are conducted testing realistic and homogenized vegetation, along with realistic and eliminated cold pools. Convection initiation is more frequent over forested than deforested areas due to more favorable thermodynamics. Heterogeneous vegetation aggregates storm initiation locations compared with homogeneous vegetation. Over heterogeneous vegetation, cold pools propagate into deforested regions, thereby initiating storms and disaggregating storm initiation locations. Convection initiation locations are randomly distributed over homogeneous vegetation, with or without cold pools, demonstrating that cold pools have minimal impacts on convection initiation locations over homogeneous vegetation.

The findings of this dissertation research shed new light on fundamental cold pool processes and should be helpful for improving the representation of cold pools in forecast and climate models. Several avenues for future research are discussed.

ACKNOWLEDGEMENTS

There are many, many people I need to thank for supporting me on my journey throughout graduate school. I feel like my words cannot truly express my full gratitude, but I have endeavored to do my best in the following lines.

To Sue van den Heever, I must first thank you for putting your faith in me and choosing me for your group. None of this would have happened without that. Sue, you often say that you view yourself foremost as a teacher and a mentor, and I certainly agree with that assessment. You have consistently challenged me to learn and grow as a scientist. I can't thank you enough for the time and effort you have spent guiding me towards becoming the scientist I am today. The lessons I have learned from your mentorship will last me for life. On top of these lessons, you have also opened up opportunities for me such as BACS and the Cold Pool Workshop which have been amazing adventures.

To Leah Grant, what I have said above about Sue applies to you as well. Your mentorship has been invaluable, and I have learned so much from you. I must have come by your office hundreds of times in the last few years to ask you questions. Those informal conversations have been vital for completing the research for this dissertation. Additionally, I must thank you for your leadership during BACS. We couldn't have done it without you (or all the popsicles you provided).

To the rest of my committee, Michael Bell, Russ Schumacher, and Karan Venayagamoorthy, thank you for your time and your many helpful comments on my work. I especially appreciate your effort during my preliminary exam. Your questions forced me to think more deeply on many topics than I ever had before. My prelim was a transformative experience and a major part of my growth as a scientist.

To all of the department faculty, thank you for being such excellent teachers and invaluable sources of knowledge. If I had the time, I would spend years just taking every class offered by our department.

To the department staff, especially Sarah Tisdale, Nate Gronlund, Noel Bryan, and Ammon Redman, endless thanks for your amazing help on so many fronts. Sarah, thank you for turning the maze of forms and paperwork involved in graduate school into an easy-to-understand path. Nate, thank you for all of the room reservations, for listening to all of my complaining about the HVAC, and for your hilarious emails. Noel, thank you for all of your hard work organizing my travel. Ammon, thank you for all of your hard work solving problems (sometimes created by me) and maintaining Sue's computers.

I must also thank the whole of the van den Heever group. I often look forward to coming into the office each day because I get to work with such a friendly, helpful, and kind group of people. I certainly could not have completed this dissertation without the vast amounts of help on coding, science, and literature I have received from everyone in the group. Many group members are coauthors on the publications associated with this work, and you have all been invaluable in your contributions. I also appreciate the many group social activities (especially pumpkin carving every October), which have always been a great way to unwind after a day of work.

I must thank everyone on the BACS team for making BACS such a success. I think BACS was an amazing experience largely because the BACS team worked so well together. All those radiosondes launches and drone flights in cold pools were often quite difficult and exhausting, but that data forms the backbone of Chapter 2 of this dissertation. I am forever grateful for all of that hard work that has allowed me to dive into the theory of cold pool propagation.

Another quite unique experience I have had as a graduate student was attending the Cold Pool Workshop. I have been to many conferences, but this has been the only one in a German castle. I thank Sue and Cathy Hohenegger for organizing this workshop, inviting me to attend, and including me in the resulting paper. I also thank all of the participants for creating such a welcoming and intellectually stimulating atmosphere.

Thanks to all of the authors of the "How Variable Are Cold Pools?" paper, specifically Bastian Kirsch, Mirjana Sakradzija, and Felix Ament who collaborated with members of the van den Heever group. That was a great collaboration, and we uncovered some very interesting findings.

Thanks to Adele Igel, Matt Igel, and Ian Faloona for offering me research experience and their mentorship while I was an undergraduate at UC Davis, and thanks to all of the atmospheric science faculty at Davis for their excellent teaching. I left Davis with an incredibly solid foundation that I have built upon during my graduate studies. There is no way I could have completed this work without that foundation.

Thanks to all of my friends – especially Michael DeCaria, Eric Goldenstern, Wei-Ting Hsiao, Jingxuan Cui, Kevin Yang, and Kiara Sweitzer – and to all of the students in the department. The countless hours spent hiking, playing board games, cooking, etc have been endless fun and important relaxation time.

Nathan, I can't express how much your love and support has meant to me. Thank you for that love and support, and for being so understanding with the amount of time I have had to dedicate to work.

To Mom, Dad, Erica, and Joel, thank you for unwavering love and support. I don’t know how I would have completed graduate school without being able to spend time with you in Nevada.

I thank NSF Grants AGS-2029611 and AGS-2105938 for funding this research.

TABLE OF CONTENTS

Chapter 1: Introduction

1.1 The Importance of Cold Pools

Cold pools are density currents formed by the evaporation of hydrometeors below the base of convective clouds (Simpson 1969; Charba 1974; Wakimoto 1982). Cold pools are the subject of this dissertation, specifically the propagation of cold pools, and the interactions between cold pools, the Earth's land surface, and convection. Cold pools are a worthy subject of study for many reasons. First, cold pools are a common and widespread phenomenon, since they form in association with any precipitating convection. They form in the tropics, midlatitudes and polar regions, over both land and ocean. Observational studies of cold pools have taken place in the US High Plains (e.g. van den Heever et al. 2021), the US Midwest (e.g. Charba 1974), the Caribbean Sea (e.g. Vogel et al. 2021), Argentina (e.g. Lombardo and Kumjian 2022), Germany (e.g. Kirsch et al. 2024), the Saharan Desert (e.g. Knippertz et al. 2007), Equatorial Africa (e.g. Hoeller et al. 2024), the Arabian Peninsula (e.g. Miller et al. 2008), the Bay of Bengal (e.g. Simoes-Sousa et al. 2022), Southern China (e.g. Mai et al. 2023), the Philippine Sea (e.g. Reid et al. 2023), and the eastern tropical Pacific (e.g. Wills et al. 2021). Second, cold pools commonly initiate convection. Over half of all convective storms in some regions are initiated by cold pools (e.g. Purdom 1976; Wilson and Schreiber 1986; Lima and Wilson 2008). The initiation of convection by cold pools – and similar atmospheric density currents like sea-breezes – is a challenging operational forecast problem and a source of error in climate models (Garcia-Carreras et al. 2013; Birch et al. 2015; Rooney et al. 2022). Hence, much effort has been spent studying how and why cold pools initiate convection. Third, cold pools can intensify and organize convection. Interactions between cold pools and wind shear are important for the maintenance of squall lines (Rotunno et al. 1988; Weisman and Rotunno 2004). In low shear environments, deeper cold pools can lift air to greater heights than shallower cold pools, which enables longer-lived convection (Houston and Wilhelmson 2011). Cold pools can also facilitate the transition of shallow convection into deep convection (Khairoutdinov and Randall 2006; Schlemmer and Hohenegger 2014). Fourth, cold pools can create strong surface winds which cause damage and can intensify wildfires (Johnson et al. 2014; Bresch et al. 2021; Squitieri et al. 2023). Finally, cold pools can loft aerosols such as mineral dust into the atmosphere (Knippertz et al. 2007; Seigel and van den Heever 2012a; Marsham et al. 2013; Bukowski and van den Heever 2022), which have important impacts on climate and the global biogeochemical cycle (Adebiyi et al. 2023; Kok et al. 2023). As cold pool propagation is the first major focus of this dissertation, this topic is now discussed in more detail.

1.2 Cold Pool Propagation

Density current propagation speed equations are frequently applied to cold pools. Chapter 2 focuses on the following propagation speed equation from Rotunno et al. (1988), referred to as EQ-RKW88:

$$C^2 = -2\int_0^h B\,dz \qquad (1.1)$$

where C is the propagation speed of the cold pool, h is the depth of the cold pool, and B is the buoyancy inside the cold pool. EQ-RKW88 assumes negative buoyancy inside cold pools (if B is positive, C will nonsensically be an imaginary number), and so for the purposes of clarity, it is more useful to analyze the buoyancy magnitude (i.e. absolute value of buoyancy) inside of cold pools. EQ-RKW88 does not assume buoyancy is constant with height. From EQ-RKW88, we can see that a cold pool with a greater vertically integrated buoyancy magnitude will propagate more rapidly than a cold pool with a smaller vertically integrated buoyancy magnitude, all else equal. The magnitude of buoyancy increases as cold pools become increasingly colder and/or drier than their surrounding environment. For two initially identical cold pools which dissipate over time, the cold pool that dissipates more slowly will be the colder of the two, and thus will propagate faster than the warmer cold pool that dissipates more quickly. This relationship between cold pool propagation speed, cold pool relative buoyancy profiles, and cold pool dissipation is investigated throughout Chapters 2 and 3.

1.3 Surface Energy Fluxes

Surface energy fluxes, and the turbulent entrainment they drive, are a primary driver of cold pool dissipation as they increase temperature and moisture within cold pools, thus reducing the magnitude of their buoyancy (Grant and van den Heever 2016, 2018; Gentine et al. 2016). In the Land-Ecosystem-Atmosphere-Feedback version 3 (LEAF-3) (Walko et al. 2000) model coupled to the Regional Atmospheric Modeling System (RAMS) (Pielke et al. 1992; Cotton et al. 2003; Saleeby and van den Heever 2013), surface sensible heat flux (SHF) and surface latent heat flux (LHF) are parameterized using the following bulk aerodynamic formulas:

$$SHF = C_d C_p \rho_{air} U\left(T_{sfc} - T_{air}\right) \tag{1.2}$$

$$LHF = C_d C_p \rho_{air} U\left(Q_{sfc} - Q_{air}\right) \tag{1.3}$$

where C_d is an aerodynamic bulk transfer coefficient, C_p is the heat capacity of dry air at constant pressure, ρ_{air} is the density of air, U is the near-surface wind speed, and T_{sfc}/Q_{sfc} are the temperature and water vapor mixing ratios of the surface and near-surface air, respectively. In line with Eq. (1.2) and Eq. (1.3), observational studies have shown that cold pools can increase surface fluxes by increasing near-surface wind speeds and increasing gradients of temperature and moisture between the air and the surface (Johnson and Nicholls 1983; Young et al. 1995; Saxen and Rutledge 1998; Simoes-Sousa et al. 2022; Wills et al. 2023). The transfer coefficient is also important in determining surface fluxes. The transfer coefficient is dependent on many factors, but the factor critical to the analysis presented in this dissertation is the surface roughness length. A surface with a longer roughness length has greater downward momentum transfer to the surface and hence greater surface fluxes than a surface with a shorter roughness length. To represent this process in Eq. (1.2) and Eq. (1.3), the transfer coefficient increases as the surface roughness increases. Differences in surface fluxes due to differences in surface roughness drive important cold pool processes, as demonstrated in Chapters 3 and 4.

1.4 Outline of Dissertation

This dissertation is outlined as follows. The applicability of EQ-RKW88 to observed cold pool propagation speeds is tested in Chapter 2. Data from the Colorado State University Convective CLoud Outflows and UpDrafts Experiment (C^{3}LOUD-Ex) (van den Heever et al. 2021), BioAerosols and Convective Storms (BACS) (UCAR/NCAR-Earth Observing Laboratory 2024), and the NASA Cloud, Aerosol and Monsoon Processes Philippines Experiment (CAMP^{2}Ex) (Reid et al. 2023) are used. Sonde-based propagation speeds are calculated by pairing sondes that were launched inside and outside of a given cold pool, calculating buoyancy and cold pool depth from the sonde pairs, and then applying these values in EQ-RKW88. Radar/satellite-based propagation speeds are determined by manually tracking cold pools in radar and satellite data. Comparisons of these propagation speeds demonstrate that sonde based-propagation speeds are correlated with radar/satellite-based propagation speeds for US High Plains cold pools, indicating that EQ-RKW88 is applicable to cold pools in this environment.

Sonde-based propagation speeds are insensitive to the way in which cold pool depth is calculated as most buoyancy is near the surface of cold pools. Sub-mesoscale variability can cause sonde-based propagation speeds to vary by ~300% for a single cold pool. This study has been accepted pending revision at *Journal of the Atmospheric Sciences*.

The effects of three factors – topographic slope, surface roughness, and dust-radiative interactions – on haboob propagation and dust lofting are examined in Chapter 3. A suite of idealized RAMS simulations is conducted where the aforementioned factors are varied. Increased surface roughness increases surface sensible heat fluxes and causes haboobs to dissipate faster. On flat terrain, this means greater surface roughnesses cause haboobs to propagate more slowly and loft less total dust than haboobs on slopes with reduced surface roughnesses. On sloped terrain, sensible heat fluxes drive anabatic winds which increase in speed with both increasing topographic slope and surface roughness. These anabatic winds cause haboobs to propagate faster upslope than they propagate downslope. The anabatic winds also loft dust, causing greater masses of dust to be lofted as the topographic slope is increased. This study is to be submitted to *Journal of Geophysical Research: Atmospheres*.

The individual and synergistic effects of cold pools and vegetation heterogeneity on convection initiation are studied in Chapter 4. Idealized RAMS simulations of deep convection representative of the Amazon rainforest are conducted. These simulations separately and jointly test homogenizing the surface vegetation and disabling low-level evaporation to eliminate cold pools. Storms are tracked to identify where they initiate. The results indicate that convection initiation is more frequent and rainfall is greater over areas with rainforest than over deforested areas. These discrepancies become greater when cold pools are weakened as cold pools can otherwise initiate storms – and hence rainfall – in deforested regions. The impact of cold pools is found to be minimal over homogeneous surfaces. This research is to be submitted to *Geophysical Research Letters*.

Finally, in Chapter 5 results from the three individual studies are summarized and synthesized. Future research on many aspects of cold pools is recommended.

Chapter 2: Do Cold Pools Propagate According to Theory?

2.1 Introduction

Accurate estimations of convective cold pool propagation speeds are important for predicting high-impact weather such as intense convection, damaging wind gusts, dust storms, and intensification of wildfires (Rotunno et al. 1988; Miller et al. 2008; Bresch et al. 2021; Squitieri et al. 2023). Theoretically derived equations exist which relate the propagation speed of a cold pool to its thermodynamic properties (Benjamin 1968; Rotunno et al. 1988; Bryan and Rotunno 2008) and are often used in theoretical and modeling studies (Lafore and Moncrieff 1989; Trier et al. 2006; Seigel et al. 2013; Seigel and van den Heever 2013; Grant and van den Heever 2016). Due to a lack of appropriate observations, these theoretical equations have only been applied to observations of real cold pools in limited case studies (Charba 1974; Wakimoto 1982; Bryan et al. 2004, 2005; Bryan and Parker 2010). Hence, it remains ambiguous as to how accurately these theoretical equations can approximate the propagation speeds of real cold pools. This paper assesses the accuracy of such theoretical equations by applying them to a large dataset of cold pool observations.

Cold pools are a type of density current, as are other flows driven by differences in density such as sea breezes, avalanches, and salt wedges (Simpson 1997). One common way to understand cold pool propagation is by using analytic density current models (hereafter referred to as density current theory). Such models usually represent a denser fluid – of depth h and density ρ – intruding into a less dense fluid – of density ρ_0 – in a rigid channel of depth H. If ρ and ρ_0 are constant with height, the propagation speed C of the current is

$$C^2 = 2gh\frac{\rho-\rho_0}{\rho_0} \qquad (2.1)$$

where g is the acceleration due to gravity (von Kármán 1940; Benjamin 1968). Eq. (2.1) is obtained by applying the incompressible Boussinesq equations to an unsheared, unstratified, and hydrostatic environment with free-slip boundaries, no flow inside of the current, and assuming $H \gg h$. In their seminal work on squall lines, Rotunno et al. (1988) subsequently expanded Eq. (2.1) by considering a current where density varies with height and found

$$C^2 = -2\int_0^h B dz \tag{2.2}$$

where B is the buoyancy inside of the current. Here

$$B = g\frac{\theta_{v,CP} - \theta_{v,ENV}}{\theta_{v,ENV}} \tag{2.3}$$

where θ_v is the virtual potential temperature, the subscript CP indicates conditions inside of the cold pool, and the subscript ENV indicates conditions in the environment surrounding the cold pool. Eq. (2.2) (hereafter EQ-RKW88) is the density current propagation speed equation that forms the focus of this study as it does not neglect the variation of buoyancy with height, nor the effect of moisture on buoyancy, both of which are more appropriate to real atmospheric cold pools. Virtual potential temperature does neglect the effect of condensate loading on buoyancy. Condensate loading in cold pools could lead to greater negative buoyancy and hence larger values of C. If a cold pool propagates away from its parent storm and other storms, the effect of condensate loading will be negligible as there are no longer hydrometers present in the cold pool.

The Froude number, the ratio of inertial to gravitational forces in a density current, is another useful concept arising from density current theory that can be applied to cold pools. Cold pool Froude numbers are important as they can be used to evaluate if cold pools obey density current theory. Benjamin (1968) demonstrates the Froude number is theoretically determined by the fractional depth ($\frac{h}{H}$) of an idealized density current. Upper and lower theoretical bounds on the Froude number of $\sqrt{2}$ and $\frac{1}{\sqrt{2}}$ are thus set by the largest ($H \gg h$) and smallest ($H = 2h$) possible channel depths. For EQ-RKW88 the Froude number is

$$Fr = \frac{C}{\sqrt{-\int_0^h B dz}} = \sqrt{2} \tag{2.4}$$

due to the assumption of $H \gg h$. If both the propagation speed and the buoyancy inside of a cold pool are observed, then the Froude number can be calculated empirically. While the Froude number is determined only by the channel depth in Benjamin's theoretical calculations, empirically calculated Froude numbers are also influenced by factors such as surface drag, which are usually neglected by density current theory. Simpson (1969), Charba (1974), and Wakimoto (1982) helped establish that cold pools are density currents by empirically calculating cold pool Froude numbers and showing they are comparable to Froude numbers of laboratory tank density currents and Benjamin's theoretical calculations (Table 2.1). This demonstrates that factors neglected by density current theory are likely not of first order importance to cold pool propagation. Observations of cold pool Froude numbers are also important as they can be used in parameterizations. For example, Rooney et al. (2022) assume a Froude number of unity in their C-POOL scheme.

Many studies have applied theoretical density current propagation speed equations to cold pools in simulation data, often in the context of RKW theory. RKW theory (named after the authors of Rotunno et al. (1988)) posits that a balance between C and the low-level wind shear leads to the deepest lifting of air by a cold pool and is thus an optimal state for the re-initiation of convection in squall lines (Rotunno et al. 1988; Weisman et al. 1988; Weisman and Rotunno 2004). Trier et al. (2006) find that integrating EQ-RKW88 all the way to the tropopause leads to values of C that match mesoscale convective system (MCS) propagation speeds more closely than simply integrating EQ-RKW88 to the cold pool top. Criticisms of RKW theory include that it neglects the effect of deep-layer shear, and that observed squall line environments usually have less shear than RKW theory would deem optimal (Stensrud et al. 2005; Coniglio et al. 2012). Weisman and Rotunno (2004) also find better correspondence between RKW theory and simulated convective structure when considering shear to a depth of 5 km, which is deeper than most cold pools. While the aforementioned studies focus on midlatitude continental environments, studies of convection outside of this regime find different results. By calculating C for cold pools in simulations of West African squall lines, Lafore and Moncrieff (1989) argue that a squall line is only controlled by cold pools if C is greater than the system propagation speed. Some studies find that RKW theory does not explain tropical oceanic convective systems (Webster et al. 2002; Moncrieff and Lane 2015; Grant et al. 2018), while other studies argue these systems can be explained by RKW theory (Keenan and Carbone 1992; Robe and Emanuel 2001). Outside of RKW theory, many modeling studies use C as a metric for the intensity and speed of cold pools (Droegemeier and Wilhelmson 1985; Seigel et al. 2013; Seigel and van den Heever 2013; Schlemmer and Hohenegger 2014; Feng et al. 2015; Grant and van den Heever 2016, 2018; Kurowski et al. 2018; Bukowski and van den Heever 2021).

Past studies have also applied density current propagation speed equations to observed cold pools. Note that all the observational studies listed in Table 2.1 in which a Froude number is provided applied a density current propagation speed equation, as this is required to calculate Froude numbers. Kirsch et al. (2024) use data from a dense network of surface stations in Germany and find that cold pool expansion was not explained well by a propagation speed equation. They argue that this discrepancy may be due to the equation neglecting variations of temperature within a cold pool, mixing with the environment, and/or surface friction. A subsequent study shows that such variations in cold pools properties may be large (Grant and Kirsch et al. 2024). On the other hand, Zuidema et al. (2012) note that in two of the cases they analyzed, precipitating cumulus moved 2-4 m s^{-1} faster than the wind. They use a density current propagation speed equation to determine that cold pool propagation speeds were likely ~3 m s^{-1} and thus could explain the motion of the clouds. Studies show observational support for RKW theory by applying EQ-RKW88 to radiosonde observations in and around MCSs in the USA (Bryan et al. 2004, 2005; Bryan and Parker 2010). Simoes-Sousa et al. (2022) estimate the depths of Bay of Bengal cold pools by applying a density current propagation speed equation to observations of cold pool temperature deficits and propagation speeds from buoys.

For all past observational studies that apply density current propagation speed equations to cold pools, at least one of the following caveats applies. First, most of these studies focus on three or fewer cold pools. Second, many of these studies are forced to make assumptions about the vertical structure of buoyancy within cold pools because they only have thermodynamic information from the surface. Third, some of these studies focus on the propagation speeds of convective systems as a whole and not specifically on the propagation speeds of the cold pools themselves. Given these caveats, and the widespread use of density current propagation speed equations in modeling studies of cold pools, the goal of the present study is to evaluate how well EQ-RKW88 approximates the propagation speeds of observed cold pools. A secondary goal is to assess the impact of the infinite channel depth and incompressibility assumptions in EQ-RKW88. We apply EQ-RKW88 to a relatively large dataset of targeted soundings within cold pools from three recent field campaigns to calculate theoretical cold pool propagation speeds. To determine actual cold pool propagation speeds, we track cold pool gust fronts in radar or satellite data. We then assess the accuracy of EQ-RKW88 in by comparing these sonde-based and radar/satellite-based propagation speeds.

2.2 Sonde, Satellite, and Radar Data

Soundings from three different field campaigns are used in this analysis: the Colorado State University Convective CLoud Outflows and UpDrafts Experiment (C^3LOUD-Ex, C3X in figure legends) (van den Heever et al. 2021), BioAerosols and Convective Storms (BACS) (UCAR/NCAR-Earth Observing Laboratory 2024), and the NASA Cloud, Aerosol and Monsoon Processes Philippines Experiment (CAMP^{2}Ex, C2X in figure legends) (Reid et al. 2023). These three field campaigns measured cold pools in two distinct environments: the US High Plains (C^3LOUD-Ex and BACS), a continental mid-latitude environment, and the Philippine Sea and South China Sea (CAMP^{2}Ex), a tropical maritime environment (Table 2.2, Fig. 2.1a-b). BACS took place at a fixed site and so all BACS sondes used in this study are represented by a single point in Fig. 2.1a. While radiosondes were launched from the ground during C^3LOUD-Ex and BACS, dropsondes were launched from an aircraft during CAMP^{2}Ex. In all three of these field campaigns, sondes were launched both into and ahead of cold pools, which is critical for the methodology described in the next section.

We track C^3LOUD-Ex and BACS cold pool propagation in Next Generation Weather Radar (NEXRAD) reflectivity data. Due to a lack of radar coverage over the Philippine and South China Seas, corrected Reflectance (true color) at 1 km resolution from the Japan Meteorological Agency's Advanced Himawari Imager (AHI) on the Himawari-8 spacecraft (Da 2015) is used to track the propagation of CAMP^{2}Ex cold pools. The NEXRAD reflectivity used in this study has a variable temporal frequency between 4 min and 9 min. The AHI true color imagery has a temporal frequency of 10 min.

Storm morphology, cold pool age, and cold pool mergers/collisions could all potentially play a role in influencing cold pool propagation speeds. From radar and satellite data, we subjectively categorize the parent convection of cold pools as scattered, multicellular, or supercellular (Table 2.2). Cold pools which appear to no longer have convection supplying them with cold air are classified as dissipating (Table 2.2). We also identify cold pools which appear to merge with another cold pool or boundary before or during sampling (Table 2.2). All cold pools that are a suitable fit for the methodology described in the next section are included regardless of storm morphology, cold pool age, and cold pool mergers. We do not have sufficient data to disentangle the impacts of these phenomena on cold pool propagation speeds. To speculate briefly, organized convective systems may produce faster propagating cold pools than those produced by scattered convection due to effects such as the downward transport of momentum in a rear inflow jet (Weisman 1992), or newly-formed cold pools could propagate slower than older cold pools due to the slumping effect described by Huppert and Simpson (1980). It is also difficult to determine when a cold pool has completely dissipated and EQ-RKW88 is no longer applicable. Head-on cold pool collisions can clearly slow or halt cold pool propagation (Droegemeier and Wilhelmson 1985; Meyer and Haerter 2020). We do cease tracking the propagation of a cold pool if it collides head-on with another boundary in radar or satellite data. The effect on propagation speeds of multiple cold pools merging upscale into a single cold pool is unclear.

2.3 Determining Cold Pool Propagation Speeds

2.3.1 Sonde-Based Propagation Speeds

Sonde pairs are used to apply EQ-RKW88 to observed cold pools. A sonde pair consists of a cold pool sonde launched inside of a cold pool, and an environmental sonde launched outside of that cold pool. This method follows a similar approach taken by Bryan et al. (2004, 2005) and Bryan and Parker (2010). We use 36 sonde pairs which sampled 22 cold pools (Table 2.2). Environmental sondes are meant to be representative of the environments into which their respective cold pools propagate. Hence, each sonde pair is chosen such that the environmental sonde and the cold pool sonde are spatiotemporally close to each other (Table 2.2). Previous research has shown convection can influence its surrounding environment (Potvin et al. 2010; Wade et al. 2018; Coniglio and Parker 2020), so environmental sondes are also chosen to be as free from the influence of storms as possible. While the distance between cold pool and environmental sondes is often <1 km for C^{3}LOUD-Ex and BACS (Table 2.2), in these campaigns cold pools were often sampled after they had propagated away from their parent convection. Environmental sondes could thus be launched a few minutes before cold pool passage and still be in an airmass not influenced by convection. Despite this, some environmental sondes may be influenced by convection if no other possible environmental sonde is available. It is important to note that some sonde pairs sample the same cold pools and/or use the same environmental sondes. Some figures plot values for every sonde pair (e.g. Fig. 2.3a), and thus show multiple observations for some cold pools. Other figures plot median values for each cold pool (e.g. Fig 2.3b), and thus show only a single value for each cold pool. The naming scheme for sonde pairs and the names of example sonde pairs are included in section 2.3.4.

To apply EQ-RKW88, the buoyancy profile B for each sonde pair is calculated using the virtual potential temperature profiles from the environmental sonde and the cold pool sonde (Fig.

2.1 c-d). We neglect the effect of condensate loading, since observations of hydrometeor mass are unavailable for all sondes. As some of the cold pool sondes were launched into precipitation, neglecting loading may lead to underestimated propagation speeds for these sondes. A cold pool depth, h, is also needed to apply EQ-RKW88. Cold pool depths are determined subjectively through the following process. First, for each sonde pair, the first height where buoyancy changes sign from negative to positive is taken to be the depth of the cold pool, as has been done previously (Bryan et al. 2005). This potential cold pool depth is then overlaid on a skew-T log-P diagram showing the temperature, dewpoint, and winds of the environmental sonde and the cold pool sonde. If the buoyancy-based cold pool depth is subjectively ascertained to be reasonable, then it is used for that sonde pair. If the buoyancy-based cold pool depth is subjectively ascertained to be unreasonable, then a different cold pool depth is chosen based on manual analysis of the skew-T log-P for this sonde pair. Of the 36 sonde pairs, 11 use subjectively chosen cold pool depths. Section 2.3.5 discusses an example sonde pair where the buoyancy-based cold pool depth was replaced with a subjectively chosen cold pool depth. All skew-T log-p diagrams pertinent to this analysis can be found via the link in the data availability statement. The impact of subjectively choosing cold pool depth on cold pool propagation speeds is explored in section 4c and is found to have only a small impact.

Once the buoyancy and cold pool depth are known for a sonde pair, the theoretical cold pool propagation speed is calculated using EQ-RKW88 (purple shaded area in Fig. 2.1 c-d). Fig. 2.1d also demonstrates the impact of moisture on buoyancy, and hence why we use virtual potential temperature when calculating buoyancy. The cold pool shown in Fig 2.1d is ~240 m deep based on analysis of buoyancy, but the temperature deficit in this cold pool is only ~50 m deep. Hereafter, the cold pool propagation speeds determined using the methodology described in this section are referred to as sonde-based propagation speeds (C_{sonde}) (or *theoretical* sonde-based propagation speeds to emphasize the theoretical nature of these values).

2.3.2 Radar/Satellite-Based Propagation Speeds

NEXRAD reflectivity data are used to determine radar-based propagation speeds (C_{radar}) for C^{3}LOUD-Ex and BACS cold pools. Cold pool gust fronts often appear as fine lines on radar, and several previous studies have tracked these fine lines to ascertain cold pool propagation speeds (Craig Goff 1976; Wakimoto 1982; Borque et al. 2020; Luchetti et al. 2020a). In this study we make use of a similar approach, outlined as follows.

First, for each cold pool, a radar reflectivity loop with an elevation angle of 0.5° is generated (Fig. 2.2a,c). The NEXRAD nearest to the location of the corresponding radiosondes is used, which is always Cheyenne (KCYS) or Denver (KFTG). In ideal circumstances, a ~1-hour loop of radar reflectivity is generated, centered on the time of the sondes. However, for some cold pools a ~1 h loop is not possible, such as when precipitation obscures the fine line. For these cold pools, the first and/or last scan in which the fine line is subjectively apparent is used. The shortest loop used is 25 min, and the mean length of loops is 51 min.

Second, a starting and ending point for the gust front are subjectively chosen such that the gust front is perpendicular to the line connecting these points and the gust front propagates along this line (Fig. 2.2a). When possible, these points are also chosen such that the line connecting them passes close to where the sondes observing the cold pool were launched (the distances are shown in Table 2.2). Features such as small bulges were followed when possible to ensure that a consistent point along the gust front was being tracked. However, the starting and ending points used in this study are ultimately subjective. To quantify the uncertainty due to this subjectivity, three cases were independently re-analyzed by 10 volunteers. An uncertainty of ±2.2 m s^{-1} is estimated and included in subsequent figures. Section 2.3.6 contains more information on the estimation of this uncertainty. All radar and satellite loops with starting and ending points can be found via the link in the data availability statement

Finally, the radar-based propagation speed is determined. A velocity vector called $\boldsymbol{V_{total}}$ is generated using the distance between the starting/ending point and the time between the first/last scan (Fig. 2.2c). While $\boldsymbol{V_{total}}$ contains information about the propagation speed of the cold pool, advection due to the background wind has not been accounted for. Thus, for each sonde pair, the mean wind measured by the environmental sonde over the depth of the cold pool, $\boldsymbol{V_{wind}}$, is calculated (Fig. 2.2c). The radar-based propagation speed and the radar-based velocity vector of the cold pool are given by:

$$C_{radar} = ||\boldsymbol{V_{radar}}|| = ||\boldsymbol{V_{total}} - \boldsymbol{V_{wind}}||. \qquad (2.5)$$

We track the arc clouds produced by CAMP^{2}Ex cold pools in AHI true color imagery due to a lack of radar data over the Philippine and South China Seas (Fig. 2.2b,d). Other than this difference, satellite-based propagation speeds for CAMP^{2}Ex cold pools ($C_{satellite}$) are determined using the same methodology as just described for the radar-based propagation speeds. When referring to data from CAMP^{2}Ex along with data from C^{3}LOUD-Ex and/or BACS, the terminology of radar/satellite-based propagation speeds ($C_{radar,satellite}$) is used.

For each cold pool only one pair of starting/ending points are chosen and thus only one value of $\boldsymbol{V_{total}}$ is determined. When a cold pool is sampled by multiple sonde pairs, different values of $\boldsymbol{V_{wind}}$ may occur for each sonde pair due to different environmental sondes being used and/or different cold pool depths being determined (since $\boldsymbol{V_{wind}}$ is the mean environmental wind over the depth of the cold pool). Hence, sonde pairs sampling the same cold pool can have radar/satellite-based propagation speeds that vary by up to ~1 m s^{-1} or up to ~26%.

Finally, note that the radar reflectivity and arc clouds being tracked are potentially above their respective cold pools. This is because these clouds and other radar targets are likely in air that is being lifted over the cold pool. This methodology thus assumes the propagation of these clouds and other radar targets is synonymous with the propagation of the cold pools themselves.

2.3.3 Differences in Methodology between the US High Plains and the Philippine Sea and South China Sea

It is worth explicitly discussing the unavoidable methodological differences in our analysis between US High Plains (C^3LOUD-Ex and BACS) and Philippine and South China Seas (CAMP^{2}Ex) cold pools. Tracking CAMP^{2}Ex cold pools in lower resolution satellite data may drive additional uncertainty compared to the tracking of C^3LOUD-Ex and BACS cold pools in NEXRAD data. Unfortunately, radar data is not available in the CAMP^{2}Ex domain. Comparing cases tracked using both satellite and radar data would be desirable. We attempted this comparison, but C^3LOUD-Ex and BACS cold pools could not be reliably identified in true color satellite imagery due to the drier environments in the US High Plains compared to the tropical oceans. Also, the distances between sondes in CAMP^{2}Ex sonde pairs are larger than those for C^3LOUD-Ex and BACS sonde pairs (Table 2.2). This is a result of aircraft dropsondes having been used during CAMP^{2}Ex compared to ground-based radiosondes having been used during C^3LOUD-Ex and BACS. This greater difference in distances between sondes in sonde pairs may lead to additional uncertainty for CAMP^{2}Ex results. Additionally, only a small number of CAMP2Ex cold pools were a suitable fit for our methodology (Table 2.2). Due to this small sample size, statistics such as variance explained and best fit lines are not calculated for CAMP2Ex cold pools. Results for the CAMP2Ex cold pools are presented in this paper simply as an interesting tropical oceanic contrast to continental mid-latitude cold pools from C3LOUD-EX and BACS. More targeted observations of tropical oceanic cold pools are needed before broad, robust conclusions can be drawn.

2.3.4 Sonde Pair Naming

Sonde pairs are named using the following format: YYYYMMDD_cp#_CPsonde_ENsonde where YYYY is the year, MM is the month, and DD is the day of the UTC start date of the C^{3}LOUD-Ex/BACS intensive operations period or the CAMP^{2}Ex research flight corresponding to the sonde pair. The cold pool number for that day sampled by the sonde pair is indicated by #. The cold pool sonde (environmental sonde) number used in the sonde pair is indicated by CPsonde (ENsonde). For BACS and CAMP^{2}Ex, sonde numbers count up from 1 for each sonde launched for each day. Since there were two minivans launching sondes during C^{3}LOUD-Ex, sonde numbers count up from 1 independently for each minivan for each day. Thus, sonde numbers are prefaced by E (or M) if they were launched from the *Elbert* (or *Massive*) minivan. For example, 20170601_cp1_M02_E01 is from the C^{3}LOUD-Ex intensive operations period that started on 1 June 2017, sampled the first cold pool that day used in this study, used the second sonde launched from the *Massive* minivan as the cold pool sonde, and used the first sonde launched from the *Elbert* minivan as the environmental sonde. One CAMP^{2}Ex cold pool (20190908_cp1) was sampled by a sonde pair early in its lifetime and was then sampled by a different sonde pair later in its lifetime after over an hour had passed.

This cold pool is thus treated as two separate cold pools (20190908_cp1a and 20190908_cp1b) with a different V_{total} being determined for each sonde pair.

The C^{3}LOUD-Ex example sonde pair shown in Fig. 2.1 and Fig. 2.2 is 20170607_cp1_M10_M07. The CAMP^{2}Ex example sonde pair shown in Fig. 2.1 and Fig. 2.2 is 20190908_cp1b_06_07. The first example sonde pair shown in Fig. 2.7 is 20230530_cp2_07_06, and the second example sonde pair shown in Fig. 2.7 is 20230610_cp1_05_04.

2.3.5 Example Sonde Pair with Subjectively Chosen Cold Pool Depth

Fig. 2.10 shows an example sonde pair where the buoyancy-based cold pool depth described in section 3a was rejected and replaced with a subjectively chosen cold pool depth. Cold pool sonde temperatures are slightly colder than environmental sonde temperatures between ~700 hPa and ~650 hPa (Fig. 2.10). This leads to slight negative buoyancy (not shown) between these levels and the buoyancy based cold pool depth (Fig. 2.10 yellow dashed line) being at ~650 hPa. We judge that this slight negative buoyancy is likely due to factors other than the cold pool. Since the cold pool temperature deficit and negative buoyancy has mostly vanished at ~700 hPa, that level is instead chosen as the subjective cold pool depth (Fig. 2.10 purple dashed line).

All skew-T log-p diagrams used in this study (similar to Fig. 2.10) can be found via the link in the data availability statement. As in Fig. 2.10, the cold pool depth chosen for the sonde pair is plotted as a purple dashed line on each of these skew-T log-p diagrams. For sonde pairs where the buoyancy-based cold pool depth was rejected, it is plotted as a yellow dashed line.

2.3.6 Uncertainty in Radar-Based Propagation Speeds

To quantify the uncertainty in our method of determining radar-based propagation speeds, we conducted a 10-participant experiment. The lead author had already chosen all of the starting and ending points used in this study. Three cold pools were each re-analyzed (i.e. new starting and ending points were chosen chosen) by 10 other participants (Fig. 2.11). The cold pools chosen include the example shown in Fig. 2.2 (8 June 2017; Fig. 2.11a,b), a relatively slow propagating case (5 May 2017; Fig. 2.11c,d), and the fastest propagating case (17 July 2016; Fig. 2.11e,f). The participants include coauthors on this manuscript and others who are not coauthors. All participants are graduate students or postdoctoral researchers studying mesoscale meteorology at Colorado State University. Participants viewed reflectivity loops on a computer screen covered in a clear piece of plastic. Participants used a dry erase marker to indicate their chosen starting and ending points. The lead author led the experiment, but left the room when participants were viewing loops so as to not influence their decision. The lead author also prevented participants from discussing their choices of starting and ending points with each other.

At the conclusion of this experiment, we have 11 pairs of starting and ending points for these three cases (Fig. 2.11). The range (maximum minus minimum) in radar-based propagation speeds for the 17 July 2016 case is 2.13 m s^{-1}. The ranges for the other cases are smaller (1.27 m s^{-1} to 1.62 m s^{-1}). We round the highest value of 2.13 m s^{-1} up to 2.2 m s^{-1} and use it as our most conservative estimate of uncertainty for radar-based propagation speeds and satellite-based propagation speeds throughout the analysis presented in the manuscript.

2.4 Results

2.4.1 Overall Statistics

Theoretical sonde-based propagation speeds are overall reasonable approximations of radar-based propagation speeds for US High Plains cold pools (Fig. 2.3). The variance in radar/satellite-based propagation speeds explained by sonde-based propagation speeds (hereafter referred to as the variance explained by EQ-RKW88) is ~69% for BACS (Fig. 2.3). For C^3LOUD-Ex, the variance explained by EQ-RKW88 is ~84% (Fig. 2.3). These results therefore suggest that EQ-RKW88 is generally highly appropriate for approximating the propagation speeds of US High Plains cold pools. Due to the small sample size of $CAMP^2$Ex cold pools, a similar conclusion can not be made about Philippine Sea and South China Sea cold pools.

To calculate the error in sonde-based propagation speeds, radar/satellite-based propagation speeds are assumed to be the true values of cold pool propagation speeds (Fig. 2.4a-b). Curiously, the percent error is inversely proportional to radar/satellite-based propagation speeds (Fig. 2.4b). This may be due, in part, to the estimated 2.2 m s^{-1} uncertainty in the radar/satellite-based propagation speeds being relatively constant for each sonde pair. However, without a third, more accurate metric for determining cold pool propagation speeds, this line of reasoning can only be speculative.

Jackknife resampling is conducted by recalculating statistics after removing a single observation from the data. The variance explained by EQ-RKW88 for C^3LOUD-Ex cold pools and all cold pools remains well above 60% for jackknife resampling. The variance explained only falls below 60% for BACS once when a specific sonde pair/cold pool is removed (Fig. 2.4c-d). Hence, these results are generally robust and not overly sensitive to the inclusion/exclusion of individual datapoints.

2.4.2 The Froude Number

A Froude number of $\sqrt{2}$ is used in EQ-RKW88 due to the assumption that the channel depth is infinite compared to the depth of the cold pool (i.e. $H \gg h$). This is a reasonable *a priori* assumption given that the atmosphere does not have a rigid lid like that assumed in the derivation of EQ-RKW88, and that cold pools are generally much shallower than the tropopause. Changing the Froude number in EQ-RKW88 would proportionally increase or decrease all theoretical sonde-based propagation speeds but would not change the variance explained by EQ-RKW88.

In this section, a different approach to the Froude number is taken. Instead of assuming a Froude number *a priori*, the Froude number for each sonde pair is calculated using:

$$Fr = \frac{c_{radar,satellite}}{\sqrt{-\int_0^h B dz}} = \frac{\sqrt{2} \times c_{radar,satellite}}{c_{sonde}}. \tag{2.6}$$

Previous studies have used an analogous approach to calculating Froude numbers for observed cold pools (see Table 2.1) (Charba 1974; Wakimoto 1982; Intrieri et al. 1990; Lothon et al. 2011). Froude numbers are calculated using Eq. (2.6) for all of the cold pools analyzed in this study (Fig. 2.5). Also plotted in Fig. 2.5 are lines at constant Froude numbers of $\sqrt{2}$ and $\frac{1}{\sqrt{2}}$ which correspond to the largest ($H \gg h$) and smallest ($H = 2h$) possible channel depths (Benjamin 1968).

Caution must be exercised when interpreting Froude numbers calculated using cold pool observations. The Froude number is intended to represent the ratio of the inertial force to the gravitational force in a density current. As sonde-based and radar/satellite-based propagation speeds are both subject to uncertainty, the Froude number inherits these uncertainties when calculated using Eq. (2.6) (Fig. 2.5 error bars). Assumptions in density current theory come into play as well. For example, Benjamin (1968) neglected many effects – such as surface drag –

when deriving his theoretical limits on the Froude number. However, observed cold pools are subject to these neglected effects which in turn may influence their Froude numbers.

Keeping in mind the uncertainties just discussed, Froude numbers in this study are in keeping with the Froude numbers reported for cold pools in the previous literature (Table 2.1, Fig. 2.5). Most Froude numbers lie between √2 (or ~1.41) and 1/√2 (or ~0.71) (Fig. 2.5), indicating that these observations generally support density current theory. Assuming a constant channel depth, the Froude number should decrease with increasing current depth (Benjamin 1968). This relationship is not apparent (Fig. 2.5), perhaps because the concept of "channel depth" is somewhat difficult to define for the Earth's atmosphere and/or because Benjamin's study does not consider factors such as surface drag or stratification of the background environment. The median Froude numbers in Fig. 2.5a (Fig. 2.5b) are 0.91 (1.14) for C3LOUD-Ex and 1.15 (1.16) for BACS. These median Froude numbers are less than the assumed value of √2 in EQ-RKW88, which is consistent with theoretical sonde-based propagation speeds generally overestimating the radar/satellite-based propagation speeds (Fig 2.3). Using EQ-RKW88 with a Froude number of ~0.9-1.2 instead of √2 may be preferable for US High Plains cold pools. A similar recommendation for Philippine and South China Seas cold pools cannot be made here due to the small sample size of CAMP2Ex cold pools.

2.4.3 The Impact of Varying Cold Pool Depths

So far, theoretical sonde-based propagation speeds have been calculated using cold pool depths that are ultimately subjective (see section 3a). In this section, we explore other possible metrics for defining cold pool depth and the impact of using these different metrics on sonde-based propagation speeds. Observations of cold pool depth are sparse and approximated using a wide range of different methodologies (see Simoes-Sousa et al. (2022) Table 1 and references therein). Hence, the results of this section not only place our approach within context, but are also helpful for later studies investigating cold pool depth.

For each sonde pair (in chronological order), the cold pool depth is calculated using five different metrics (Table 2.3, Fig. 2.6a). Since buoyancy is used as a first guess for the *subjective* cold pool depths, for most cold pools the *subjective* and *buoyancy* metrics yield the same cold pool depth. The *temperature* metric considers temperature – usually the dominant influence on the buoyancy in cold pools – while ignoring the effects of moisture and pressure. The *direction* and *speed* metrics both use winds instead of thermodynamic variables, since winds should theoretically return to near their environmental values above a cold pool. The values of 10° and 5 m s^{-1} used in the *direction* and *speed* metrics, respectively, were selected after subjective analyses of the environmental and cold pool sondes.

The five cold pool depth metrics yield quite disparate cold pool depths for many sonde pairs (Fig. 2.6a). The variability in sonde-based propagation speeds, however, appears to be smaller than the variability in cold pool depth (Fig. 2.6b). To quantify the variability in cold pool depths and sonde-based propagation speeds due to these different depth metrics, we calculate the range of cold pool depths and sonde-based propagation speeds for each sonde pair and determine the median of these ranges. The median range of cold pool depths is 940 m while the median range of sonde-based propagation speeds is 1.33 m s^{-1}. For comparison, the *subjective* cold pool depth metric yields a median cold pool depth of 1160 m and a median sonde-based propagation speed of 7.90 m s^{-1}. Thus, using the aforementioned metrics for cold pool depth, the variability in cold pool depth is much larger relative to the median cold pool depth ($\frac{940\ m}{1160\ m} = {\sim}81\%$) than the variability in sonde-based propagation speed is relative to the median sonde-based propagation speed ($\frac{1.33\ m\ s^{-1}}{7.90\ m\ s^{-1}} = \sim 17\%$).

Analysis of buoyancy profiles demonstrates why sonde-based propagation speeds are relatively insensitive to the different cold pool depth metrics. While there is substantial variability in the shapes of the individual buoyancy profiles, the mean buoyancy profile changes roughly linearly with height with the largest (smallest) magnitudes near the bottom (top) (Fig. 2.6d). Since EQ-RKW88 integrates buoyancy with respect to height, and as buoyancy is usually small in magnitude near the tops of cold pools, it follows that relatively large changes in cold pool depths do not always translate to relatively large changes in sonde-based propagation speeds. In other words, while the height to which EQ-RKW88 is integrated can change substantially, the area over which EQ-RKW88 is integrated does not change substantially.

The variance explained by EQ-RKW88 is recalculated using the different cold pool depth metrics (Fig. 2.6c). If a metric cannot determine a cold pool depth for a given sonde pair, then the subjective cold pool depth is used for that sonde pair when calculating the variance explained. This prevents the number of points used to calculate the variance explained from changing between the metrics. It is evident from Fig. 2.6c that the variance explained by EQ-RKW88 is relatively insensitive to which cold pool depth metric is used, in agreement with the low variability shown in Fig. 2.6b. Thus, the conclusions drawn in previous sections are largely insensitive to the subjective method used to determine cold pool depths.

2.4.4 The Impact of Assumptions Used to Derive EQ-RKW88

As discussed in the introduction, many assumptions are used in the derivation of EQ-RKW88. The impact of two of these assumptions are investigated in this section: (1) an infinite channel depth; and (2) an incompressible atmosphere. These two assumptions are tested individually and together.

Cold pools with depths exceeding 4 km were observed by Bryan et al. (2005). Bryan and Rotunno (2008) (hereafter BR08) argue that applying the incompressible Boussinesq equations to such cold pools would be inappropriate as vertical displacements due to these cold pools would not be small relative to the density scale height of the atmosphere. BR08 then use the deep anelastic equations to derive a new propagation speed equation

$$C^2 = \frac{\int_0^h \bar{\rho}\left(\int_0^z B dz'\right)dz + \int_0^h B dz \int_h^H \bar{\rho} dz}{\int_0^H \bar{\rho} dz\left(\frac{1}{2} - \frac{\int_0^H \bar{\rho} dz}{\int_h^H \bar{\rho} dz}\right)} \qquad (2.7)$$

where $\bar{\rho}$ is the density of the environment surrounding the cold pool. Eq. (2.7) will hereafter be referred to as EQ-BR08.

EQ-BR08 assumes neither an incompressible atmosphere nor an infinite channel depth. To understand the impact of these two assumptions separately, an equation which assumes an incompressible atmosphere but not an infinite channel depth is derived. By starting with EQ-BR08 and assuming an incompressible atmosphere (that is, that $\bar{\rho}$ is constant with height), it can be shown that

$$C^2 = \frac{-2(H-h)}{H(H+h)}\left(\int_0^h\left(\int_0^z B dz'\right)dz + (H-h)\int_0^h B dz\right). \qquad (2.8)$$

Eq. (2.8) will hereafter be referred to as EQ-INC-FIN (INCompressible and FINite).

A channel depth (H) is needed to apply EQ-BR08 and EQ-INC-FIN to cold pool observations. Xue (2002) argued that the tropopause can be used as the channel depth when applying analytic density current equations to atmospheric phenomena. As such, sonde observations extending to the tropopause are necessary for this analysis. NASA’s P-3 flights were restricted to mid-tropospheric levels during CAMP^{2}Ex, so all of the CAMP^{2}Ex dropsonde observations are precluded. During C^{3}LOUD-Ex and BACS, only two radiosondes could be tracked simultaneously. Sondes were therefore often terminated in the middle troposphere to facilitate the rapid launch of subsequent sondes. Hence, only four sonde pairs in which the environmental sonde was tracked until the tropopause are available (see Fig. 2.7 for two examples). We apply EQ-BR08 and EQ-INC-FIN to these four sonde pairs by calculating the tropopause depth H and environmental density $\bar{\rho}$ using the environmental sonde (Fig. 2.8a). The tropopause depth is calculated using the simplified WMO definition described by Maddox and Mullendore (2018). To apply EQ-INC-FIN and EQ-BR08 to all sonde pairs, ERA5 reanalysis data are used (Hersbach et al. 2020). The grid column in ERA5 spatiotemporally closest to each environmental sonde is determined. Tropopause depths (H) and environmental densities ($\bar{\rho}$) are calculated using these ERA5 columns and used in lieu of data from their respective environmental sondes. For the four sonde pairs with environmental observations to the tropopause, propagation speeds for a given equation (EQ-INC-FIN or EQ-BR08) are negligibly different when using H and $\bar{\rho}$ from environmental sondes versus from ERA5 (Fig. 2.8a, filled vs hollow triangles). This comparison demonstrates our use of ERA5 data likely does not have a meaningful influence on subsequent results.

We define the "channel depth effect" as the percent difference between propagation speeds from EQ-RKW88 and EQ-INC-FIN. Similarly, we define the "compressibility effect" as the percent difference between EQ-INC-FIN and EQ-BR08, and the "combined effect" as the percent difference between EQ-RKW88 and EQ-BR08. Each of these effects reduces theoretical sonde-based propagation speeds (Fig. 2.8b). Thus, sonde-based propagation speeds are largest when using EQ-RKW88, smaller when using EQ-INC-FIN, and smallest using EQ-BR08. This result is in keeping with theoretical density current studies which demonstrate that the effects of a finite channel and of a compressible atmosphere should both result in slower current propagation (Benjamin 1968; Huppert and Simpson 1980; Bryan and Rotunno 2008). The mean difference between sonde-based propagation speeds and radar/satellite-based propagation speeds is 1.68 m s^{-1} when using EQ-RKW88, 0.48 m s^{-1} when using EQ-INC-FIN, and -0.15 m s^{-1} when using EQ-BR08. Thus, as assumptions are relaxed, sonde-based propagation speeds go on average from overestimating to slightly underestimating radar/satellite-based propagation speeds. These differences are all within the ±2.2 m s^{-1} uncertainty for radar-based propagation speeds.

The channel depth and compressibility effects become larger for larger fractional depths ($\frac{h}{H}$). For all sonde pairs with fractional depths greater than 0.05, the channel depth effect has a larger magnitude than the compressibility effect (Fig. 2.8b). This suggests that the infinite channel depth assumption is more impactful than the incompressible assumption in EQ-RKW88. In this dataset, the channel depth effect is up to a 20.1% reduction in propagation speed, the compressibility effect is up to an 11.0% reduction, and the combined effect of these two assumptions is up to a 28.7% reduction. The variance in radar/satellite-based propagation speeds explained by sonde-based propagation speeds is largely insensitive to whether EQ-RKW88, EQ-INC-FIN, or EQ-BR08 is used (Fig. 2.8c). This demonstrates that similar to EQ-RKW88, EQ-INC-FIN and EQ-BR08 are appropriate to use for US High Plains cold pools.

2.4.5 C^{3}LOUD-Ex Case Study: 17 May 2017

Cold pools and the atmospheric boundary layer exhibit spatiotemporal variability (Weckwerth et al. 1996; van den Heever et al. 2021; Kirsch et al. 2022; Grant and Kirsch et al. 2024). The C^{3}LOUD-Ex cold pool observed on 17 May 2017 is further examined, as a total of eight radiosondes were launched before, during, and after the passage of this cold pool. This relatively large number of sonde observations allows for a more thorough analysis of the impact of atmospheric variability on theoretical sonde-based propagation speeds.

A thorough summary of the 17 May 2017 C^{3}LOUD-Ex cold pool is presented in van den Heever et al. (2021). The information relevant to this study is as follows. Sondes were launched from two minivans – *Massive* and *Elbert* – approximately 1 km apart. These two minivans performed sonde launches at the same time and each minivan launched four sondes. The first coordinated sonde launch was before the cold pool passage (sondes E01 and M02, the first environmental sondes). The second coordinated sonde launch was after an observed shift in the winds, but before the cold pool temperature drop (sondes E02 and M03, the second environmental sondes). The final two coordinated sondes were launched after the passage of the gust front (sondes E03 and M04, the first cold pool sondes; and sondes E04 and M05, the second cold pool sondes).

Eight sonde pairs are chosen using all possible combinations of environmental and cold pool sondes launched from the same minivan (Fig. 2.9). Sonde-based propagation speeds are sensitive to both the choice of the environmental sonde and the choice of cold pool sonde (Fig. 2.9). This shows that spatiotemporal variability both inside and outside of the cold pool matters for theoretical sonde-based propagation speeds. The minimum and maximum sonde-based propagation speeds are 2.53 m s^{-1} and 7.83 m s^{-1}, respectively. Thus, there is a ~300% difference in sonde-based propagation speed depending on the timing and location of sonde launches. Radar-based propagation speeds are more sensitive to the choice of environmental sonde than the choice of cold pool sonde (Fig. 2.9), indicating that the environmental winds play a larger role in determining $\boldsymbol{V_{wind}}$ than the cold pool depth does. The winds in the second environmental sondes may have been influenced by the cold pool. However, this cold pool occurred early in the afternoon on a sunny day as the ambient temperature was rising. Temperatures in the second environmental sondes are warmer, and hence potentially more representative of the cold pool environment, than temperatures in the first environmental sondes. For this reason, the E03_E02, E04_E02, M04_M03, and M05_M03 sonde pairs (the stars in Fig. 2.9) are used for the analysis in preceding sections.

Our finding from this case study that sonde-based propagation speeds can vary by ~300% depending on the timing and location of sonde launches suggests that sub-mesoscale variability is important for cold pool propagation. This large variability seems at odds with our previous finding that the variance explained by EQ-RKW88 is high for the US High Plains environment. Note that the 17 May 2017 cold pool was aged, diffuse, and had a relatively small temperature deficit when these observations were taken. More observations of the variability in cold pools and in the boundary layer are needed to understand how this sub-mesoscale variability affects cold pool propagation speeds.

2.5 Summary and Conclusions

The density current propagation speed equation derived by Rotunno et al. (1988) (EQ-RKW88) has been applied conceptually to convective cold pools (Rotunno et al. 1988) and to modeled cold pools (Lafore and Moncrieff 1989; Trier et al. 2006; Seigel et al. 2013; Seigel and van den Heever 2013; Grant and van den Heever 2016), but only occasionally to cold pool observations (Charba 1974; Wakimoto 1982; Bryan et al. 2004, 2005; Bryan and Parker 2010). Furthermore, a thorough examination of how accurately EQ-RKW88 approximates the propagation speeds of observed cold pools has not previously been performed. A lack of targeted sonde observations inside and outside of cold pools may have prevented such a comparison in the past, but since 2016, several field campaigns have collected such targeted observations. Thus, the goal of this study has been to use these targeted observations to compare theoretical sonde-based cold pool propagation speeds – determined using EQ-RKW88 and similar equations – to cold pool propagation speeds based on radar and satellite data.

Observations from three different field campaigns were used (Fig. 2.1a-b). C^{3}LOUD-Ex (van den Heever et al. 2021) and BACS (UCAR/NCAR-Earth Observing Laboratory 2024) observed midlatitude continental cold pools over the US High Plains using radiosondes, whereas CAMP^{2}Ex (Reid et al. 2023) observed tropical maritime cold pools over the Philippine Sea and South China Sea using dropsondes. To determine theoretical sonde-based propagation speeds, pairs of sondes inside and outside of cold pools were used (Fig. 2.1c-d). Radar/satellite-based propagation speeds were determined by manually tracking cold pool boundaries in NEXRAD reflectivity (C^{3}LOUD-Ex and BACS) or true color AHI imagery from Himawari-8 (CAMP^{2}Ex) (Fig. 2.2). Radar/satellite-based propagation speeds were also corrected for advection due to the environmental wind.

The main conclusions of this study are:

- Sonde-based and radar-based propagation speeds of US High Plains cold pools are highly correlated. For BACS (C^{3}LOUD-Ex), ~69% (~84%) of the variance in radar-based propagation speeds can be explained by EQ-RKW88 (Fig. 2.3).
- Froude numbers found in this study are in keeping with past studies (Table 2.1 and Fig. 2.5). A Froude number of ~0.9-1.2 may be preferable when applying EQ-RKW88 to US High Plains cold pools.
- Theoretical sonde-based propagation speeds are insensitive to how the cold pool depth is determined (Fig. 2.6). The insensitivity of sonde-based propagation speeds to changes in cold

pool depth is due to cold pools usually having the preponderance of their negative buoyancy near the surface.

- The infinite channel depth and incompressibility assumptions used to derive EQ-RKW88 can result in increases in theoretical sonde-based propagation speeds of up to 20% and 11%, respectively, for the cases analyzed here (Fig. 2.8). The infinite channel depth assumption is more impactful than the incompressible assumption in EQ-RKW88.
- Finally, within a single cold pool, theoretical sonde-based propagation speeds can vary by ~300% based on the timing and locations of sonde launches (Fig. 2.9), suggesting that sub-mesoscale spatiotemporal variability could have an important influence on cold pool propagation speeds.

There are several potential limitations to this study. The sample size of CAMP^{2}Ex cold pools was too small for statistical conclusions about Philippine Sea and South China Sea cold pools to be drawn (see section 3c). Radar/satellite-based propagation speeds are determined subjectively, and an uncertainty of ±2.2 m s^{-1} in radar-based propagation speeds is estimated. Analysis of error suggests this uncertainty may be insensitive to cold pool propagation speeds (Fig. 2.4b). Cold pool soundings and environmental soundings were assumed to be representative of conditions inside of cold pools and their surrounding environments, respectively. As shown in Fig. 2.9, atmospheric variability within a cold pool and its surrounding environment can be substantial, which introduces uncertainty in the representativeness of each sonde. Some environmental sondes may have been influenced by nearby convection as well. While different storm morphologies, cold pool ages, or colliding/non-colliding cold pools may influence cold pool propagation speeds (see the last paragraph of section 2), we do not distinguish between them. Factors such as surface drag and the downward transport of momentum in sheared environments are neglected in this study as they are not considered in EQ-RKW88 and difficult to estimate with observations. Surface drag will slow cold pools, while downward momentum transport could increase or decrease cold pool propagation speeds.

The results presented here lead to several suggestions for both researchers and forecasters. EQ-RKW88 appears to be appropriate to use when nowcasting, forecasting, parameterizing, and/or modeling US High Plains cold pools. More observations are needed to understand EQ-RKW88's applicability in tropical oceanic and other environments, and to understand how storm morphology, cold pool age, and cold pool mergers/collisions affect cold pool propagation speeds. Future field campaigns should also aim to observe the impacts of sub-mesoscale spatiotemporal variability on cold pool propagation. Objective methods for tracking cold pools in both radar and satellite data would reduce uncertainty in propagation speeds and be useful to compare to each other. An evaluation of the propagation speed equations used in this study to cold pools in numerical simulations is another potential area for new research.

EQ-RKW88 and similar theoretical equations have been applied to cold pools for over 50 years. By using novel observations, this study confirms that EQ-RKW88 accurately approximates the propagation speeds of midlatitude continental cold pools within current estimates of error.

2.6 Tables and Figures

Table 2.1. Cold pool Froude numbers and propagation speeds from the published literature.

Study	**Froude Number**	**Propagation speed ($m\ s^{-1}$)**	**Simulated or observed**	**Location**
Farquharson (1937)	0.9	10	Observed	Sudan
Charba (1974)	1.25	20	Observed	Oklahoma
Goff (1976)	N/A	8.1 to 18.6	Observed	Oklahoma
Wakimoto (1982)	0.71 to 0.87	7 to 20	Observed	Illinois
Droegemeier and Wilhelmson (1987)	0.8 to 1.6	6.9 to 23.4	Simulated	Idealized
Intrieri et al. (1990)	0.43 to 1.7	4.1 to 15	Observed	Colorado
Weckwerth and Wakimoto (1992)	N/A	~15	Observed	Alabama
Lothon et al. (2011)	0.74	4.4 to 6.7	Observed	Niger
Heinold et al. (2013)	N/A	~10	Simulated	Mauritania
Grant and van den Heever (2016)	N/A	7.15 to 12.33	Simulated	Idealized
Borque et al. (2020)	N/A	6.7	Observed	Oklahoma
Luchetti et al. (2020a)	N/A	~1 to ~15	Observed	New Mexico and Arizona
Wills et al. (2021)	N/A	12.5 to 21.67	Observed	Tropical Pacific
Simoes-Sousa et al. (2022)	N/A	~5 to ~25	Observed	Bay of Bengal

Table 2.2. Logistical and sonde information for the C^{3}LOUD-Ex, BACS, and CAMP^{2}Ex field campaigns. Note “SE-lines” refers to the lines connecting the starting and ending points.

Campaign Name	C^{3}LOUD-Ex	BACS	CAMP^{2}Ex
Location	N Colorado, S Wyoming, E Nebraska, USA	N Colorado, USA (Central Plains Experimental Range)	Philippine Sea and South China Sea
Dates	July 2016, May-June 2017	May-June 2022 and 2023	August-October 2019
Mobile or Fixed Site	Mobile (Minivans)	Fixed Site	Mobile (NASA P-3)
Sonde Type	iMet-1-ABxn radiosondes	iMet-4 radiosondes	Vaisala RD41 dropsondes
# of sonde pairs analyzed	15	16	5
# of cold pools analyzed	6	12	4
Median, max distance between sonde pairs (km)	<1,16.7	<1,<1	49.4,78.6
Median, max time between sonde pairs (min)	23,48	30,69	13,32
Median, max distance between environmental sondes and SE-lines (km)	<1,8.1	1.1,1.9	35.9,50.0
Median, max distance between cold pool sondes and SE-lines (km)	<1,7.4	1.1,1.9	14.3,28.8
# of cold pools from scattered, multicellular, supercellular convection	2,2,2	8,4,0	2,2,0
# of cold pools dissipating when sampled	2	5	1
# of cold pools which merged with another boundary	3	9	2

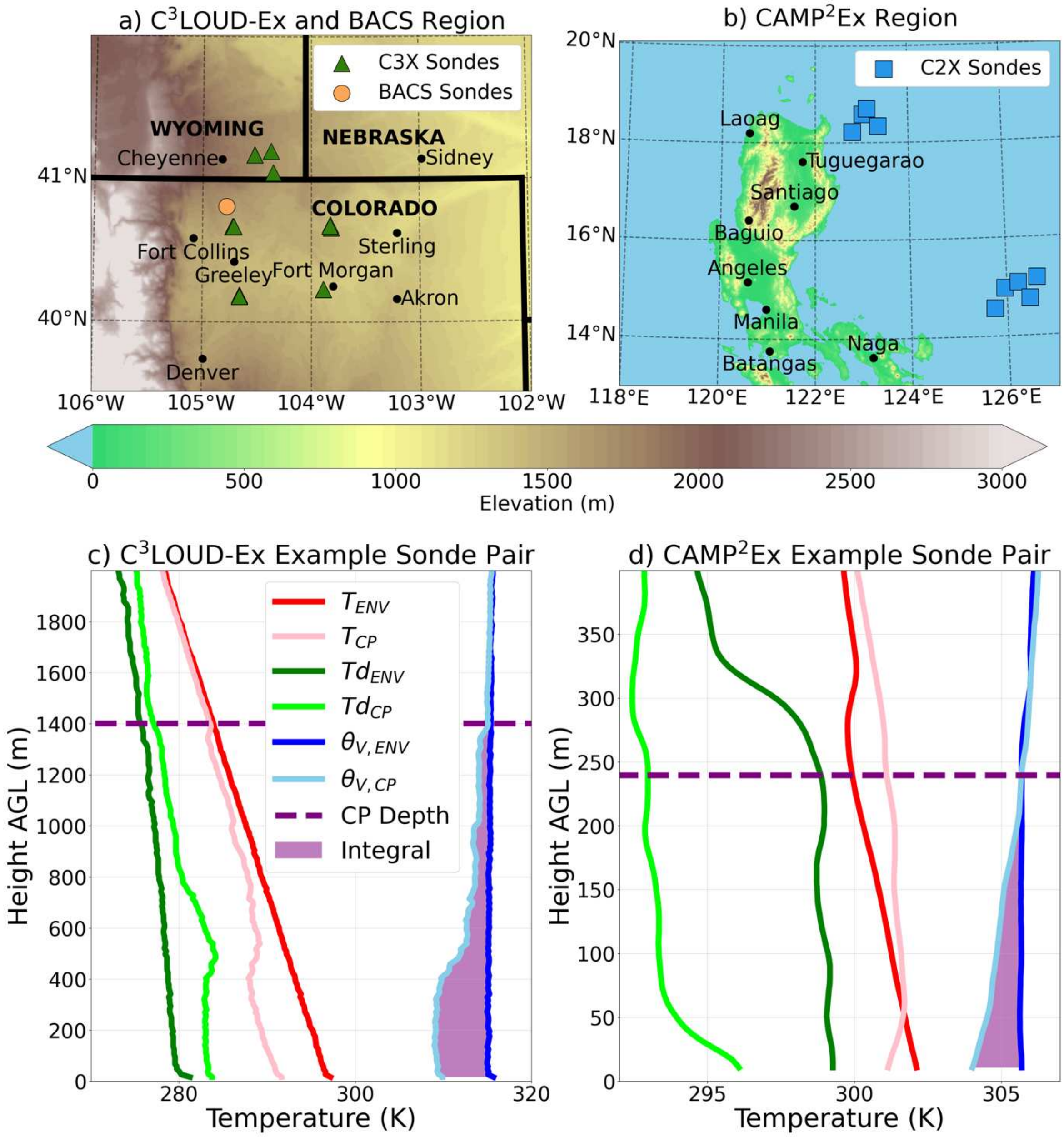

Figure 2.1. **Locations of C^{3}LOUD-Ex, BACS, and CAMP^{2}Ex soundings used in this study and example soundings from these midlatitude continental and tropical oceanic environments**. (a) Map of the US High Plains showing C^{3}LOUD-Ex soundings (dark green triangles) and the fixed site for all BACS soundings (the light orange circle). (b) Map of the Philippines, the South China Sea, and the Philippine Sea showing CAMP^{2}Ex soundings (blue squares). In (a) and (b), the shading represents topography and population centers are indicated (labeled black circles). (c) Temperature (red, pink), dewpoint (green, lime), virtual potential temperature (blue, sky-blue), cold pool depth (purple dashed lined), and a visual representation of the integral in EQ-RKW88 (purple sharing) with height for the environmental sonde (darker colors) and the cold pool sonde (lighter colors) of the C^{3}LOUD-Ex example sonde pair. (d) As in (c) but for the CAMP^{2}Ex example sonde pair. Note the axes limits differ between (c) and (d).

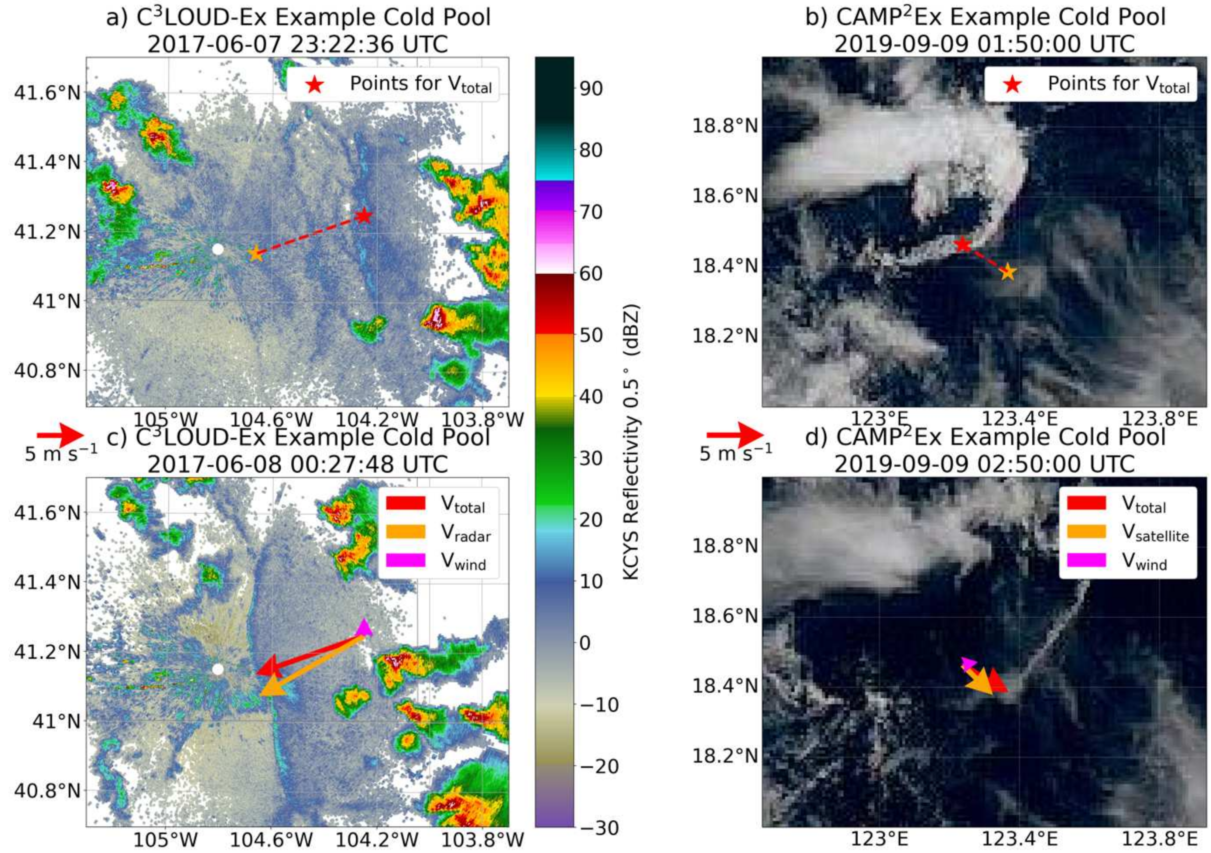

Figure 2.2. **Demonstration of how radar-based and satellite-based propagation speeds are determined**. (a) The pair of points used to determine V_{total} (red and orange star connected by red dotted line) for the C^3LOUD-Ex example sonde pair overlaid on NEXRAD reflectivity (color shading) from KCYS. (c) As in (a) but showing V_{total} (red vector), V_{radar} (orange vector), and V_{wind} (magenta vector) for this sonde pair. (b,d) Analogous to (a,c) but for the CAMP^{2}Ex example sonde pair and Himawari 8 AHI visible imagery.

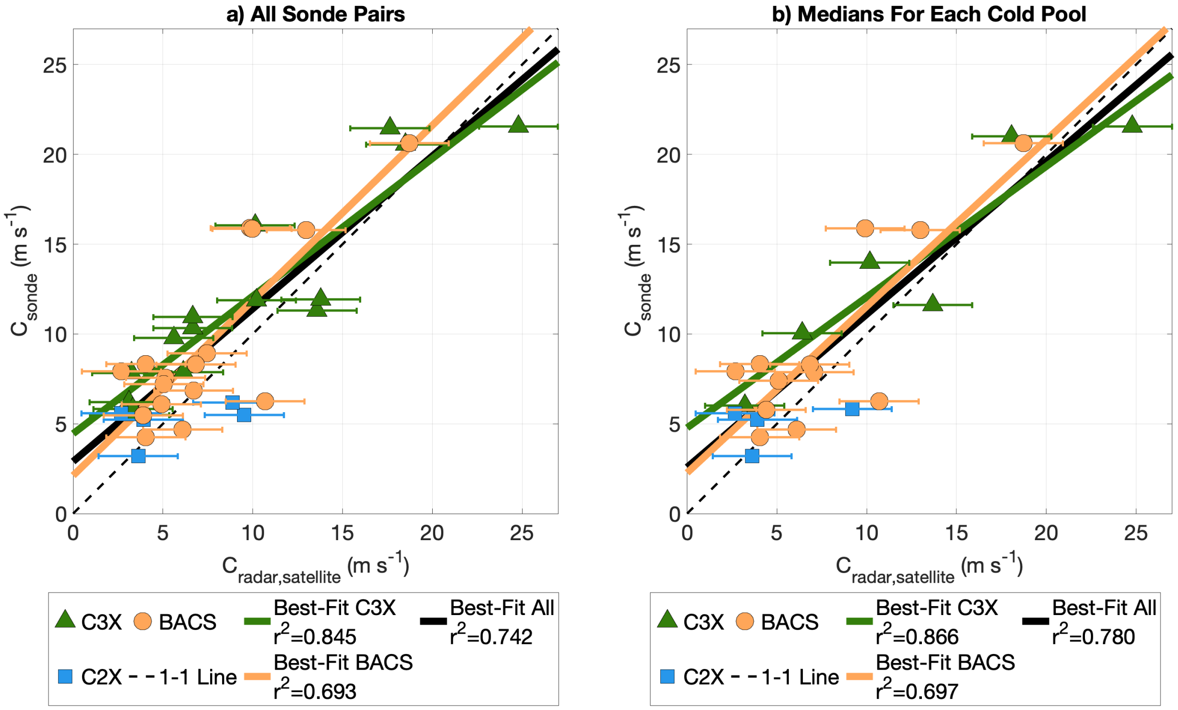

Figure 2.3. **High correlations between radar/satellite-based propagation speeds and sonde-based propagation speeds for the US High Plains**. (a) Scatterplot of sonde-based propagation speeds versus radar/satellite-based propagation speeds for all C^{3}LOUD-Ex (dark green triangles), BACS (light orange circles), and CAMP^{2}Ex (blue squares) sonde pairs with best-fit lines for C^{3}LOUD-Ex (dark green), BACS (light orange), and all points (black) along with a one-to-one line (black dashed). Error bars indicate the 2.2 m s^{-1} uncertainty in radar/satellite-based propagation speeds. (b) As in (a) but using median propagation speed values for each cold pool plotted.

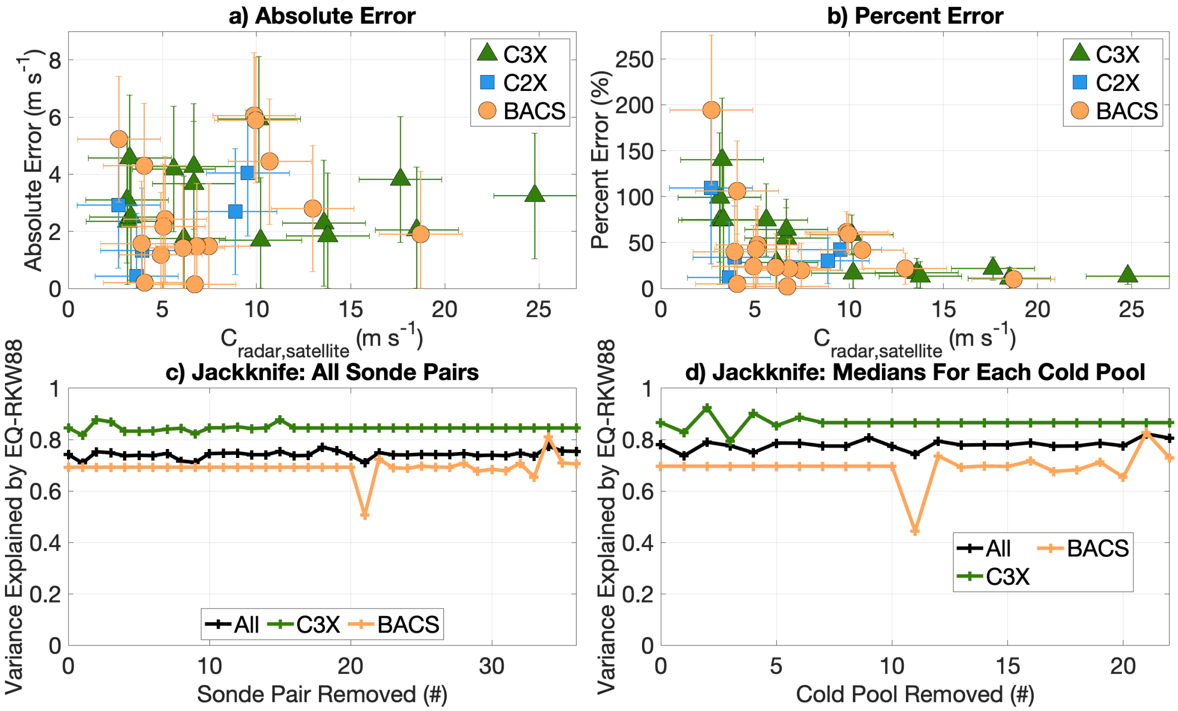

Figure 2.4. **Absolute error is insensitive to propagation speed, percent error decreases with increasing propagation speed, and results are insensitive to jackknife resampling**. (a) Absolute error in sonde-based propagation speeds versus radar/satellite-derived propagation speeds for all C^{3}LOUD-Ex (dark green triangles), BACS (light orange circles), and CAMP^{2}Ex (blue squares) sonde pairs. Error bars indicate the 2.2 m s^{-1} uncertainty in radar/satellite-based propagation speeds and resulting uncertainty in absolute error. (b) As in (a) but plotting percent error on the ordinate. (c) Variance in radar/satellite-based propagation speeds explained by sonde-based propagation speeds versus which sonde pair is removed during jackknife resampling for all (black), C^{3}LOUD-Ex (dark green), and BACS (light green) sonde pairs. (d) As in (c) but calculating statistics using the median propagation speed values for each cold pool and removing cold pools during the jackknife resampling. In (c) and (d), the abscissa is in chronological order and the 0 value on the abscissa represents no sondes pairs/cold pools being removed during jackknife resampling.

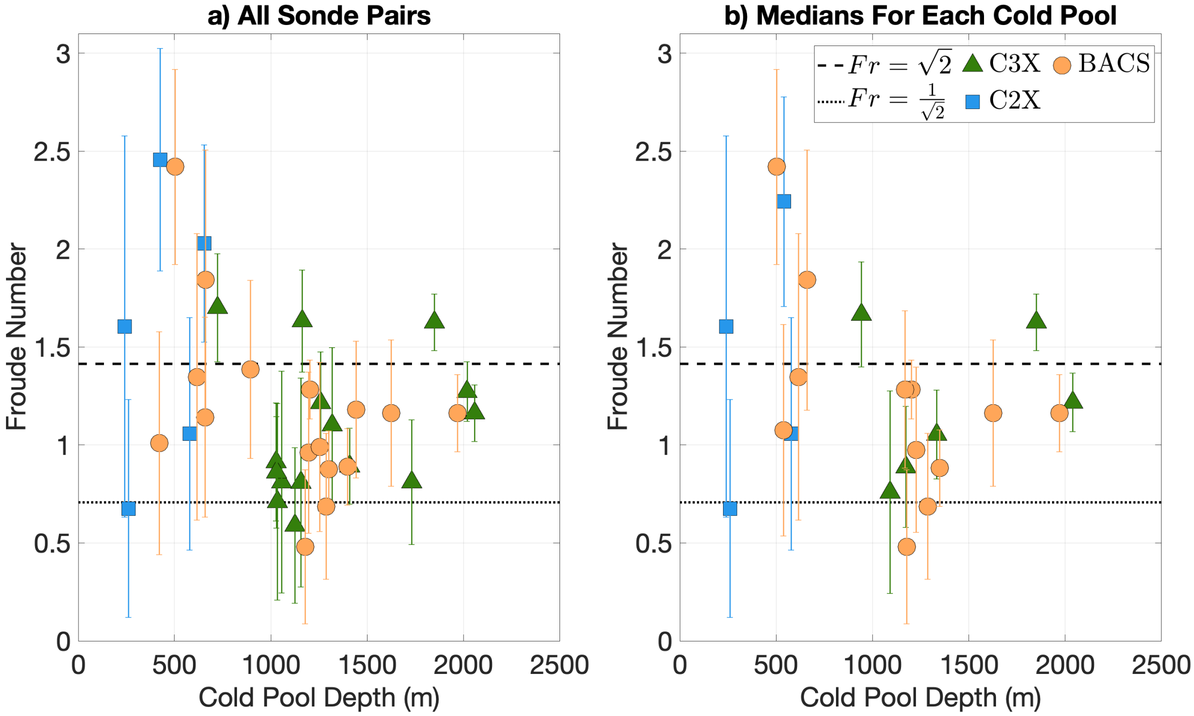

Figure 2.5. **Froude numbers are in keeping with theoretically expected values**. (a) Scatterplot of Froude numbers and cold pool depths for all C^{3}LOUD-Ex (dark green triangles), BACS (light orange circles), and CAMP^{2}Ex (blue squares) sonde pairs. Froude number of the square root of two (infinite channel depth) and the inverse square root of two (channel depth of double the current depth) are plotted as dashed and dotted lines, respectively. Error bars indicate the uncertainty in Froude number given the 2.2 m s^{-1} uncertainty in radar/satellite-based propagation speeds. (b) As in (a) but plotting median values for each cold pool.

Table 2.3. Description of the five different metrics for cold pool depth used in Figure 2.6.

Depth metric name	**Description**
Subjective	Described in section 3a
Buoyancy	Height where buoyancy first changes sign from negative to positive
Temperature	Height where temperature perturbation first changes sign from negative to positive
Direction	Lowest height where difference in wind direction between environmental sonde and cold pool sonde is less than 10°
Speed	Lowest height where magnitude of the difference between the cold pool wind vector and the environmental wind vector is less than 5 m s^{-1}

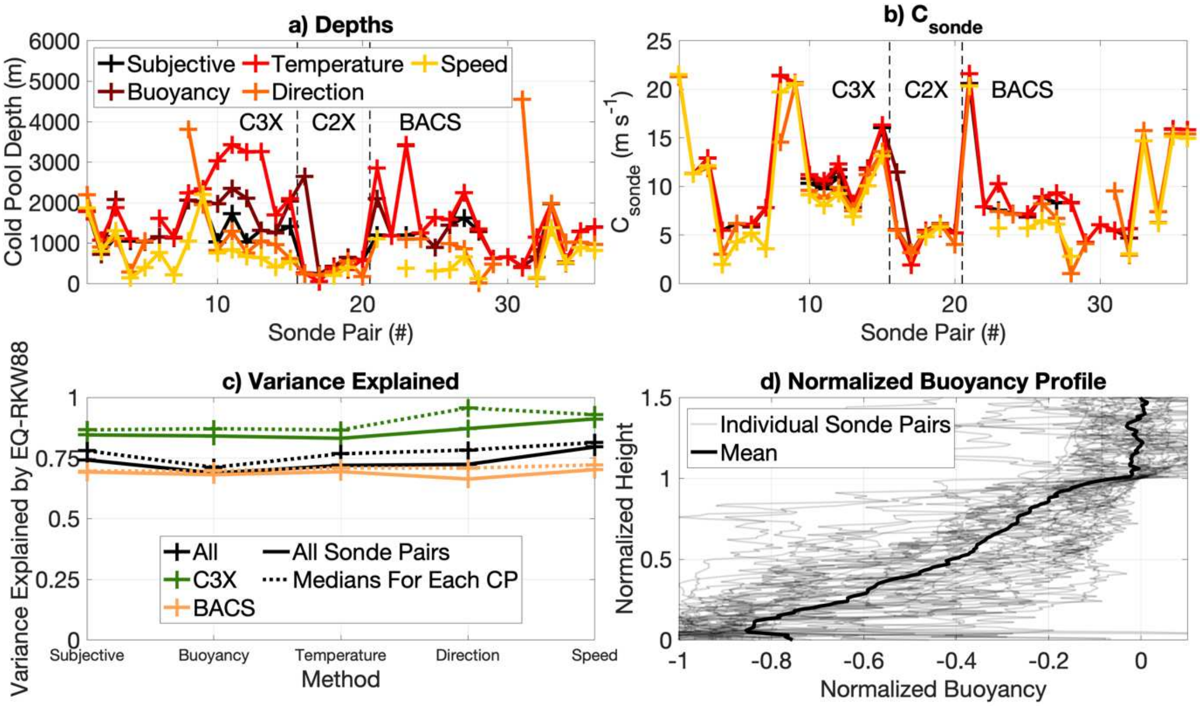

Figure 2.6. **The impacts of using various cold pool depth definitions**. (a) Cold pool depth versus sonde pair number when determining the cold pool depth subjectively (black), using buoyancy (brown), using temperature (red), using wind direction (orange) and using wind speed (yellow). Black dashed lines and text indicate which sonde pair number corresponds to which campaign. (b) As in (a) but plotting sonde-based propagation speeds on the ordinate. In (a) and (b) missing values indicate when a metric is unable to determine a cold pool depth for that sonde pair. (c) Variance in radar/satellite-based propagation speeds explained by sonde-based propagation speeds versus different methods of determining the cold pool depth for all (black), C^{3}LOUD-Ex (dark green), and BACS (light orange), sonde pairs (solid lines) and median propagation speed values for each cold pool (dashed lines). (d) Profiles of normalized buoyancy versus normalized height for all sonde pairs (light grey lines) and the mean profile for all sonde pairs (thick black line).

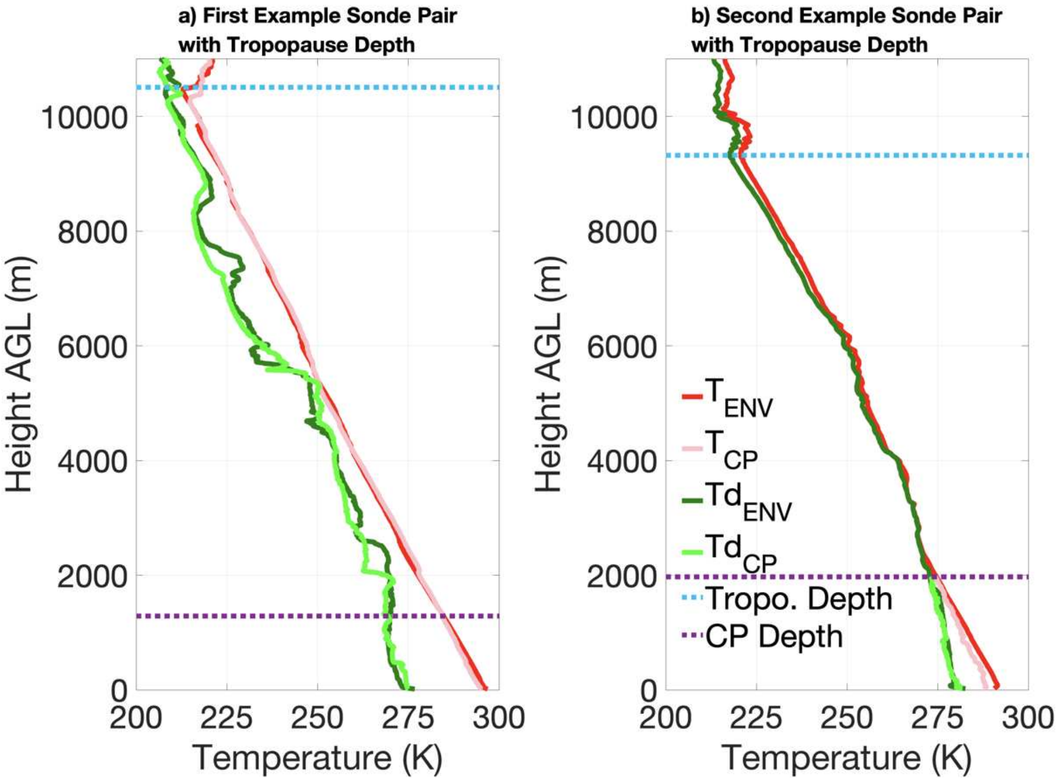

Figure 2.7. **Soundings from example sonde pairs where the tropopause depth is known**. (a) Temperature (red, pink) and dewpoint (green, lime) with height for the environmental sonde (darker colors) and the cold pool sonde (lighter colors) along with cold pool depth (purple dotted line) and tropopause depth (blue dotted line) for the first example sonde pair. (b) As in (a) but for the second example sonde pair.

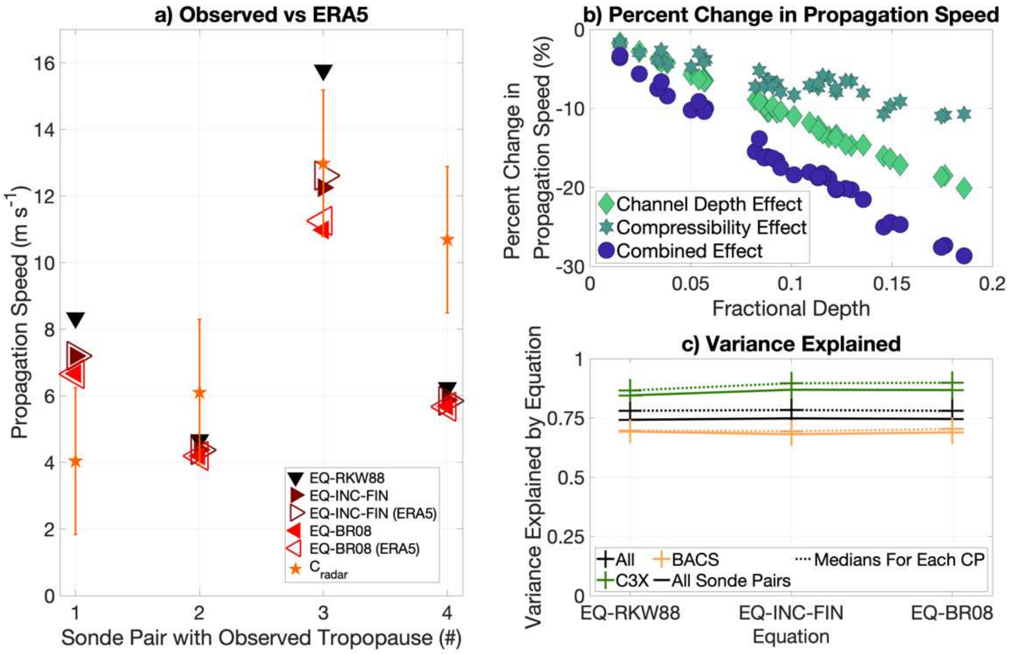

Figure 2.8. **The impact of the incompressible and infinite channel depth assumptions on propagation speeds.** (a) Propagation speeds from EQ-RKW88, EQ-INC-FIN, and EQ-BR08 using H and $\bar{\rho}$ from both environmental sondes and ERA5 (see legend) along with radar-based propagation speeds (orange stars with 2.2 m s^{-1} uncertainty) for the four sonde pairs with environmental information to the tropopause. (b) The channel depth effect (light green diamonds), compressibility effect (teal stars), and combined effect (purple circles) (see text for definition of these effects) versus fractional depth for all sonde pairs using H and $\bar{\rho}$ from ERA5. (c) Variance in radar/satellite-based propagation speeds explained by sonde-based propagation using each different propagation speed equation with H and $\bar{\rho}$ from ERA5 for C^{3}LOUD-Ex (dark green), BACS (light orange), all (black) sonde pairs (solid lines) and median propagation speed values for each cold pool (dashed lines).

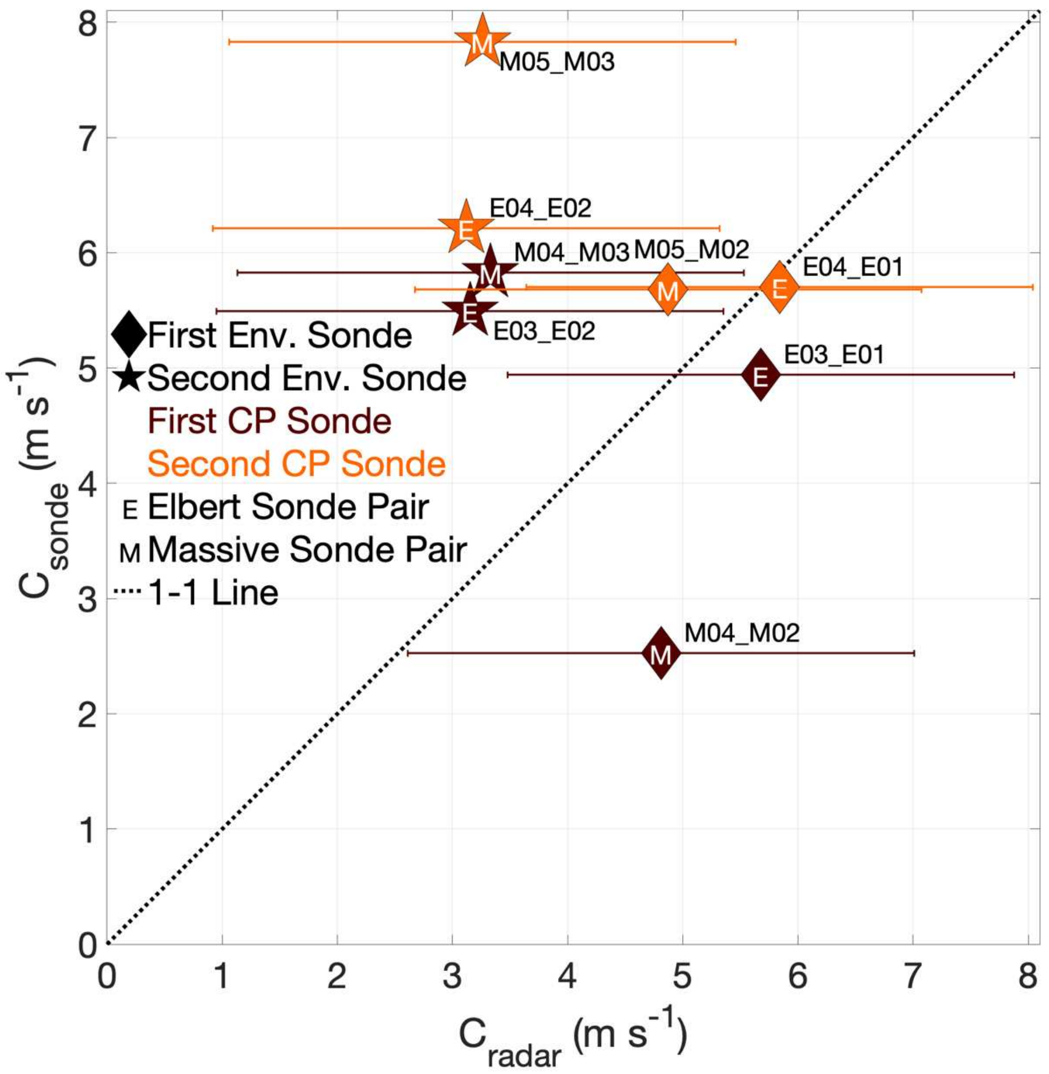

Figure 2.9. **Sonde-based propagation speeds can vary due to sub-mesoscale spatiotemporal variability**. Scatterplot of sonde-based propagation speeds versus radar-based propagation speeds for the 17 May 2017 cold pool when using the first environmental sonde (diamonds, E01 or M02) or second environmental sonde (stars, E02 or M03) and the first cold pool sonde (brown, E03 or M04), or the second cold pool sonde (orange, E04 or M05). Location of sonde pair is indicated (E for *Elbert* van, M for *Massive* van), each sonde pair is labeled with the date removed, and a one-to-one line is plotted (black dotted line). Error bars indicate the 2.2 m s^{-1} uncertainty in radar-based propagation speeds.

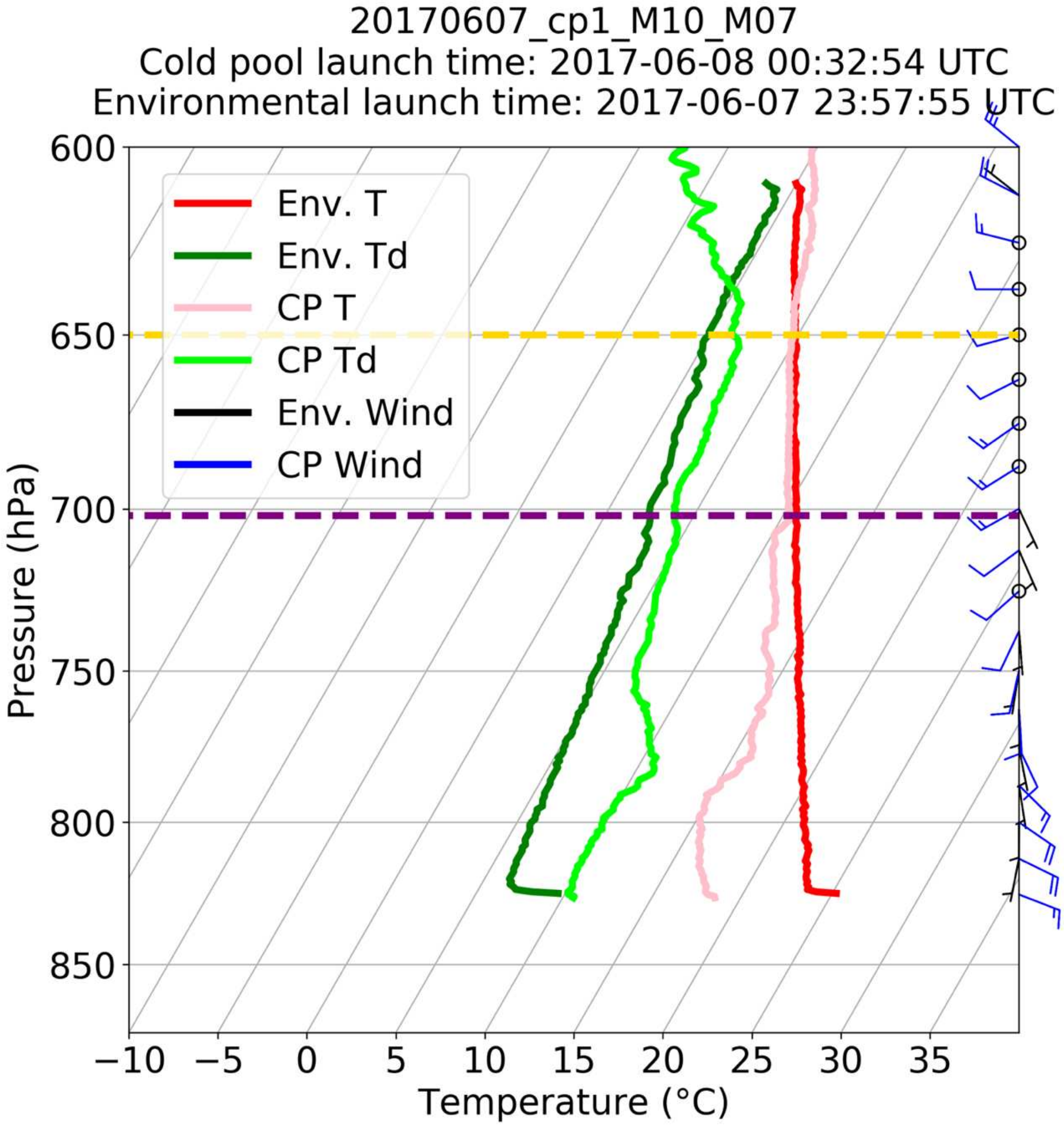

Figure 2.10. Skew-T log-p diagram of the 20170607_cp1_M10_M07 sonde pair showing temperature (environmental sonde red, cold pool sonde pink), dewpoint (environmental sonde green, cold pool sonde lime), winds (environmental sonde black, cold pool sonde blue), the buoyancy-based cold pool depth that was rejected (yellow dashed line), and the subjectively chosen cold pool depth (purple dashed line).

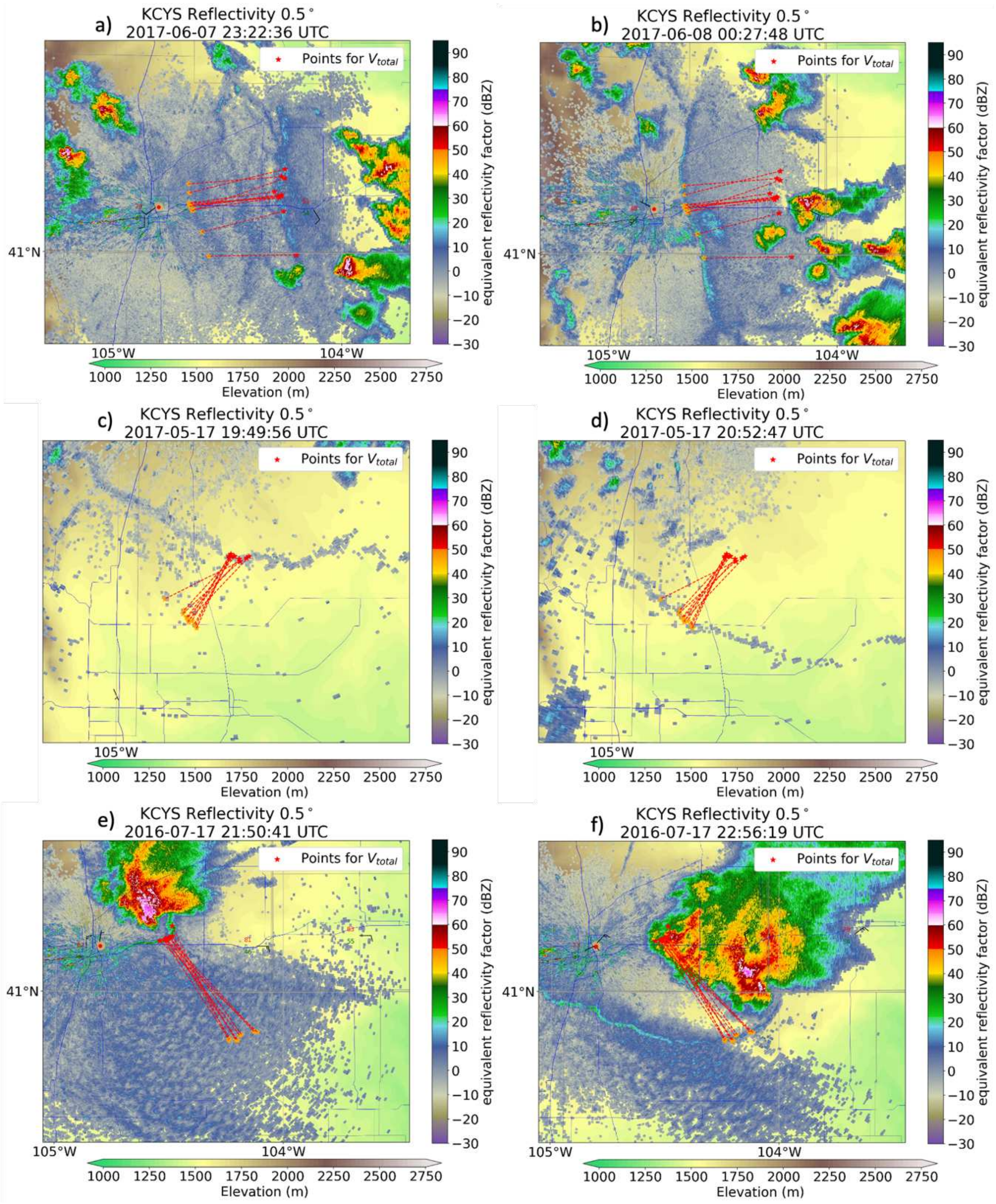

Figure 2.11. (a,b) As in Fig. 2.2a,c but showing all sets of starting and ending points chosen during the experiment discussed in this section. (c,d) as in (a,b) but for the second case analyzed (5 May 2017). (e,f) as in (a,b) but for the third case analyzed (17 July 2016).

Chapter 3: Haboobs on Slopes

3.1 Introduction

Haboobs are convective cold pools which loft mineral dust from the surface into the atmosphere (Sutton 1925). They contribute a substantial fraction of the dust emitted from the surface, for example 40-50% of the emitted dust in the Sahara (Heinold et al. 2013; Marsham et al. 2013; Bergametti et al. 2017) and 30% in the southern Arabian Peninsula (Miller et al. 2008). Understanding the processes influencing atmospheric dust loading is critical, since dust alters the atmospheric radiative balance (Sokolik and Toon 1996; Slingo et al. 2006), serves as cloud condensation nuclei and ice nuclei (DeMott et al. 2003; Field et al. 2006; Twohy et al. 2009; Seigel et al. 2013), fertilizes the oceans and the Amazon rainforest (Martin et al. 1990; Babin et al. 2004; Bristow et al. 2010), causes motor vehicle accidents by reducing visibility (Ashley et al. 2015; Lader et al. 2016; Li et al. 2018), and contributes to respiratory disease (Griffin 2007; Kanatani et al. 2010; Tong et al. 2023). Current emissions of dust are greater than preindustrial dust emissions, and these emissions may continue to increase due to climate change, land use change, and other anthropogenic activities (Neff et al. 2008; Mahowald et al. 2010; Munson et al. 2011; Ginoux et al. 2012). Despite its importance, dust emission is not well represented in weather and climate models (Knippertz and Todd 2012; Ansmann et al. 2017; Wu et al. 2020; Kok et al. 2023), and the difficulties of accurately representing haboobs in such models may be a large source of error (Walker et al. 2009; Pantillon et al. 2015, 2016; Saleeby et al. 2019; Bukowski and van den Heever 2020).

Topography can impact haboobs and dust lofting. Haboobs – and dust emissions in general – often occur in regions of complex topography such as northern Africa, the Arabian

Peninsula, and the southwest United States (Adams and Comrie 1997; Tanaka and Chiba 2006; Knippertz et al. 2007; Miller et al. 2008). The mountain-plain circulation in the Sahara driven by the Atlas and Hoggar mountains is similar to Alpine-pumping (Lugauer et al. 2003; Flamant et al. 2007). This pumping can initiate convection over high terrain, leading to the formation of haboobs which accelerate downslope (Knippertz et al. 2007; Emmel et al. 2010). The Saharan mountain-plain circulation can also redirect dust lofted by haboobs towards Iberia and lead to further dust lofting (Dhital et al. 2022). Downslope windstorms have also been shown to loft dust in North Africa and the Arabian Peninsula (Pokharel et al. 2017). Heinold et al. (2013) investigated drivers of dust emission in summertime West Africa. They speculated that topographically-driven circulations could contribute to unknown sources of dust emission, which make up ~20% of total emissions. This aforementioned research on interactions between topography, haboobs, and dust lofting has used data from observations or case study simulations. While these are useful datasets, disentangling the impacts of topography on haboobs from other factors such as synoptic forcing is not easily accomplished.

Topographic effects on cold pools more generally have been investigated using mostly observational data or case study simulations. Cold pools in Arizona, New Mexico, and Colorado have been shown to propagate more quickly downhill than uphill or over complex terrain (Luchetti et al. 2020a,b). The ambient wind appears to influence the propagation speed of Arizona cold pools (which propagated uphill), but not New Mexico (downhill propagating) or Colorado (propagating over complex terrain) cold pools (Luchetti et al. 2020a,b). Simulations have also shown that the terrain can slow (Liu et al. 2022) or even block (Mulholland et al. 2019) cold pools. Johnson et al. (2014) simulated a cold pool over the Colorado Rocky Mountains and noted hydraulic jumps on the lee side of ridgelines. Furthermore, laboratory tank density current experiments have shown that density currents behave differently on slopes compared to flat surfaces (Simpson 1997). Compared to a flat surface, density currents propagate faster downslope (Dai et al. 2012; Dai and Huang 2016; He et al. 2017) and density currents moving upslope become vertically thinner and move slower (Marleau et al. 2014; Lombardi et al. 2015; De Falco et al. 2020).

A number of other factors known to affect haboob propagation and dust lofting may be important in modulating the impact of topographic slopes on haboobs. Huang et al. (2018) (hereafter H18) tested the impact of grid spacing and prescribed surface sensible heat fluxes in idealized simulations of haboobs. They found that finer grid spacing led to greater turbulent mixing and hence haboobs which dissipated faster, propagated slower (as shown by earlier studies such as Straka et al. (1993) and Grant and van den Heever (2016)), and lofted less dust. Greater sensible heat fluxes similarly also led to faster dissipating and slower haboobs in keeping with the prior results of Grant and van den Heever (2016, 2018), but also greater dust lofting due to increased downward momentum transport. Bukowski and van den Heever (2021) (hereafter BvdH21) investigated the radiative effects of dust in case study simulations of haboobs. Scattering of shortwave radiation during the day caused colder and dustier haboobs, while absorption of longwave radiation at night caused warmer haboobs. However, the stable nocturnal surface layer caused increased haboob propagation speeds, in keeping with previous theoretical investigations of the impacts of stable layers on density currents (Liu and Moncrieff 2000; Seigel and van den Heever 2012b), as well as larger dust emission at night. Diurnal variations in haboob propagation speeds over the Sahara have also been observed (Caton Harrison et al. 2021) in support of these modeling studies. Bukowski and van den Heever (2022) (hereafter BvdH22) examined the influence of time of day, initial haboob temperature, vegetation type, soil type, and soil moisture on haboobs. They found the most important of these factors were the initial temperature and vegetation type. Colder initial temperatures drove faster propagation, faster wind speeds, and hence more dust lofting. Vegetation with greater roughness lengths decreased dust emission but also increased sensible and latent heat fluxes. BvdH22 found that interpreting the effect of vegetation type was complicated because several factors – such as roughness, albedo, and evapotranspiration – are all dependent on vegetation type. Finally, the erodible surface fraction can also influence dust emissions (Walker et al. 2009; Saleeby et al. 2019), and could in turn impact haboob propagation via radiative effects.

The objective of this study is to investigate the impact of topographic slope on daytime haboob propagation and dust lofting, along with how this impact is modulated by aerodynamic surface roughness and dust-radiative effects. Given that BvdH22 found the largest impact on haboobs from varying vegetation type was due to roughness effects, testing roughness in isolation allows for a clearer understanding of its impacts. Dust-radiative effects are also examined, since BvdH21 showed that these factors influence haboob propagation and dust lofting. To achieve our objective, we run a suite of 40 idealized haboob simulations where topographic slope, surface roughness, and aerosol-radiative effects are independently and simultaneously varied. In contrast to many previous studies which have used observational data or case study simulations, this suite of idealized simulations allows for the impacts of topographic slope, surface roughness, and aerosol-radiative effects to be more clearly disentangled from each other, thereby removing potentially confounding factors (e.g. synoptic forcing). A unique algorithm is developed to track the boundaries of haboobs and determine propagation speeds. The simulations are analyzed to understand how and why the chosen factors (slope, roughness, and aerosol-radiative effects) impact haboob propagation and dust lofting. Our findings shed new light on fundamental haboobs processes and should be useful in improving the representation of haboobs and associated dust lofting in forecast and climate models.

3.2 Methods

3.2.1 Model Setup

The suite of idealized simulations is run using the Regional Atmospheric Modeling System (RAMS) version 6.3.02 (Pielke et al. 1992; Cotton et al. 2003; Saleeby and van den Heever 2013; van den Heever et al. 2022). The objective of this study is not to simulate haboobs in a specific region but rather represent haboob processes in conditions broadly representative of haboob environments. As such, we conduct idealized simulations of haboobs, as opposed to specific case studies, which allows us to more easily isolate and hence disentangle the effects we are interested in, as well as draw more generalized conclusions about haboob processes. To simplify the analysis, simulations are run without moisture or microphysics. Horizontal (vertical) grid spacings of 100 m and (50 m) are used as previous studies have shown such grid spacings are needed to accurately simulate cold pools and their interactions with the surface (Grant and van den Heever 2016; Hirt et al. 2020; Fiévet et al. 2023). Terrain-following sigma coordinates are used for the vertical coordinate system. The vertical grid spacing is constant and not stretched over flat terrain. In simulations with sloped topography, the vertical grid spacing varies between 29 m and 50 m based on both the height of the topography and the height above ground level. The idealized model domain is 80 x 160 x 10 km in the zonal, meridional, and vertical directions, respectively. Cyclic lateral boundaries are used. A damping layer is applied near the rigid model top to prevent the reflection of gravity waves. The topography varies only in the meridional direction. The southern half of the domain slopes linearly upwards to a peak in the meridional center. The topography in the northern half of the domain is then a mirror image of the southern half, sloping downward toward the northern boundary (Figure 3.1a). The topographic slopes tested are discussed further in section 2.3.

Radiative tendencies are updated either every 10 min or every 1 min (see section 2.3 for further details). The radiation parameterization assumes a flat surface, so the southern and northern halves of the domain receive nearly identical amounts of solar radiation at the surface. Only the central latitude, central longitude, and simulation starting time affect the parameterized radiation (Harrington 1997; Stokowski 2005). The settings for these parameters are chosen to be representative of daytime haboobs occurring in the southwestern United States (Table 3.1) (Adams and Comrie 1997). The Land-Ecosystem-Atmosphere-Feedback version 3 (LEAF-3) (Walko et al. 2000) model coupled to RAMS is used to simulate an interactive land surface. All simulations use a horizontally homogenous bare soil desert with silty clay loam soil (59% clay). These conditions were chosen because they are generally representative of environments in which haboobs form and were also tested by BvdH22. Subgrid turbulence is parameterized following Smagorinsky (1963) with modifications from Lilly (1962) and Hill (1974). No aerosols other than dust are included. No Coriolis force is applied as it would have little effect given the short duration of these simulations. A full summary of the model settings is provided in Table 3.1.

Simulations consist of an initial spin-up phase, during which a turbulent boundary layer is allowed to develop, and a subsequent analysis phase, during which haboobs are initiated by releasing cold bubbles. This follows the approach of BvdH22. Simulations are initialized in the spin-up phase with a horizontally homogeneous atmospheric sounding with zero winds and a constant Brunt-Väisälä frequency of 0.005 s^{-1}. These weak statically stable conditions are used to prevent the turbulent boundary layer from growing unphysically deep. At sea level, the initial sounding has a surface temperature of 28.4 °C (based on the 0Z Tucson sounding from 1984-08-10) and a surface pressure of 1000 hPa. These values were chosen to be consistent with the time and location (southwestern United States) specified for the radiation parameterization. Density current propagation is more strongly modulated by the temperature difference between the current and its surroundings than the temperature of the current/surroundings in isolation (Benjamin 1968). Thus, while we chose conditions based on the southwestern United States, choosing conditions based on a different region (e.g. the Sahara or the Arabian Peninsula) would likely have led to similar results.

At the start of the spin-up phase, random potential temperature perturbations of amplitude 0.1 K are added to the lowest 500 m of the domain to break symmetry. Simulations are integrated for 90 minutes during the spin-up phase. After the spin-up phase is completed, the simulations are restarted with one dome-like cold bubble added to both the southern and northern halves of the domain. Each of these two cold bubbles has a horizontal radius of 6000 m, a vertical radius of 4000 m, is cosine smoothed, and is centered in its respective domain half (Figure 3.1a-b). These initial cold bubbles are also centered at the surface (i.e. the bubble is a dome extending to 4 km above the surface) to facilitate tracking of the haboob boundary. Simulations are then integrated for another 90 min during the analysis phase, after which the haboobs have almost entirely dissipated. All of the figures below show data from the analysis phase, and all times discussed in this paper are relative to the start of the cold bubble introduction and hence start of the analysis phase.

3.2.2 Dust Emission

Dust mass flux from the surface F_p in RAMS is parameterized (Smith 2007; Seigel and van den Heever 2012a; Saleeby and van den Heever 2013) based on the GOCART scheme (Ginoux et al. 2001), where

$$F_p = \begin{cases} E_{z0} C s_p u_h^2 (u_h - u_{t,wet}^*), & u_h > u_{t,wet}^* \\ 0, & u_h \leq u_{t,wet}^* \end{cases} \quad (3.1).$$

In Equation 3.1, E_{z0}, C, s_p , and $u_{t,wet}^*$ are constants described as follows. The erodible surface fraction E_{z0} is calculated following Pierre et al. (2012) and reduces dust emissions with an increasing vegetation roughness length. In this study, E_{z0} is always 1 since the soil roughness, and not the vegetation roughness, is varied in the sensitivity experiments. A constant dust scaling factor C of $1.153 \times 10^{-16}\ g\ s^2\ cm^{-5}$ is used to scale emissions to a global annual value of 1851 Tg (Ginoux et al. 2001; Saleeby and van den Heever 2013). Dust mass flux is calculated separately for seven radius bins p, and these are ultimately converted to a submicron bin and a supermicron bin which RAMS tracks. The constant factor s_p is chosen such that ~10% (~90%) of lofted dust mass is in the submicron (supermicron) bin (Tegen and Fung 1994; Seigel and van den Heever 2012a). The threshold friction velocity $u_{t,wet}^*$ is calculated following Marticorena and Bergametti (1995) with an adjustment for soil moisture by Fécan et al. (1999). Simulations in this study are dry, so $u_{t,wet}^*$ is constant for each of the bins. The only variable in Equation 3.1 is the 10 m wind speed u_h, which is calculated by assuming a logarithmic wind profile from the wind speed at the lowest model level. Importantly, RAMS assumes a constant roughness length of 0.05 m when calculating u_h. This means that over surfaces with roughness lengths greater (less) than 0.05 m, values ofu_h and diagnosed dust fluxes will be higher (lower) than if the roughness length used in other parts of the model were used to calculate u_h. Given this setup,F_p only varies with u_h. Dry deposition of dust is enabled. Readers interested in further details of the dust scheme in RAMS are referred to Saleeby and van den Heever (2013) and Seigel and van den Heever (2012a).

The effect of low-level winds on dust lofting is evident in Figure 3.1, which shows the output from an example simulation. Most of the dust mass is at the leading edges of the haboobs (Figure 3.1c-d). This is due to the fastest wind speeds being located at the leading edges of the haboobs (not shown).

3.2.3 Sensitivity Experiments

All combinations of five topographic slopes, four surface roughness lengths, and two aerosol-radiative settings are tested giving a total of 40 simulations. The five different topographic slopes are grades of 0% (i.e. flat ground), 1%, 2%, 3%, and 5% (hereafter named SLOPE-0, SLOPE-1, SLOPE-2, SLOPE-3, and SLOPE-5 respectively). For example, Figure 3.1a shows topography with a grade of 2% (SLOPE-2) where the terrain rises 1.6 km over a horizonal distance of 80 km. These slopes were chosen based on analysis of topography in the southwestern United States. The Summit of Brown’s Peak in Arizona to the confluence of the Salt River and Verde River has a point-to-point slope of ~5.28%. However, this is only over a horizontal distance of 35.5 km and not 80 km. SLOPE-5 is included here an extreme case but is within the realm of slopes that exist over shorter horizontal scales. SLOPE-3 is chosen since the Summit of Mount Lemmon to the Gila River in Cochran, AZ has a point-to-point slope of ~2.76% over a horizontal distance of 82.6 km. SLOPE-2 and SLOPE-1 are tested to represent gentler and less extreme topographic slopes. The flat ground SLOPE-0 serves as the control.

As discussed previously, two dome-like cold bubbles are initially centered on the northern and southern halves of the domain in each simulation. In our analysis, the northern and southern domain halves of each simulation are treated independently of each other. All southern cold bubbles have initial minimum potential temperature perturbations of -10 K, based on BvdH22. For the northern cold bubbles, the temperature perturbations are scaled such that the latent cooling required to produce them is the same as to produce a -10 K cold bubble on flat ground at sea level. Since the air density is lower at higher elevations but the latent cooling required to produce the initial bubbles is being held constant, the northern cold bubbles become slightly colder as the topographic slope increases. The northern cold bubbles are included to test the effects of this alternative setup. The northern haboobs do propagate slightly faster and loft a little more dust than their southern counterparts due to being slightly colder (not shown). However, the northern haboobs produce broadly similar results to the southern haboobs, so northern haboob results are not shown, other than in Figures 3.1 and 3.2.

The four surface roughness lengths tested are 0.001 m, 0.034 m, 0.066 m, and 0.100 m (hereafter named ROUGH-001, ROUGH-034, ROUGH-066, ROUGH-100 respectively). These correspond to the roughness lengths of the four different vegetation types tested in BvdH22 (desert, short grassland, semidesert, and crop-grassland respectively). BvdH22 found that the impact of vegetation type on haboobs was dominated by changes in roughness but complicated by changes in other factors such as albedo or the erodible surface fraction. Hence, in this study, only the soil roughness is varied, and other factors including the erodible surface fraction and albedo are held constant to isolate the impact of roughness on haboobs. Greater roughness will lead to a greater downward transport of momentum at the surface, in turn causing greater sensible and latent heat fluxes (BvdH22).

Simulations are run with both radiatively interactive dust (DUSTRAD-ON) and radiatively inert dust (DUSTRAD-OFF). Dust has a complex index of refraction of 1.53+0.003i, based on observations by Haywood et al. (2003) and testing of the RAMS dust-radiation scheme by Stokowski (2005). Radiative tendencies are updated every 1 min in the analysis phase of DUSTRAD-ON simulations. For computational expediency, radiative tendencies are updated every 10 min in the spin-up phase of all simulations and in the analysis phase of DUSTRAD-OFF simulations. A DUSTRAD-OFF simulation was simulated with radiative tendencies updated every 1 min and was found to be nearly identical to a simulation with tendencies updated every 10 min (not shown). The simulations are named using their topographic slope, surface roughness length, and dust-radiation setting. For example, the SLOPE-2_ROUGH-034_DUSTRAD-ON simulation shown in Figure 3.1 has a 2% topographic slope, a 0.034 m surface roughness length, and uses radiatively interactive dust.

3.2.4 Analysis Approach

An algorithm was developed to track the boundaries of the haboobs in time, thereby objectively determining propagation speeds. For each haboob, this algorithm first determines the 25 m AGL potential temperature perturbation θ', converts θ' to polar coordinates centered in the middle of the haboob, and smooths θ' to θ'_{smooth}. Haboob boundary points $\boldsymbol{b}$ are then determined by applying a $-0.5\ K$ temperature threshold to θ'_{smooth}. Two checks are used to identify and remove any "lost haboob boundary points" which are points of boundary layer turbulence that the algorithm identifies as the haboob boundary. Finally, radial interpolation of the remaining haboob boundary points is performed to recover values for the lost haboob boundary points. The algorithm is described in detail in the following section. For a given time t and angle ϕ, the vector $\boldsymbol{b}$ yields an (x, y) coordinate pair. Note $\phi = 0$ points east and ϕ increases moving counterclockwise around haboobs (Figure 3.1c). The haboob tracking algorithm uses 1588 angles in polar coordinates, so at each time, 1588 haboob boundary points are identified for each haboob. Haboob boundary points are shown for the example haboobs demonstrated in Figure 3.1b,c. Propagation speeds are calculated as a function of time, and the mean is taken over all haboob boundary points for each haboob, the results of which are shown in Figure 3.2a. Haboobs accelerate for the first ~10 min of simulations and then begin to decelerate. Figure 3.2b shows the percentage of lost haboob boundary points that must be recovered by radial interpolation. Haboob boundaries are not tracked after 30 min, as the number of lost haboob boundary points increases substantially after ~25 min due to the dissipation of the simulated haboobs. In all subsequent figures, haboob propagation speeds $v(\phi)$ are always calculated by taking the mean propagation speed between 10 min and 30 min:

$$v(\phi) = \frac{\|\boldsymbol{b}(30\ min,\phi)-\boldsymbol{b}(10\ min,\phi)\|}{20\ min}. \tag{3.2}$$

Thus, $v(\phi)$ represents the mean propagation speed of haboobs after their initial acceleration but before they have dissipated to the point of becoming difficult to identify and track. Results are not sensitive to the starting time chosen for $v(\phi)$. When $v(\phi)$ is recalculated using a starting time of 15 min (not shown), haboob propagation speeds decrease, but the trends in haboob propagation speeds with changing slope, roughness, and dust-radiative interactions are mostly unchanged.

Identifying the haboob boundary points allows for the identification of model gridpoints located within specific regions of haboobs. Figure 3.1e,f shows how each haboob can be subdivided into a downslope region and an upslope region. These two regions can also be considered together to yield all model grid-points inside of a haboob. Additionally, it is sometimes useful to add an additional 1 km buffer when looking at points within haboobs since some dust is slightly ahead of our thermodynamically defined haboob boundary. These 1 km buffers are also shown in Figure 3.1e,f. The internal haboob regions are determined for every haboob at every output time between 1 min and 30 min (i.e. when haboob boundary points can be identified).

3.2.5 Tracking Algorithm

The algorithm which tracks haboob boundaries in time is described as follows. The algorithm begins by reading in potential temperature data $\theta(t,x,y)$ that has been interpolated to 25 m AGL. The three rows/columns of points nearest to the lateral boundaries of the domain are removed, as these points are repeated to facilitate periodic boundaries in RAMS. Hence, x runs from 0 to 793 and y runs from 0 to 1593. The temporal dimension is represented by t.

The algorithm determines a base state for θ in the following way. First, θ_1 is calculated for a given t and y as

$$\theta_1(t,y) = \frac{\theta(t,0,y)+\cdots+\theta(t,14,y)+\theta(t,779,y)+\cdots+\theta(t,793,y)}{30}. \tag{3.3}$$

By taking a mean of 15 points near each of the east and west boundaries, θ_1 is not influenced by the haboobs. For the 0% topographic slope simulations, the base state potential temperature does not vary with y and is simply calculated as the mean of θ_1 over all y points:

$$\overline{\theta_{flat}}(t) = \frac{1}{1594}\sum_{y=0}^{1593} \theta_1(t,y)\ . \tag{3.4}$$

This is similar to how BvdH22 calculated base state potential temperature. On sloped terrain, θ_1 varies with y, so a mirrored base state is desirable. Thus we define

$$\theta_2(t,y') = \frac{1}{2}[\theta_1(t,y') + \theta_1(t,1593-y')] \tag{3.5}$$

where y' runs from 0 to 796 instead of 0 to 1593. Next, for each output time, θ_3 is defined by fitting a cubic polynomial to θ_2 in y, which smooths out the remaining noise. A cubic fit was used because a linear fit and a quadratic fit were determined to produce excessive smoothing. For sloped terrain, the base state potential temperature is

$$\overline{\theta_{sloped}}(t, y) = \begin{cases} \theta_3(t, y), \ y \leq 796 \\ \theta_3(t, 1593 - y), \ y > 796 \end{cases}. \tag{3.6}$$

Finally, the potential temperature perturbation is defined as

$$\theta'(t, x, y) = \begin{cases} \theta(t, x, y) - \overline{\theta_{flat}}(t), \ slope = 0\% \\ \theta(t, x, y) - \overline{\theta_{sloped}}(t, y), \ slope > 0\% \end{cases}. \tag{3.7}$$

Once θ' has been determined, the next step in the algorithm is to find the haboob boundary points. Since there are two haboobs in the model domain, the southern half of the domain and the northern half of the domain are hereafter considered separately. The process for each domain-half is analogous and is described as follows. For either half of the domain, θ' is converted to polar coordinates with radius r and angle ϕ. Note $\phi = 0$ points east and ϕ increases when moving counterclockwise around haboobs (Figure 3.1c). The number of angles used is 1588, as the python package used to perform the polar transformation determines this is the smallest number of angles for which no information is lost during the transformation. The origin of the polar coordinates used corresponds to the center of the half of the domain being considered. The origin also corresponds to the center of the initial cold bubble and subsequent haboob. Next, θ' is smoothed in the angular dimension using a triangular weighting function spanning ~6.8°. This smoothing likely removes some of the lobe and cleft instabilities along the boundary of the haboob. However, the smoothing removes much of the noise in the boundary layer surrounding the haboob, and thus makes false detections of the haboob boundary much less frequent. Haboob boundary points can be identified from the new θ'_{smooth} field. The haboob boundary point β at a given angle ϕ and time t is found via

$$\beta(\mathrm{t}, \phi) = \max\{r : \theta'_{smooth}(t, r, \phi) < -0.5 \ K\}. \tag{3.8}$$

The haboob boundary points are next quality controlled to ensure they are accurately tracking the haboob boundary. Since haboobs expand radially, values of β are flagged as invalid if β decreases with time. Haboob boundary points which are flagged as invalid are referred to as "lost haboob boundary points". A "jump threshold" is next implemented. If a haboob boundary point moves on average faster than 50 m s^{-1} between two times, then the value of β is flagged as invalid at the latter time. This jump threshold helps remove haboob boundary points which accidentally identified boundary layer turbulence ahead of the haboob instead of the haboob boundary. Since this misidentified turbulence is often well ahead of the haboob, such haboob boundary points jump an unrealistic distance from one time to another and are thus caught by the jump threshold. Note from Figure 3.2a that mean haboob propagation speeds do not exceed 12 m s^{-1}, so the jump threshold is sufficiently high enough to prevent accidentally removing haboob boundary points which are moving at a realistic speed. A final quality control is implemented as follows. For β at time t and angle ϕ_1, where ϕ_0 is the angle immediately prior to ϕ_1, if

$$\beta(t,\phi_1) - \beta(t,\phi_0) > 375\left[\sqrt{2}\beta(t,\phi_0)(1 - \cos(\phi_1 - \phi_0))\right] \tag{3.9}$$

then $\beta(t,\phi_1)$ is flagged as invalid. This final check catches haboob boundary points which have much greater radii compared to neighboring haboob boundary points. As with the jump threshold check, this catches haboob boundary points that misidentified boundary layer turbulence as the haboob boundary. The factor of 375 used in Equation 3.9 was chosen after much trial and error.

Finally, at every time, β is linearly interpolated in the angular dimension to recover lost haboob boundary points created through the quality control process. These interpolated haboob boundary points are then converted back into Cartesian coordinates. The interpolated Cartesian haboob boundary points are represented by $\boldsymbol{b}$. For a given t and ϕ, $\boldsymbol{b}$ yields a two-dimensional vector in x and y.

3.3 Results

3.3.1 Haboobs on Flat Terrain

We first investigate how the daytime haboobs in our simulations are impacted by surface roughness and dust-radiation interactions on flat terrain before considering their behavior on sloped terrain. As a reminder, all results in the main text of this paper are for the southern haboobs, since the northern haboobs give qualitatively similar results. Figure 3.3a demonstrates the mean and standard deviation propagation speeds for haboobs on flat terrain. The mean and standard deviation are taken over all angles ϕ (i.e. radially around the entire haboob), since haboobs on featureless terrain without background winds should expand equally in all directions at about the same rate. Increasing surface roughness from 0.001 m to 0.034 m slows these haboobs down by ~0.75 m s^{-1} (~10%), but subsequent increases in surface roughness produce smaller decreases in propagation speeds (Figure 3.3a). Density current propagation speeds are directly tied to temperature perturbations (Benjamin 1968), so haboobs which dissipate more rapidly through warming should propagate more slowly than those which dissipate less rapidly. Increased surface roughness enhances the sensible heat fluxes within the haboobs which in turn increases the in-haboob warming (Figure 3.3b). So, higher surface roughnesses causes haboobs to dissipate faster – and thus propagate slower – than lower surface roughnesses (Figure 3.3d). Additionally, increased surface roughness leads to greater surface drag on the haboobs which also reduces propagation speeds (Figure 3.3c). Several previous studies have similarly shown increased surface roughness/sensible heat flux leading to faster dissipation of haboobs/cold pools on flat terrain (Gentine et al. 2016; Grant and van den Heever 2016, 2018; Huang et al. 2018; Bukowski and van den Heever 2022).

Dust-radiative interactions have a negligible effect on the propagation speeds of the flat terrain haboobs simulated here (Figure 3.3a), contrary to the findings of BvdH21. As BvdH21 simulated haboobs that lived through both daylight and nighttime hours, and as our simulations here are representative of haboobs from short-lived convection, it seems reasonable to speculate that dust-radiative interactions become more important as haboobs are longer lived and traverse the diurnal cycle. It appears that it requires several hours for the effect of dust on radiative heating rates to become cumulatively large enough to impact haboob propagation speeds in a meaningful manner.

We now investigate the dust lofted by the passage of haboobs in the flat terrain simulations. Total dust mass initially increases rapidly with time and then asymptotes between 30-90 min for haboobs on flat terrain (Figure 3.4a). This behavior suggests that dust lofting mostly ceases once haboobs have dissipated after ~30 min, and that the dry deposition of dust is minimal. H18 also argued that the deposition of dust should be minimal in haboob simulations lasting <6 h, as vertical wind speeds in turbulent daytime haboobs are greater than dust particle fall speeds, thereby preventing dust particles from settling to the surface. Recall in these simulations that dust emission from the surface only varies due to changes in low-level wind speed and is not a function of surface type, erodible surface fraction, soil moisture, etc. Wind speeds at 25 m AGL are minimally impacted by dust-radiative interactions and decrease with increasing surface roughness (Figure 3.4b). It follows that dust-radiative interactions have a minimal impact on the total lofted dust mass, while increased roughness decreases the total mass of dust lofted (Figure 3.4a). The total dust mass is approximately halved between ROUGH-001 and ROUGH-100 in the SLOPE-0_DUSTRAD-OFF simulations (Figure 3.4a). Taken together, Figures 3.3 and 3.4 show that increased surface roughness alone can decrease haboob dust lofting via faster haboob dissipation and increased surface drag. Note that if the erodible surface fraction was allowed to vary due to surface roughness, then the impact of roughness would likely be even more pronounced.

BvdH22 and H18 conducted somewhat similar tests regarding dust lofting, surface roughness, and sensible heat flux. In a few tests where they neglected the erodible surface fraction BvdH22 argued, as we do here, that colder and slower-dissipating haboobs should loft more dust because of the faster near-surface winds produced in association with stronger cold pools. However, our result – that on flat terrain increased surface roughness decreases haboob dust lofting – is somewhat at odds with H18. They found that as the sensible heat flux is increased, downward mixing of momentum towards the surface is increased, leading to stronger low-level wind speeds and greater dust lofting rates. There are several possible explanations for the discrepancy between H18's results and our results. First, we vary surface roughness length while H18 varied sensible heat flux. Hence, H18 did not consider the effects of increased drag on haboob dust lofting. Second, H18 used constant, prescribed sensible heat fluxes while sensible heat fluxes in this study are determined using a bulk formula. Grant and van den Heever (2016, 2018) demonstrated that prescribed and interactive sensible heat flux formulations have significantly different effects on cold pool properties and processes. Third, we simulate the entire lifetime of haboobs while H18 did not. H18 speculated that, if they ran their simulations longer, increased sensible heat flux may lead to decreased haboob lifetimes and thus decreased dust lofting. Finally, our simulations are all three-dimensional while all but one of H18's simulations were two-dimensional, so differences between turbulence in 3D and 2D could be playing a role as well. We now proceed to investigate the effects of topographic slope on haboobs.

3.3.2 Haboobs on Sloped Terrain

In this section we first investigate the effect of sloped terrain on daytime haboobs in the DUSTRAD-OFF simulations, i.e., those simulations in which radiation is not allowed to interact with the dust. As shown in prior studies, and discussed above, haboobs are expected to propagate at different speeds when traveling upslope compared to downslope. Hence, upslope and downslope propagation speeds are computed separately for all of the haboobs in this analysis. Figure 3.5a shows mean and standard deviation propagation speeds $v(\phi)$, where the mean and standard deviation are taken for angles between 180° and 0° i.e., the downslope sides of haboobs (Figure 3.1c). Figure 3.5c analogously shows mean and standard deviation propagation speeds for the upslope sides of haboobs (i.e. for angles between 0° and 180°). The results show that as the topographic slope increases, downslope haboob propagation speeds decrease while upslope haboob propagation speeds are mostly unchanged (Figure 3.5a,c). This is contrary to previous literature which has found that cold pools and laboratory tank density currents propagate faster downslope and slower upslope (Dai et al. 2012; Marleau et al. 2014; Luchetti et al. 2020a,b). The difference in our simulation results is due to the presence of an anabatic wind.

An upslope anabatic wind forms during the spin-up phase of our simulations. The development of anabatic winds in response to the daytime heating of topographic slopes is frequently observed and in keeping with mountain valley circulation theories (e.g. Defant 1951). Figure 3.6a demonstrates the speed of the anabatic wind by showing the mean low-level meridional wind at the time the initial cold bubbles are added. Recall that the radiation parameterization does not consider the topographic slope, so the downwelling shortwave radiation at the surface is similar across the domains of all simulations during the spin-up phase. Thus, while the anabatic winds form because of the heating of the sloped surfaces, they are not due to slope-induced differential heating, but rather form because the heating creates a pressure gradient between the sloped surface and the ambient environment (not shown).

The anabatic wind speed increases as topographic slope is increased (Figure 3.6a). For steeper topographic slopes, air is warmed over a deeper layer (i.e. the height of the topography) thereby driving a larger pressure gradient force between the sloped surface and the ambient environment compared to less steep slopes (not shown). Greater roughness lengths drive larger sensible heat fluxes, thereby increasing the heating rates of near-surface air, and subsequently causing larger pressure gradient forces compared to lower roughness lengths (not shown). Greater roughness lengths also increase the drag on the anabatic wind. The experiments show that the anabatic wind speed weakly increases as the surface roughness is increased (Figure 3.6a), indicating that the effect of increased sensible heat fluxes outweighs the effect of increased drag. There may also be a self-exciting component to the anabatic wind speeds detailed as follows. As increased slope or roughness causes the anabatic wind speed to increase, these greater wind speeds will drive higher sensible heat flux, which drives more heating, which drives an even faster anabatic wind speed.

Figure 3.5b (3.5d) shows the downslope (upslope) haboob propagation speeds relative to the anabatic wind speeds, i.e., the anabatic wind speeds have been added (subtracted) from the propagation speeds shown in Figure 3.5a (3.5c). When adjusting for advection due to the anabatic winds it is evident that as the topographic slopes become steeper, downslope haboob propagation speeds are mostly unchanged while upslope haboob propagation speeds decrease. The anabatic wind speed at 25 m AGL and 0 min is used when making this adjustment, but the results shown in Figure 3.5b,d are not overly sensitive to the time or depth chosen. After taking into account the anabatic wind velocities, the behavior of the haboob propagation speeds are more in keeping with findings of past research (Dai et al. 2012; Marleau et al. 2014; Luchetti et al. 2020a,b). While previous studies have disagreed about the influence of ambient winds on cold pool propagation speeds (Luchetti et al. 2020a,b), here the ambient anabatic wind plays an important role in altering the propagation speeds.

Even after accounting for the anabatic wind speeds, downslope haboob propagation speeds do not seem to meaningfully increase on steeper slopes (Figure 3.5b). To ensure that this relationship is not a result of shortfalls in our simulation setup or analysis, several simplified slope simulations were conducted with no spin-up, the parameterized radiation turned entirely off, and a free-slip surface (not shown). We find that no anabatic wind forms due to the lack of sensible heat fluxes in these simplified simulations. Accordingly, haboobs are observed to propagate progressively faster downslope and slower upslope with increasing slope than they do on flat terrain in these simplified simulations. Our model setup and analysis produce results that are therefore in keeping with traditional theory. The simplified simulations also show that a mechanism beyond the anabatic wind is slowing the downslope propagation of haboobs in our suite of sensitivity simulations. As the topographic slope increases, sensible heat flux in both the upslope and downslope regions of haboobs increases, likely because of the anabatic winds driving faster low-level wind speeds (Figure 3.6b). Hence, as the haboobs are warmed, the magnitude of the haboob temperature perturbations decreases, and the haboobs slow down (Figure 3.6d). This more rapid dissipation of haboobs on increasingly sloped terrain explains why there is not a clear increase in downslope propagation speeds when adjusting for the anabatic wind speed (Figure 3.5b).

Topographic slope also has a marked impact on dust emissions. After 30 min, the mass of dust lofted inside the haboobs and the total mass of lofted dust are nearly identical for SLOPE-0 simulations (Figure 3.7a), which is expected because the SLOPE-0 simulations do not produce anabatic winds nor dust lofting far from the haboobs. We add a 1 km buffer around haboobs when determining the in-haboob dust mass (see Figure 3.1e-f for an example). Without this 1 km buffer, the in-haboob dust mass is noticeably less than the total dust mass for flat ground simulations (not shown). This suggests that some dust is located slightly ahead of the haboob boundary, perhaps because the –0.5 K threshold used to detect haboob boundary points is slightly too restrictive and/or because some of the winds associated with haboobs are ahead of their temperature deficits. Previous studies have shown that winds associated with cold pools can occur ahead of drops in temperature (Byers and Braham 1949; Drager and van den Heever 2017; van den Heever et al. 2021; Wills et al. 2023). Regardless, as topographic slope increases, the total dust mass is increasingly greater than the in-haboob dust mass (Figure 3.7a). The only other possible source of this dust lofting found outside of the haboobs in this experiment setup is the anabatic wind. Note that previous studies have also shown that upslope and downslope winds can contribute to dust emissions (Pokharel et al. 2017; Dhital et al. 2022).

After 90 min, the increase in dust lofting due to increasingly sloped terrain is more pronounced than at 30 min. As haboobs have almost entirely dissipated by 90 min, we only examine the total dust mass at this time. There is approximately 1.5 to 4.5 times more dust mass in the SLOPE-5 simulations than the SLOPE-0 simulations depending on the surface roughness (Figure 3.7b). Figure 3.4 indicated that on flat ground most haboob dust lofting occurs during the first 30 minutes of their lifetimes. Hence, most of the difference in total dust mass between 90 min (Figure 3.7b) and 30 min (Figure 3.7a) is due to the anabatic wind. For the SLOPE-5 simulations, the effect of the anabatic wind is so pronounced that the total dust mass increases as the surface roughness increases (Figure 3.7b). Hence, as surface roughness is increased on the most extreme topographic slope, enhanced dust lofting from the larger anabatic wind speed more than counteracts decreases in dust lofting from faster haboob dissipation and larger drag. Recall that as surface roughness increases, the anabatic wind speed increases due to greater sensible heat fluxes even though drag on the anabatic wind is also greater (Figure 3.6a).

The impact of dust-radiative interactions on haboob propagation speeds and dust mass remains small when considering increasingly sloped terrain (not shown). We reiterate our speculation that dust-radiative interactions would become more impactful for longer-lived haboobs. The overall results of the suite of sensitivity experiments are summarized in Figures 3.8 and 3.9.

3.4 Conclusions

Haboobs are a major contributor to dust emissions in many regions (Heinold et al. 2013; Marsham et al. 2013; Bergametti et al. 2017). Many factors are known to influence haboob propagation speeds and dust lofting, such as turbulent mixing, low-level static stability, or surface vegetation types (H18, BvdH21, BvdH22). Haboobs commonly occur in regions of steeply sloped topography (Adams and Comrie 1997; Knippertz et al. 2007; Miller et al. 2008), but the impact of topographic slope on haboobs – and cold pools in general – has not been disentangled from these other known factors. Hence, the objective of this study has been to investigate the impacts of topographic slope on daytime haboob propagation and dust lofting, along with how these impacts are modulated by surface roughness and dust-radiation interactions. Surface roughness was tested as BvdH22 found it difficult to disentangle the effects of surface roughness on haboob propagation and dust lofting from the effects of vegetation type.

Dust-radiation interactions were tested as BvdH21 also demonstrated they influence haboob propagation and dust lofting.

A suite of 40 dry, high-resolution idealized simulations was conducted using the Regional Atmospheric Modeling System (RAMS). These simulations test all combinations of five topographic slopes (0%, 1%, 2%, 3%, 5%, based on analysis of topography in the southwestern United States), four surface roughness lengths (0.001 m, 0.034 m, 0.066 m, 0.100 m, based on vegetation tested by BvdH22), and two dust-radiation settings (radiatively inactive and radiatively active dust). Haboobs were initiated by adding cold bubbles to simulations after an initial 90-minute period of boundary layer spin-up was performed. To distinguish the haboobs from their surroundings and calculate haboob propagation speeds, the leading edges of the haboobs were identified and tracked in time (Figure 3.1b,c).

- On flat ground, increasing surface roughness decreases haboob propagation speeds and reduces the total mass of dust lofted by haboobs (Figures 3.3, 3.4, and 3.9e-f).
- As the topographic slope becomes steeper, the ground-relative downslope propagation speed of haboobs decreases, while the upslope propagation speed is mostly unchanged (Figures 3.5a,c, 3.9). These changes – or lack thereof – are driven primarily by the development of an anabatic wind and the changes in its speed which arise due to the sloped topography and heating from solar radiation (Figure 3.6a). Relative to the anabatic wind speed, the downslope propagation speed of haboobs is mostly unchanged and the upslope propagation speed decreases with increasing topographic slope (Figure 3.5b,d).
- As the topographic slope becomes steeper, dust lofting by anabatic winds causes the total mass of dust lofted into the atmosphere to increase (Figures 3.7, 3.9).

- Aerosol-radiative impacts on haboob propagation and dust lofting are small compared to the impacts of surface roughness and topographic slope. This result stands in contrast to BvdH21 and is mostly likely because BvdH21 focused on long-lived haboobs while this study focused on haboobs with lifespans of ~30 min.

The results of this study suggest that the velocity of the anabatic winds that develop due to the heating of sloped terrain is of primary importance to the propagation and dust lofting of haboobs on such terrain. Over complex topography the misrepresentation of anabatic winds and their interactions with haboobs may be a source of error in forecast models due to the difficulties in accurately representing such topography in forecast models, primarily around grid resolution. Similarly, climate model parameterization of cold pools (e.g. Rooney et al. 2022) should include such interactions to potentially reduce errors in the amount of dust lofted by haboobs. We hope that the results of this study can be used to improve the representation of interactions between haboobs and anabatic winds in both small- and large-scale models.

The findings of this study lead us to pose several new questions about haboob processes. What is the impact of topographic slope on haboobs at night? This study focused only on daytime conditions. Results at night may differ given that katabatic winds flow downslope at night, and that nocturnal stratification is known to affect haboobs (BvdH21). Also, what is the impact of complex terrain on haboobs? This study used linearly sloped terrain to ease the interpretation of results, but results may vary with more complex terrain. Finally, what are the feedbacks between haboobs, topography, and storms? This study used dry conditions to facilitate the analysis, but the subsequent feedbacks to the parent storm producing the haboob are another avenue worth investigating. As this study found a counterintuitive result – that haboobs propagate slower downslope than they propagate upslope – investigating these questions may lead to further interesting physical insights on the relationships among haboobs, topography, land-atmosphere interactions, and convective storm processes.

3.5 Tables and Figures

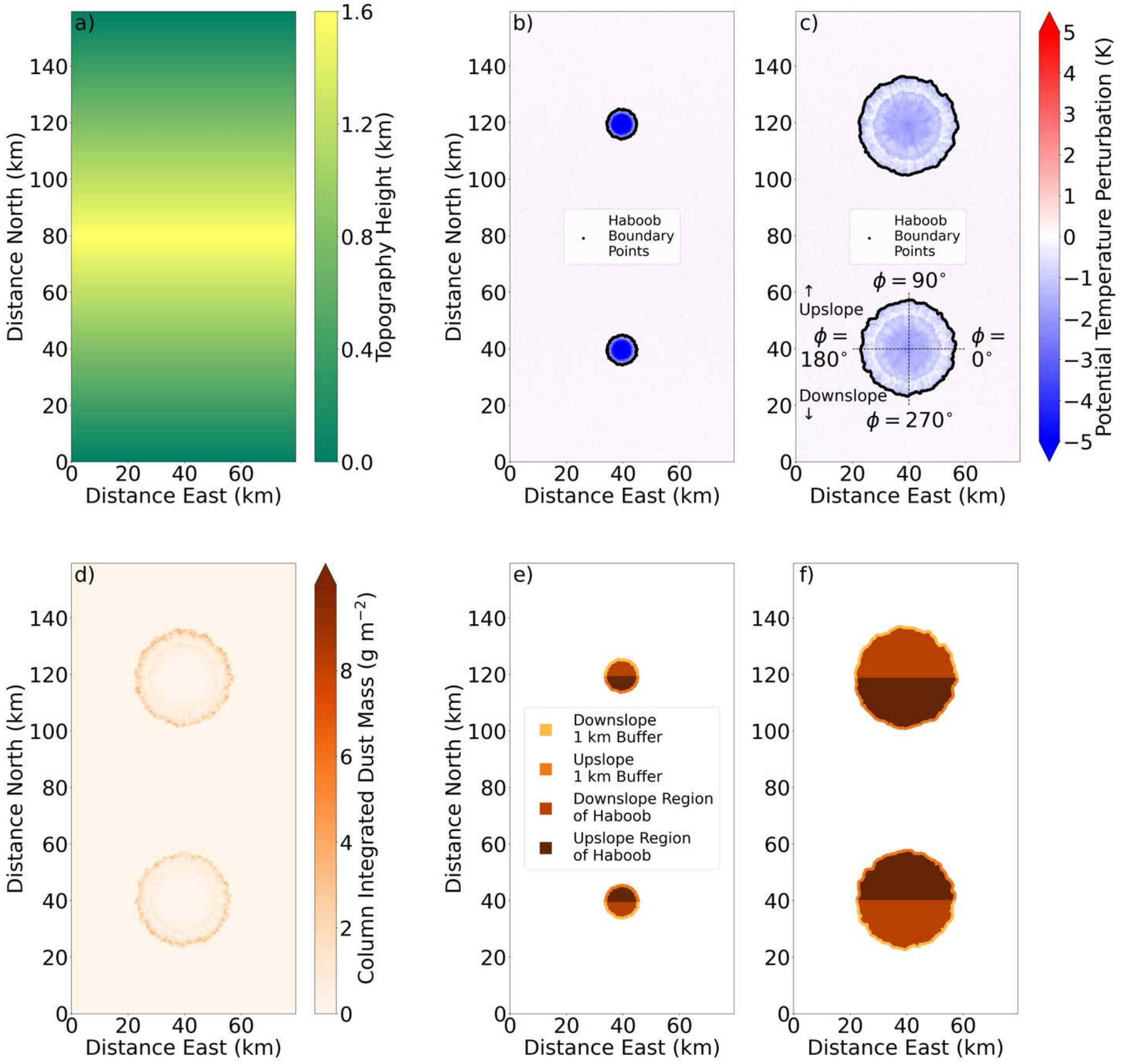

Figure 3.1. **Model domain, topography setup, and output**. All data in this figure are plotted for the SLOPE-2_ROUGH-034_DUSTRAD-ON simulation. Shown are (a) model topography (m); (b) 25 m AGL potential temperature perturbation (K) and haboob boundary points at 1 min; (c) as in (b) but at 30 min; (d) column integrated dust mass (g m^{-2}) at 30 min; (e) identified haboob regions at 1 min; and (f) as in (e) but at 30 min. Also indicated in (c) are the angles (ϕ) used in the haboob tracking algorithm.

Table 3.1. **Summary of RAMS settings common to all simulations.**

Model Setting	**Value/type**
Starting time	1984-08-09 2030 Z (1330 LT)
nx, ny, nz	800, 1600, 200
dx, dy, dz	100, 100, 50 m
dt	0.5 s
Central latitude and longitude	32.3 N, 111.0 W
Data output frequency	1 min
Lateral boundary condition	Cyclic
Radiation Parameterization	Harrington (1997)
Surface parameterization	LEAF-3 (Walko et al. 2000)
Vegetation Type	Desert, bare soil
Soil Type	Silty clay loam
Number of soil layers	11
Soil depth	0.5 m
Initial soil surface temperature offset from lowest atmospheric level	-2 K
Soil moisture	None

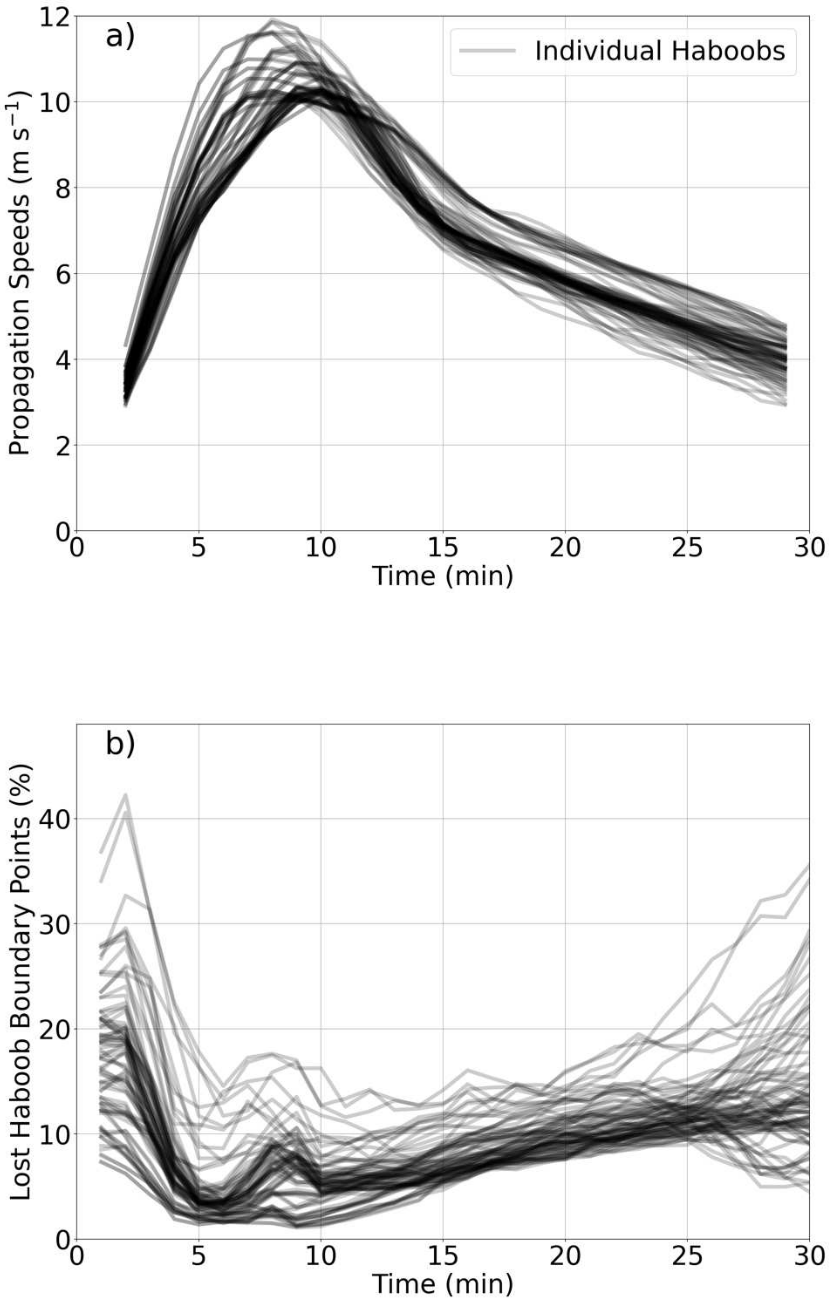

Figure 3.2: **Haboobs begin to decelerate after ~10 minutes and become difficult to track ~30 minutes**. (a) Timeseries of propagation speeds for all the haboobs captured in the idealized simulations. (b) Percentage of lost haboob boundary points for all the haboobs as a function of time.

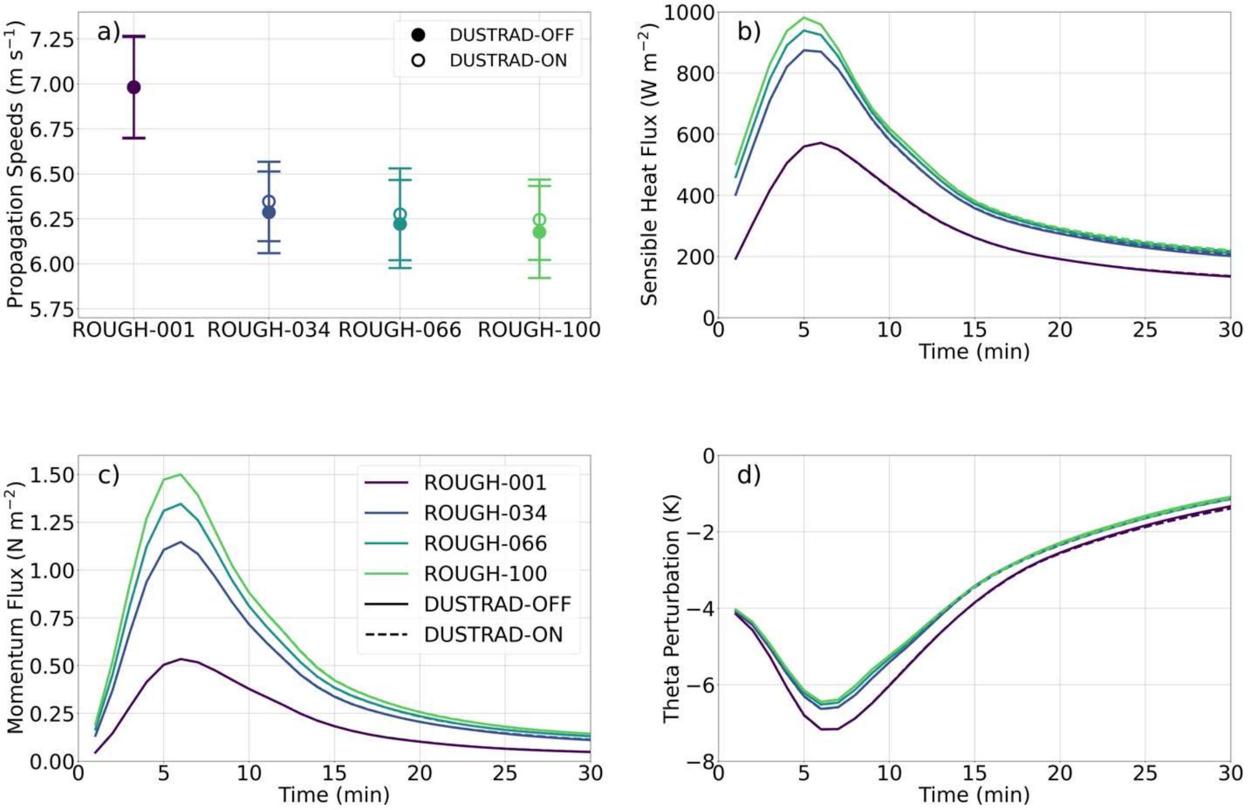

Figure 3.3: **Haboobs on flat terrain are slowed by increasing surface roughness and are mostly unaffected by dust-radiative interactions**. All data in this figure are from SLOPE-0 simulations. (a) Haboob propagation speeds as a function of surface roughness for DUSTRAD-OFF simulations (filled circles) and DUSTRAD-ON simulations (hollow circles). In (a) circles (error bars) represent mean (standard deviation) propagation speeds over all haboob boundary points. (b) Timeseries of in-haboob mean surface sensible heat flux for different surface roughnesses (line colors) and dust-radiation settings (line styles). (c) as in (b) but for the horizontal momentum flux. (d) as in (b) but for the 25 m AGL potential temperature perturbation.

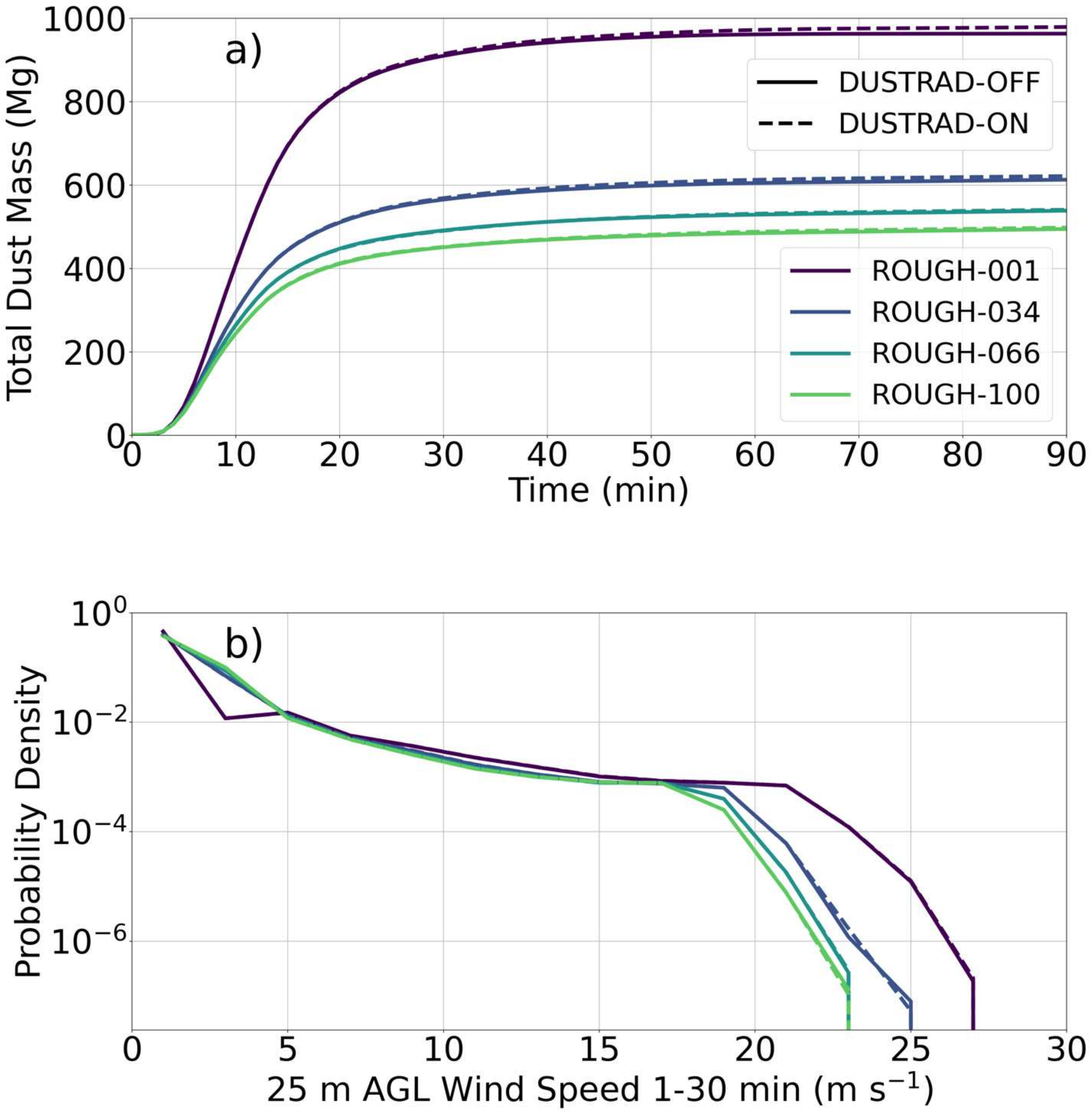

Figure 3.4: **For haboobs on flat terrain, increased surface roughness decreases the total dust mass while dust-radiative interactions weakly increase total dust mass**. (a) Timeseries of total dust mass for SLOPE-0 simulations, surface roughness is indicated by line color and the dust-radiative interaction setting is indicated by line style. (b) Probability density function of 25 m AGL wind speed in SLOPE-0 simulations.

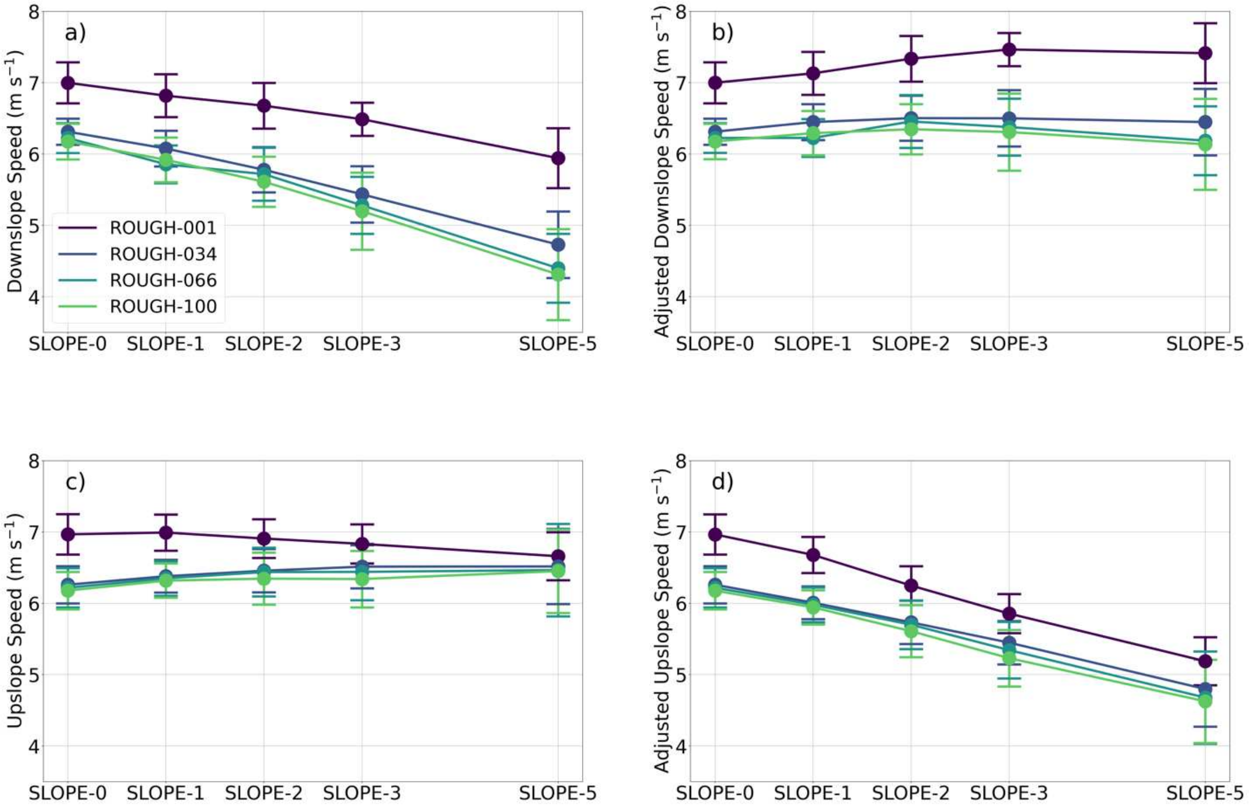

Figure 3.5: **As the topographic slope increases, anabatic winds cause downslope haboob propagation speeds to decrease and upslope speeds to be mostly unchanged**. All data in this figure are from DUSTRAD-OFF simulations. (a) Downslope haboob propagation speeds as a function of topographic slope for different surface roughnesses (line colors). In (a) circles (error bars) represent mean (standard deviation) propagation speeds. (b) as in (a) but with propagation speeds adjusted for anabatic wind speed. (c, d) as in (a, b) but for upslope propagation speeds.

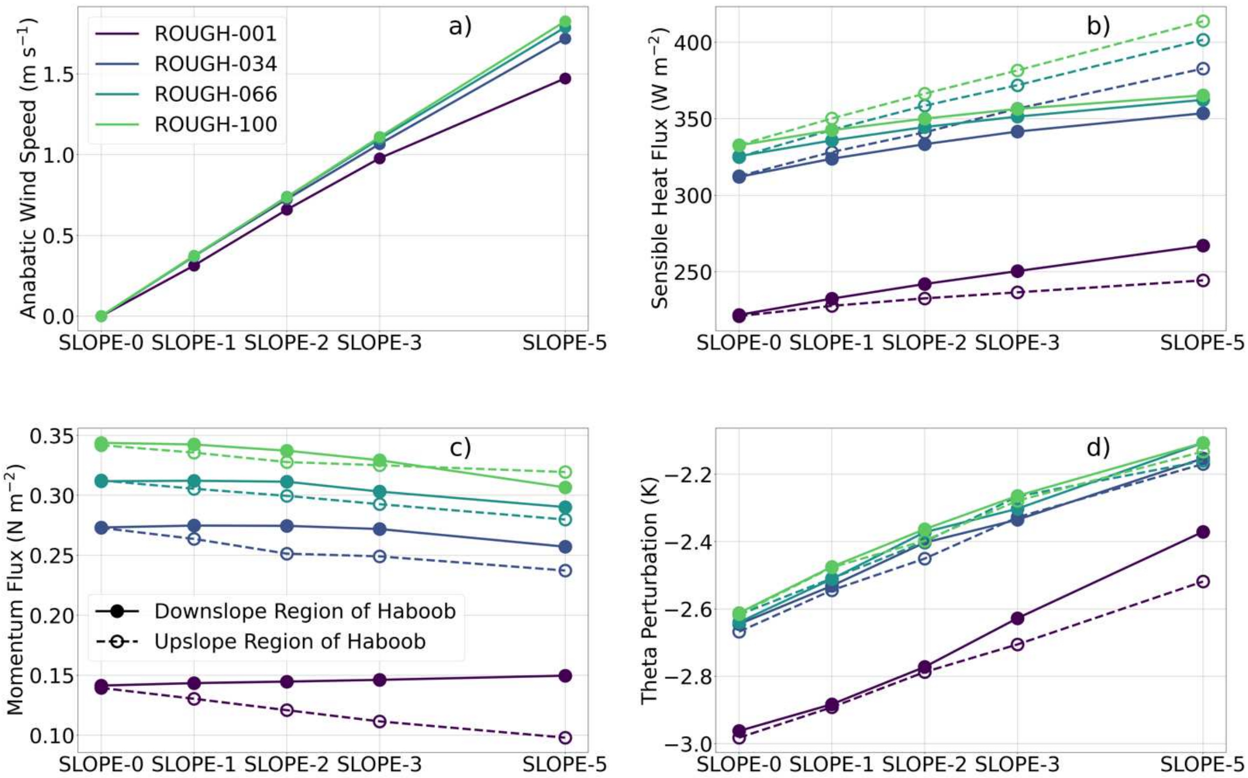

Figure 3.6: **Increasing topographic slope and surface roughness lead to increased anabatic wind speeds, in haboob surface sensible heat fluxes, and haboob dissipation**. All data in this figure are from DUSTRAD-OFF simulations. (a) Mean 25 m AGL meridional wind speed at the time cold bubbles are initiated as a function of topographic slope for different surface roughnesses (line colors). (b) Mean sensible heat flux between 10 min and 30 min for the downslope (solid circles and lines) and upslope (hollow circles and dashed lines) regions of haboobs as a function of slope for different roughnesses (line colors). (c) as in (b) but for horizontal momentum flux. (d) as in (b) but for 25 m AGL potential temperature perturbation.

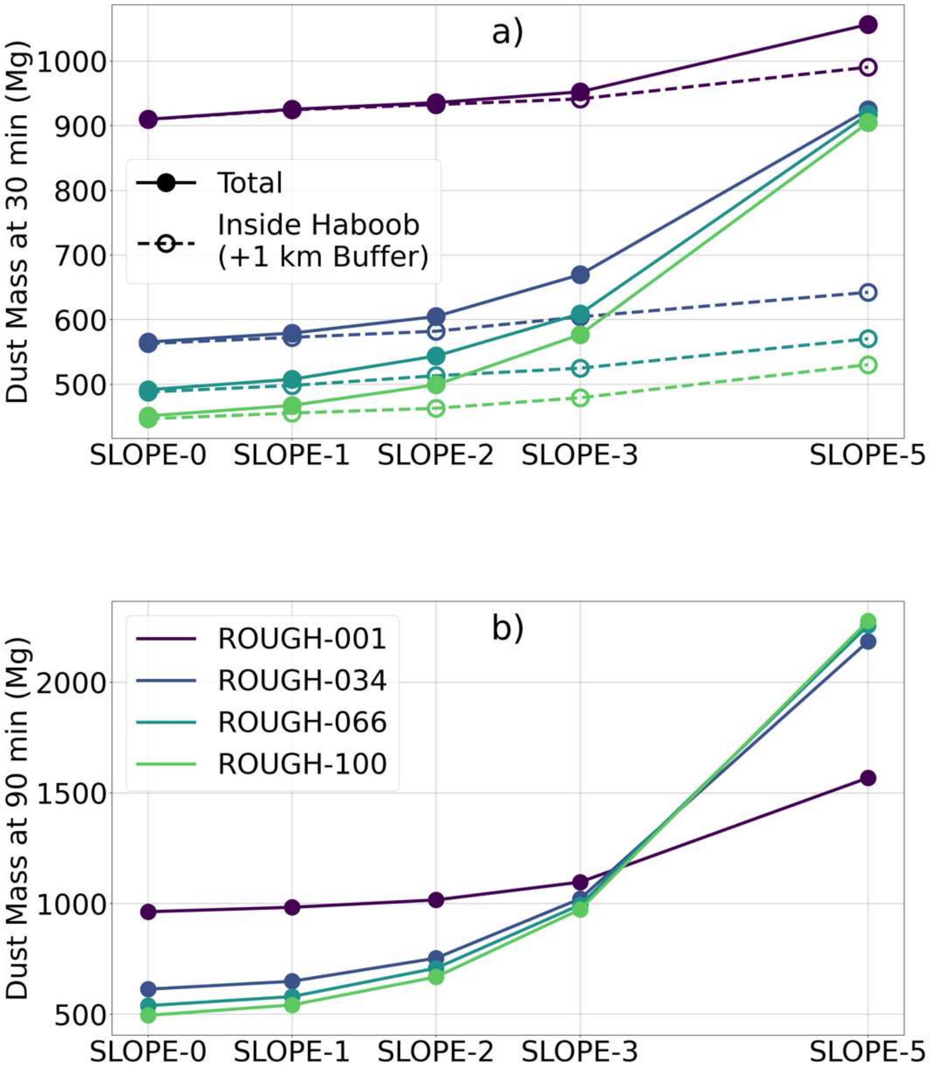

Figure 3.7: **Increasing topographic slope increases the amount of lofted dust, mostly due to the increased anabatic wind speeds**. All data in this figure are from DUSTRAD-OFF simulations. (a) Total dust mass (solid circles and lines) and dust mass inside haboobs with a 1 km buffer (hollow circles and dashed lines, see main text for explanation of the 1 km buffer) as a function of topographic slope for different surface roughnesses (line colors) at 30 min. (b) as in (a) but only for total dust mass at 90 min. Note the vertical scale differs between (a) and (b).

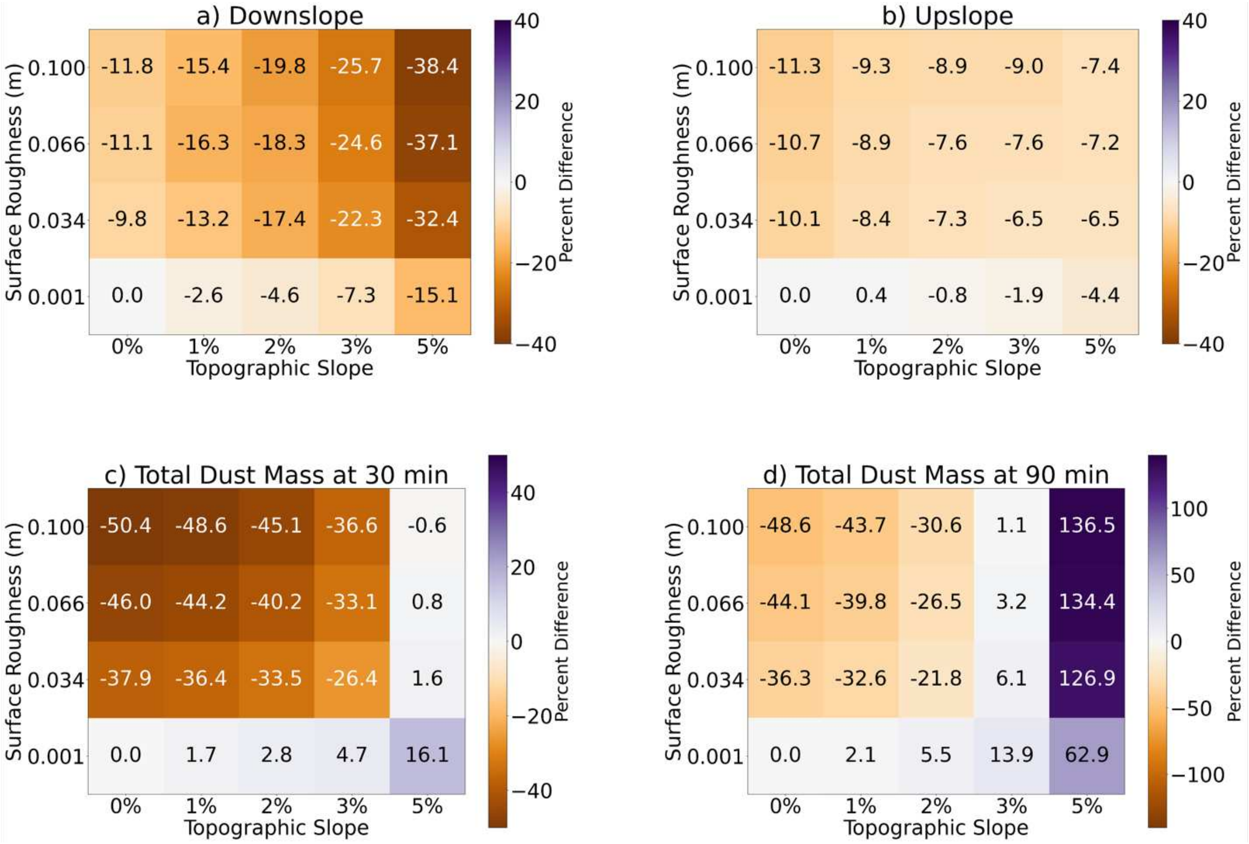

Figure 3.8: **Summary of changes in propagation speeds and lofted dust mass with surface roughness and topographic slope**. All data in this figure are from DUSTRAD-OFF simulations. (a) Percent difference in mean downslope propagation speed from the SLOPE-0_ROUGH-001_DUSTRAD-OFF simulation. (b) as in (a) but for upslope propagation speed. (c) Percent difference in total dust mass at 30 min. (d) as in (c) but at 90 min.

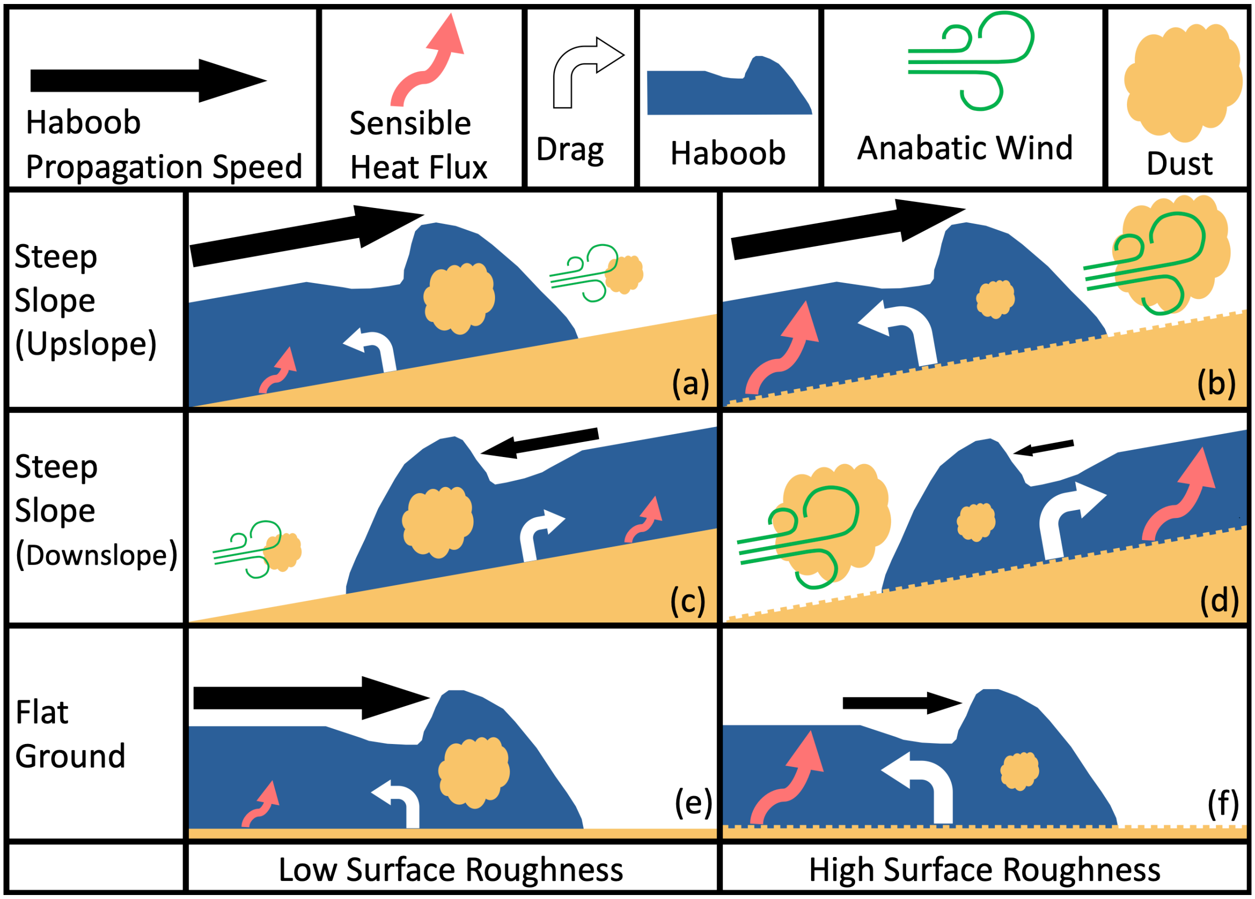

Figure 3.9: **Schematic summary demonstrating the impacts of topographic slope, surface roughness, and dust-radiative interactions on haboobs**. Larger objects are indicative of greater values, but the change in the size of objects between panels is not directly to scale. Dust clouds inside of haboobs are indicative of dust lofted by haboobs, while dust clouds outside of haboobs are indicative of dust lofted by anabatic winds.

Chapter 4: Cold Pools Disaggregate Convection over Heterogeneous Surfaces

4.1 Introduction

Anthropogenic deforestation in rainforests such as the Amazon creates a heterogeneous land surface. Such heterogeneities can drive mesoscale circulations and impact the distribution of convective clouds and rainfall (Souza et al. 2000; Durieux et al. 2003; Chagnon et al. 2004; Wang et al. 2009). When land surfaces with different properties are adjacent on the mesoscale, studies have shown that moist convection is often favored over warmer and drier surfaces compared to nearby cooler and moister surfaces (Rabin et al. 1990; Mascart et al. 1991; Chagnon et al. 2004; Taylor et al. 2012). However, environmental factors such as low-level humidity or wind direction can sometimes cause this relationship to reverse (Findell and Eltahir 2003a,b). Enhanced convective activity over warm/dry surfaces has been attributed to mesoscale solenoidal circulations driven by surface heterogeneity (hereafter simply solenoidal circulations). These circulations flow at low-levels from cool/moist regions into warm/dry regions, ascend in warm/dry regions, and then return towards cool/moist regions at higher levels. Ascent from solenoidal circulations can initiate convection in warm/dry regions. (Mascart et al. 1991; Chen and Avissar 1994; Hong et al. 1995; Cheng and Cotton 2004; Cioni and Hohenegger 2018; Branch and Wulfmeyer 2019). Garcia-Carreras et al. (2011) investigated the mechanisms by which vegetation-induced solenoidal circulations in a tropical continental environment influence cloud formation in detail. They demonstrate that solenoidal circulations can initiate convection at their edges by both lifting air and also creating a favorable thermodynamic environment. Collisions between solenoidal circulations can also initiate convection (Lynn et al. 1998; Rieck et al. 2014).

Similar to heterogeneous land surfaces, convective cold pools create regions that are favorable for the initiation of new convective storms and regions where convection initiation is suppressed. Studies as early as Byers and Braham (1949) have noted that moist convection can be inhibited in the interiors of cold pools. On the other hand, cold pools initiate new storms at their edges through the same mechanisms that solenoidal circulations do: mechanical lifting, creating favorable thermodynamics, and collisions (Purdom 1976; Weaver and Nelson 1982; Tompkins 2001; Torri et al. 2015; Feng et al. 2015; Drager et al. 2020; Falk and van den Heever 2023). These similarities suggest that convection initiation may be affected by the interaction between cold pools and solenoidal circulations.

Cold pools and solenoidal circulations can interact in important ways. If cold pools form on the cool/moist side of a solenoidal circulation, the circulation can be accelerated by the cold pools increasing the temperature gradient between the warm/dry and cool/moist regions (Rieck et al. 2015; Ascher et al. 2024). Similar results have been found for mountains-plains circulations (Bao and Zhang 2013). Cold pools can conversely act to reverse the flow of solenoidal circulations if they form in the warm/dry region (Harvey et al. 2022; Ascher et al. 2024). Chen et al. (2020) and Ascher et al. (2024) both found that convection which initially forms due to land surface heterogeneities can produce cold pools that subsequently initiate new convection in areas where convection was previously absent. Despite this previous research, the impacts of surface heterogeneity and cold pools on convection initiation have not been systematically disentangled from each other. Studies which aim to understand the impacts of cold pools often conduct mechanism-denial experiments to eliminate cold pools through changes to the evaporation (e.g. Crook and Moncrieff 1988; Khairoutdinov and Randall 2006; Jeevanjee and Romps 2013; Grant et al. 2018, 2020), but such mechanism-denial experiments are usually conducted over homogeneous land surfaces. Additionally, studies investigating the effects of land surface heterogeneity often test striped or checkerboard-like surfaces instead of surfaces with more realistic variability (Rieck et al. 2015; Harvey et al. 2022; Ascher et al. 2024). Hence, the interactions between cold pools and solenoidal circulations driven by land surfaces with realistic heterogeneity are also unclear.

The objective of this study is to address the following science question: What are the individual and synergistic impacts of surface heterogeneity/solenoidal circulations and cold pools on the initiation of convective storms? We run a set of large eddy simulations (LES) designed to directly address this question. Realistic and weakened cold pools are tested along with realistic and homogenized vegetation. Storms are tracked to identify where they initiate. The factor separation technique (Stein and Alpert 1993) is used to disentangle the individual and synergistic impacts of both cold pools and surface heterogeneity on convection initiation. Our findings demonstrate the importance of cold pools in modulating the effects of deforestation on storms in the Amazon. Cold pools may similarly modulate the effect of heterogeneous surfaces in other environments.

4.2 Methods

4.2.1 Large Eddy Simulations

Large eddy simulations are conducted using the Regional Atmospheric Modeling System (RAMS) version 6.3.04 (Pielke et al. 1992; Cotton et al. 2003; Saleeby and van den Heever 2013; van den Heever et al. 2023). Simulations are idealized to isolate processes of interest, except that realistic vegetation data are used to accurately capture the heterogeneity patterns created by deforestation. A horizontal grid spacing of 150 m is used with a timestep of 0.75 s, while the vertical grid spacing starts at 50 m near the surface and is stretched to 300 m. Grid spacings of this order are needed to accurately represent cold pools and their interactions with the land surface (Straka et al. 1993; Grant and van den Heever 2016; Hirt et al. 2020; Fiévet et al. 2023). The model domain is 150 x 150 x 24.2 km. Periodic lateral boundaries are used. The Land-Ecosystem-Atmosphere-Feedback version 3 (LEAF-3) (Walko et al. 2000) model simulates two-way land-atmosphere interactions. Radiative tendencies are updated every 5 min using RTE-RRTMGP (Pincus et al. 2019). Cloud microphysics are represented using the RAMS double-moment bin emulating microphysics scheme (Saleeby and van den Heever 2013). Subgrid turbulence is parameterized following Smagorinsky (1963) with modifications from Lilly (1962) and Hill (1974).

The atmosphere is initialized using the 23 February 1999 TRMM-LBA sounding presented in Grabowski et al. (2006) (Figure 4.5). This sounding is chosen because it has been commonly used in studies of Amazon convection and in mechanism-denial studies of cold pools (e.g. Grabowski et al. 2006; Khairoutdinov and Randall 2006; Kurowski et al. 2018). Simulations start on 23 February 1999 at 0730 LT (UTC = LT + 4). They are integrated for 120 h (5 days) to capture multiple diurnal cycles and to ensure that a large number of storms are simulated, thus generating a statistically robust sample of convection initiation events. The grid spacing, domain size, and integration duration were chosen as a compromise given the available computation resources. Sandy loam soil, an initial soil temperature of 24.8 °C, and an initial soil moisture 0.24 m^3 m^{-3} are chosen based on contemporaneous observations shown in Alvalá et al. (2002). The soil extends 2 m below the surface and is broken into 26 levels. Note that all atmospheric and land surface fields are initially horizontally homogeneous in all simulations, other than the vegetation in certain simulations (as described below). Initial random potential temperature perturbations of amplitude 0.1 K in the lowest 500 m are used to facilitate development of the boundary layer.

Four simulations are conducted to assess the individual and synergistic impacts of land surface heterogeneity and cold pools on convection initiation. In the control simulation (CTRL), realistic vegetation and realistic evaporation are used, thereby representing realistic land surface and cold pool processes. The model domain is centered at 10.70 S, 62.05 W and contains the site where the initial sounding was launched from (Figure 4.1a, where "evergreen broadleaf tree" is rainforest). In the homogeneous simulation (HMGN), vegetation properties at each grid point are set to the vegetation-area-weighted mean values of properties in CTRL. Thus, CTRL and HMGN have the same domain-mean vegetation properties, but CTRL has vegetative heterogeneity while HMGN does not. This homogenization only applies to properties which are fixed in time, so prognostic quantities (e.g. soil and canopy moisture/temperature, surface fluxes) are allowed to evolve freely in all simulations. Thus, surface heterogeneities in quantities like soil moisture can develop over time in HMGN. In the third evaporation-off simulation (EOFF), evaporation of rain and drizzle are disabled in the lowest 2 km. Grant et al. (2018) describe how this approach is implemented in RAMS. Since RAMS considers the evaporation of all hydrometeors together, evaporation is only disabled when no cloud water is present at a grid point. This means that only the evaporation of falling rain and drizzle are altered and that other cloud microphysical processes, such as the evaporation of cloud water due to entrainment, remain unaltered. Analysis of density potential temperature at the lowest model level above ground shows that cold pools are almost entirely eliminated in EOFF (Figure 4.6). Finally, the homogeneous and evaporation off simulation (HMGN_EOFF) simultaneously applies the homogeneous vegetation of HMGN and the disabled evaporation of EOFF in order to assess synergistic interactions between these processes.

4.2.2 Tracking

We use a tracking algorithm to identify where storms initiate. By tracking storms in time, we can importantly distinguish the locations where storms initiate from the locations where storms subsequently propagate. We focus our analysis on the initiation locations of storms only to prevent double-counting storms. The Tracking and Object-Based Analysis of Clouds (*tobac*) algorithm v1.5 (Heikenfeld et al. 2019; Sokolowsky and Freeman et al. 2024) is used to track convective updrafts in three dimensions. A vertical velocity threshold of 3 m s^{-1} is used to identify convective updrafts, which must also occupy a volume of at least 64 contiguous grid points to be counted as an updraft. Updrafts tracked for less than 15 min are excluded from further analysis, as updrafts of such durations are likely shallow convection. Updrafts which are tracked for more than 15 min are referred to as storms (e.g. Figure 4.1b, red points and lines). The selected *tobac* thresholds were subjectively determined after trial-and-error, but results are not qualitatively sensitive to the thresholds chosen.

4.2.3 Quantifying Aggregation

We use the organization index (I_{org}) (Weger et al. 1992) to quantify the aggregation of storm initiation locations. I_{org} is calculated by comparing the nearest neighbor cumulative density function (NNCDF) of a given set of points against a NNCDF of random uniform points, then calculating the area underneath the curve. An I_{org} of approximately 0.5 indicates the analyzed points are randomly distributed, while values above (below) 0.5 indicate the analyzed points are aggregated (regularly distributed). All storm initiation locations over the five simulated days for a given simulation are used when calculating I_{org}. We therefore quantify the degree to which the locations where storms initiate are aggregated. Past studies have, by contrast, used I_{org} to quantify the organization of convection at a given snapshot in time (Seifert and Heus 2013; Cheng et al. 2018; Pscheidt et al. 2019). For each simulation, a distribution of I_{org} values is calculated by generating 1000 random uniform NNCDFs and thus recalculating I_{org} 1000 times.

4.2.4 Factor Separation

The factor separation technique (Stein and Alpert 1993) is applied to understand the individual and synergistic impacts of heterogeneous vegetation and cold pools on patterns of convection initiation. For a given quantity φ, such as mean values of I_{org}, the impact of heterogeneous vegetation can be determined by subtracting φ in EOFF by φ in HMGN_EOFF:

$$F_{VEG} = \varphi_{EOFF} - \varphi_{HMGN\_EOFF} \quad (4.1).$$

Analogously, the impact of cold pools is calculated as:

$$F_{CP} = \varphi_{HMGN} - \varphi_{HMGN\_EOFF} \quad (4.2)$$

and the impact of synergetic interactions between heterogeneous vegetation and cold pools is:

$$F_{VEG\_CP} = \varphi_{CTRL} - \varphi_{HMGN\_EOFF} - F_{VEG} - F_{CP} = \varphi_{CTRL} - (\varphi_{HMGN} + \varphi_{EOFF}) + \varphi_{HMGN\_EOFF}$$

(4.3).

4.3 Results

Vegetation heterogeneity has a clear impact on surface heat fluxes and low-level virtual potential temperature. Total surface heat flux (i.e. the sum of the sensible and latent heat fluxes) at 0930 LT, before the onset of deep convection, is greater over the forest than over the deforested region in CTRL (Figure 4.1c shading). Surface heat fluxes are greater over the forest because the surface roughness length is greater and the albedo is smaller over the forest than the deforested region (Table 4.1). Reduced albedo implies the forest absorbs more energy from solar radiation, while greater roughness length means the forest more efficiently transfers this energy to the atmosphere through turbulent processes. Accordingly, at 0930 LT, the 25 m virtual potential temperature in CTRL is greater over the forest than over the deforested region (Figure 4.1c hatching). As a consequence of the homogenized vegetation in HMGN, perturbations in surface heat fluxes and low-level virtual potential temperature are smaller in magnitude and less widespread than in CTRL (compare Figure 4.1c-d). Perturbations of pre-convective surface heat fluxes and virtual potential temperature in EOFF (HMGN_EOFF) are qualitatively similar to those for CTRL (HMGN) (not shown). Hence, our simulations with heterogeneous vegetation (CTRL and EOFF) have greater virtual potential temperatures over the forest than the deforested region, while our simulations with homogeneous vegetation (HMGN and HMGN_EOFF) have comparatively more uniform virtual potential temperature across the domain.

Storms in CTRL and EOFF initiate less frequently over the deforested region than over the forest (Figure 4.2a,c). The lack of storms in the deforested region can be explained by the reduced virtual potential temperature, and hence the air being less buoyant, compared to the forest (Figure 4.1a,c). At low levels, the forest is warmer but slightly drier than the deforested region (not shown). Thus, we find a similar result to previous studies which determined that moist convection preferentially forms over warm/dry regions compared to cool/moist regions (Rabin et al. 1990; Mascart et al. 1991; Chen and Avissar 1994; Hong et al. 1995; Chagnon et al. 2004; Cheng and Cotton 2004; Taylor et al. 2012; Cioni and Hohenegger 2018; Branch and Wulfmeyer 2019). There is evidence of vegetation-driven solenoidal circulations initiating storms in CTRL and EOFF. Figure 4.2b,d show storm initiation locations before 1200 LT in these simulations to further demonstrate the effects of solenoidal circulations and cold pools. During this time period, storms initiate most frequently near the forested-deforested boundary (Figure 4.2b,d). These patterns are consistent with solenoidal circulations beginning to propagate from the deforested region into the forest and initiating convection. As the day progresses, these solenoidal circulations propagate further into the forested region and continue to initiate convection (not shown). Therefore, while solenoidal circulations are evident in the simulations, their effects are less evident in Figure 4.2a,c because the entire diurnal cycle is shown and the effects of the solenoidal circulations are spread across the forest.

Storms in HMGN and HMGN_EOFF initiate more uniformly across the domain than storms in CTRL and EOFF (Figure 4.2a,c,e,f). This is because virtual potential temperature is more uniform across the domain with homogeneous vegetation compared to heterogeneous vegetation (Figure 4.1c,d). Therefore, convection initiation is not favored or disfavored in specific regions, nor can solenoidal circulations form in the homogeneous vegetation simulations.

Cold pools also influence where storms initiate. Recall that the only difference between EOFF and CTRL is the suppressed evaporation of precipitation in the lowest 2 km, and therefore lack of cold pools, in EOFF. Storms in EOFF initiate less frequently over the deforested region than storms in CTRL (Figure 4.2a,c). This suggests that cold pools in CTRL propagate from the forest into the deforested region and initiate storms over the deforested region, despite the less favorable conditions for convection initiation compared to the forest. Chen et al. (2020) and Ascher et al. (2024) have similarly noted cold pools initiating convection in areas which are thermodynamically disfavored due to land surface heterogeneity. On the other hand, in EOFF, very few storms initiate in the deforested region due to the lack of cold pool-induced initiation. To further support this argument, we return to Figure 4.2b. The time period shown in Figure 4.2b captures the first set of storms on each day in CTRL which initiate before strong cold pools form, thus partially removing the influence of cold pools. Early storm initiation frequency in CTRL is suppressed in the deforested region relative to later time periods (compare Figure 4.2a,b) and even approaches the magnitude of suppression in EOFF over the full diurnal cycle (compare Figure 4.2b,c), further demonstrating that cold pools are largely responsible for the initiation of storms in the deforested region of CTRL.

We now use I_{org} to quantify the impact of heterogeneous vegetation and cold pools on storm initiation locations (Figure 4.3a). Storms are close to randomly distributed with homogeneous vegetation, as the mean I_{org} for HMGN and HMGN_EOFF are both ~0.5 (Figure 4.3a). The individual effect of cold pools (F_{CP}), as demonstrated from factor separation, on the mean I_{org} is small compared to F_{VEG} and F_{VEG_CP} (Figure 4.3c), demonstrating that cold pools do not have a large impact on storm initiation locations over homogeneous vegetation (see also Figure 4.3a, Figure 4.2e,f). Heterogeneous vegetation acts to aggregate storm initiation locations, since F_{VEG} is positive for the mean I_{org} (Figure 4.3c), consistent with our previous finding that storm initiation is less frequent over the deforested regions of CTRL and EOFF than the forests. The synergistic interactions between heterogeneous vegetation and cold pools acts to disaggregate storm initiation locations, since F_{VEG_CP} is negative for I_{org} (Figure 4.3c), consistent with cold pools propagating from the forest into the deforested regions and subsequently initiating convection in the deforested region of CTRL but not in EOFF. Thus, the effects of cold pools on convection initiation patterns are only apparent when vegetation is heterogeneous.

Precipitation is impacted by changes in storm initiation driven by heterogeneous vegetation and cold pools. Figure 4.3b (4.3d) shows precipitation in CTRL (EOFF) normalized by the domain mean precipitation. Normalization is necessary because more precipitation accumulates in EOFF than in CTRL as a direct result of the disabled evaporation of precipitation below 2 km in EOFF. The deforested region of EOFF receives almost no precipitation (Figure 4.3d), while such a pattern is less evident in CTRL (Figure 4.3b). These precipitation patterns follow patterns in storm initiation (Figure 4.2). We define "precipitation gaps" as areas of the domain receiving <1 mm of precipitation. We determine the total area of precipitation gaps in each simulation and conduct factor separation analysis on this metric (Figure 4.3c). The factors for this precipitation gap metric have similar relative magnitudes as the factors for mean $I_{org,}$ demonstrating that aggregating (disaggregating) storm initiation locations causes precipitation gaps to become larger (smaller).

4.4 Summary and Conclusions

The goal of this study has been to investigate the individual and synergistic impacts of surface heterogeneity and cold pools on the initiation of tropical continental convective storms. To achieve this goal, four idealized LES of deep convection in a partially deforested region of Amazon rainforest were run with varied vegetation (realistic and homogenized) and varied evaporation (realistic and disabled over the lowest 2 km to eliminate cold pools). Storms were tracked to identify where they initiate, and the aggregation of storm initiation locations was determined using I_{org}. Factor separation was used to disentangle the individual and synergetic impacts of heterogeneous vegetation and cold pools. Figure 4.4 presents a schematic summary of our results.

We find greater surface roughness and lower albedo lead to greater surface heat fluxes and virtual potential temperatures over forested compared to deforested regions (Figure 4.1a,c). This results in more frequent convection initiation over forests than deforested regions due to favorable thermodynamics and the development of solenoidal circulations between forested and deforested regions (Figure 4.2a-d, Figure 4.4a,b). Storm initiation locations are therefore aggregated over heterogeneous vegetation (Figure 4.3a). However, similar to findings by Chen et al. (2020) and Ascher et al. (2024), cold pools can propagate away from the storms over the forest and initiate new convection over the otherwise less thermodynamically favorable deforested region (Figure 4.2a-d, Figure 4.4a). This mechanism partially counteracts the effects of heterogeneous vegetation and disaggregates storm initiation locations (Figure 4.3a,c). Without cold pools, a large gap in the precipitation field forms over the deforested region in the heterogeneous vegetation simulation, since few storms initiate in this region (Figure 4.2c, Figure 4.3d). Convection initiation is nearly random over homogeneous vegetation, regardless of whether or not cold pools are present, so the disaggregating effect of cold pools on convection initiation locations is only important for heterogeneous vegetation (Figure 4.2e,f, Figure 4.3a, Figure 4.4c,d).

The results of this study indicate that the interactions between heterogeneous surfaces and cold pools are crucial for convection initiation patterns. While our simulations are representative of convection in the Amazon rainforest, we suggest that cold pools can similarly counteract the effects of heterogeneous vegetation in other environments. The effect of cold pools may be larger in regions drier than the Amazon where cold pools can have larger evaporatively-generated temperature deficits. Accurately parameterizing interactions between heterogeneous surfaces and cold pools may improve the ability of climate models to represent convection initiation, especially for heterogeneous surfaces resulting from anthropogenic activity. While not tested in this study, the background wind also certainly plays an important role. The background wind is coincidentally approximately perpendicular to the solenoidal circulations. A background wind parallel with the solenoidal circulations could cause storms and cold pools to form in different locations, potentially changing these results. We also did not test the spatial scale of heterogeneity, but past work has shown this scale can be important for convection initiation (Rieck et al. 2014; Khanna et al. 2017), and hence this should be tested. Many previous modeling studies have also altered evaporation to weaken cold pools (e.g. Khairoutdinov and Randall 2006; Jeevanjee and Romps 2013; Grant et al. 2018, 2020), but most of these studies did not consider heterogenous land surfaces. Our results suggest that the role of cold pools may be larger than what is presented in such studies, as cold pools have a greater impact on convection initiation over heterogeneous vegetation than homogeneous land surfaces. Finally, an important takeaway from this study is that, while deforestation and other land use changes may reduce precipitation in certain regions, cold pools partially counteract these changes.

4.5 Figures

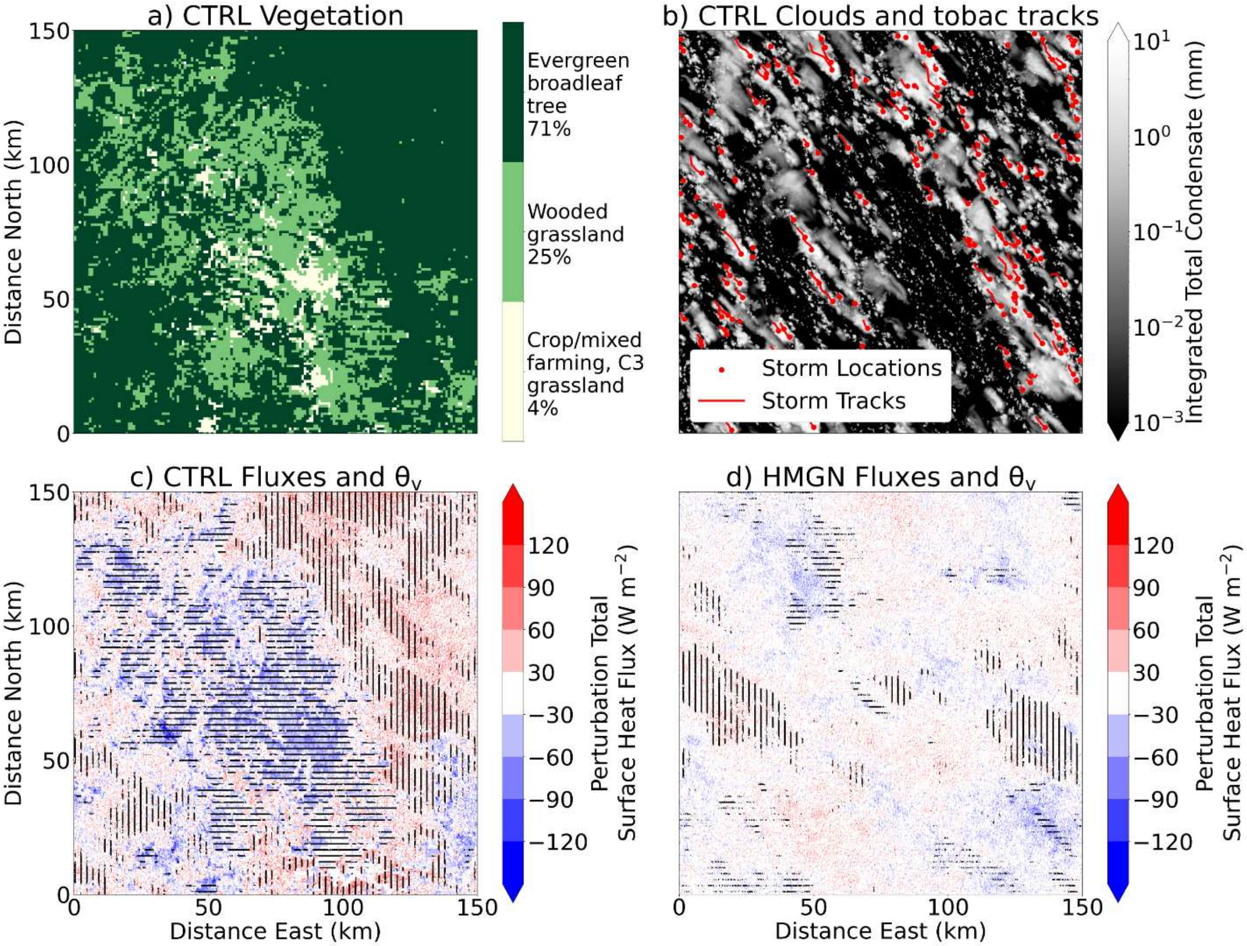

Figure 4.1. **Overview of vegetation pattern, storms, surface fluxes, and virtual potential temperature.** (a) Vegetation class in CTRL (shading) with percent of the domain covered by each class indicated in the colorbar. (b) Vertically integrated total condensate (shading), *tobac*-identified storm locations (red points), and storm tracks (red lines) in CTRL at 1200 LT on day one. (c) Perturbation total surface heat flux (shading) and 25 m perturbation virtual potential temperature (vertical hatching for >0.25 K, horizontal hatching for <-0.25 K) in CTRL. Perturbations are calculated from the domain- and time-mean at 0930 LT across all 5 simulated days. (d) As in (c) but for HMGN.

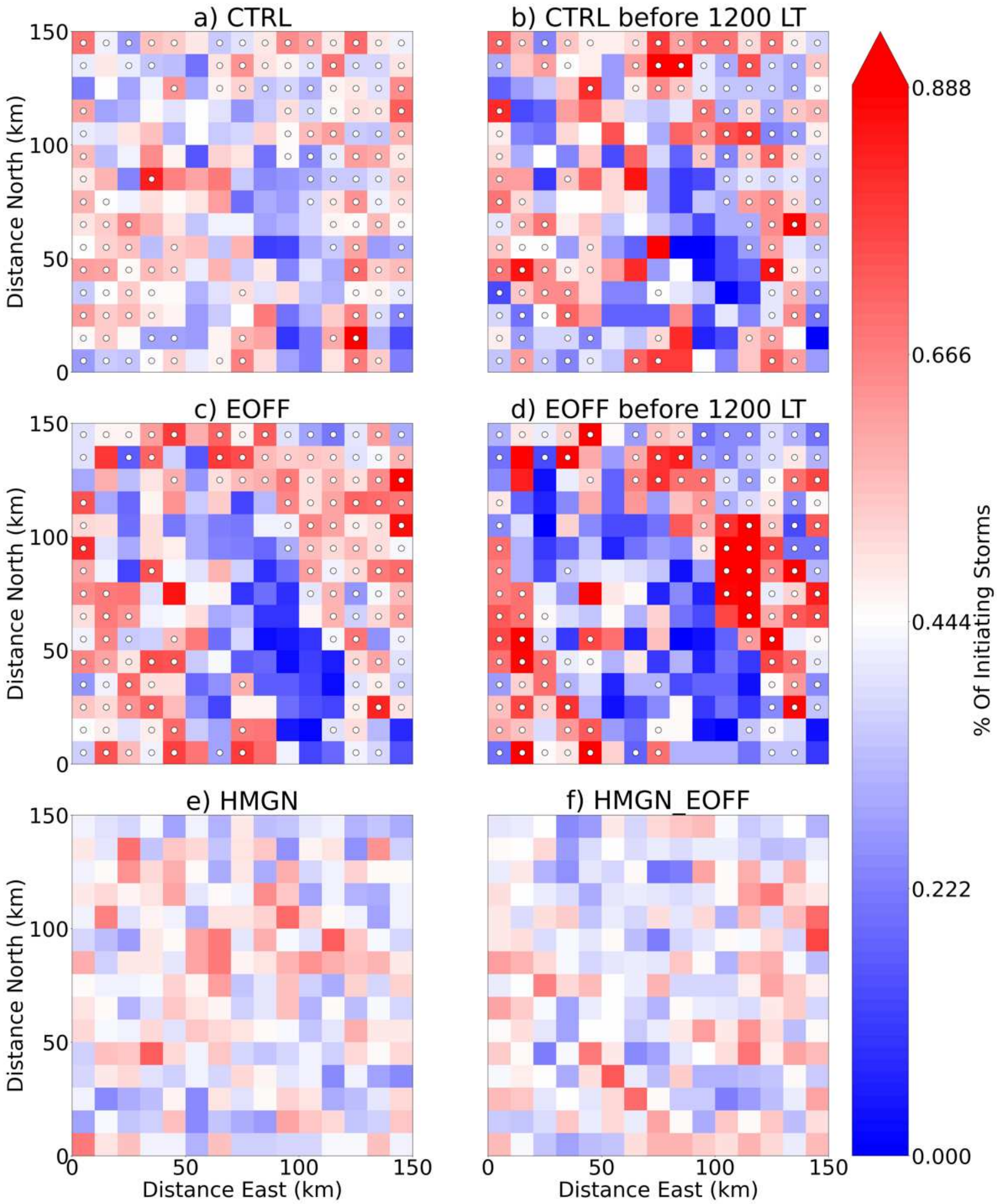

Figure 4.2: **Storms initiate more frequently over forests than over deforested areas, especially when cold pools are not present.** (a,c,e,f) Heatmaps of storm initiation locations for CTRL, EOFF, HMGN, and HMGN_EOFF, respectively. (b,d) as in (a,c) but only looking at storms which initiate between 0000 LT and 1155 LT. White dots indicate bins where the vegetation is >71% evergreen broadleaf tree. The colorbar is scaled such that if storms initiated uniformly across the domains, the panels would be white.

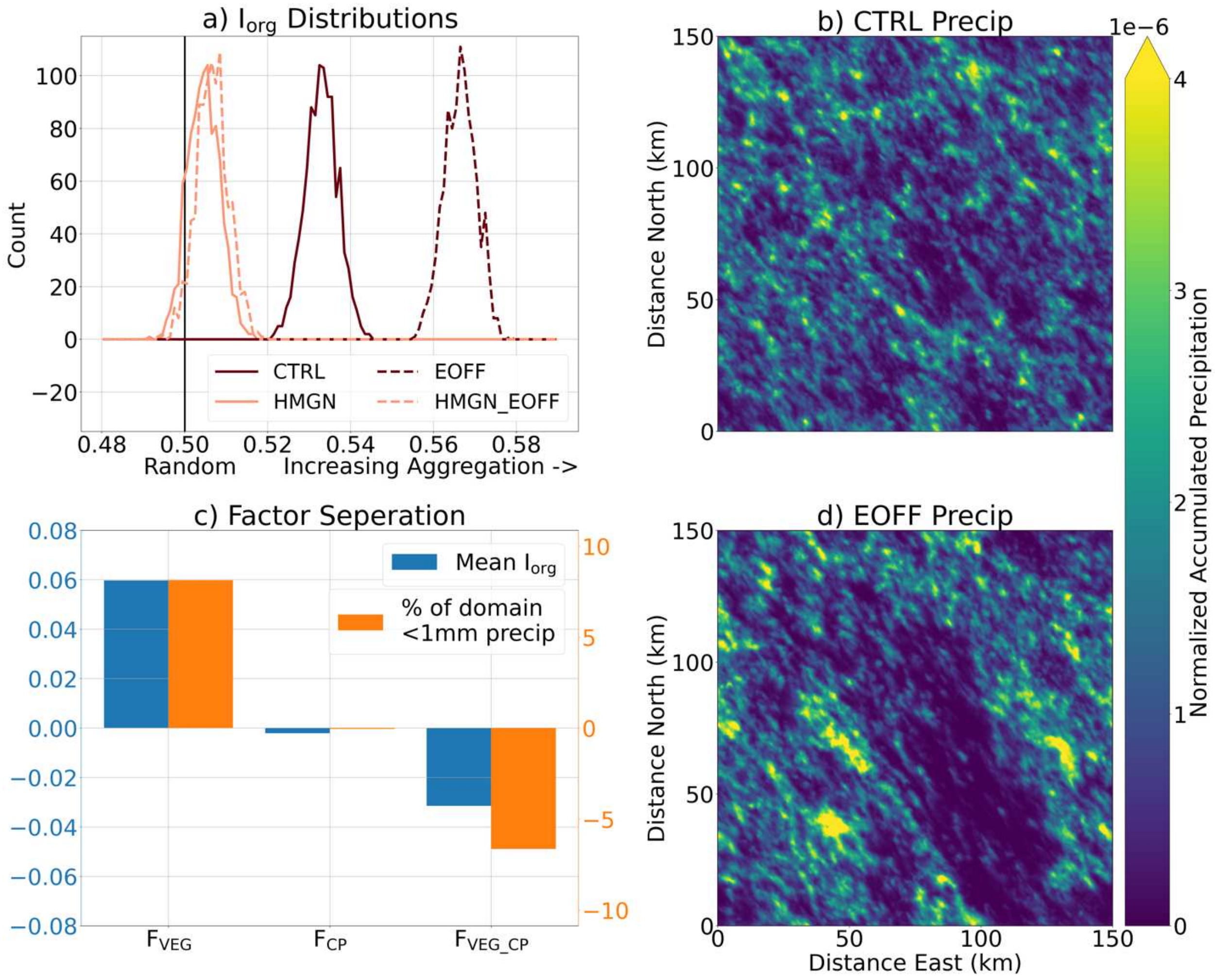

Figure 4.3: **Cold pools disaggregate storm initiation locations and accumulated precipitation over heterogeneous vegetation.** (a) Distributions of I_{org} of storm initiation locations for each simulation. (b,d) Normalized accumulated precipitation over the five simulated days (shading) for (b) CTRL and (d) EOFF. (c) Factor separation analysis of mean I_{org} values and percentage area receiving <1 mm of precipitation.

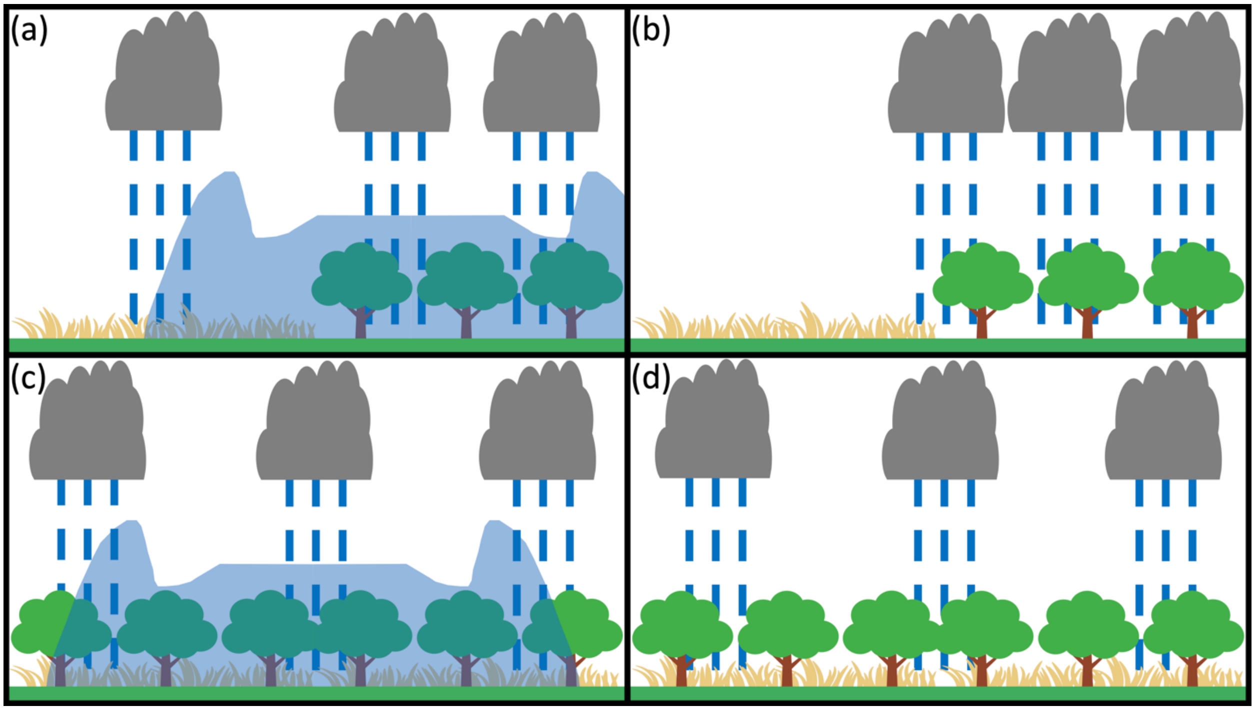

Figure 4.4: **Schematic summary of results**. (a) Storms form more frequently over forested regions, but cold pools (blue shading) can assist in initiating storms over deforested areas. (b) Without cold pools, almost all storms form over forested regions due to more favorable thermodynamics compared to deforested regions. (c,d) Storms form randomly over heterogeneous surfaces with or without cold pools.

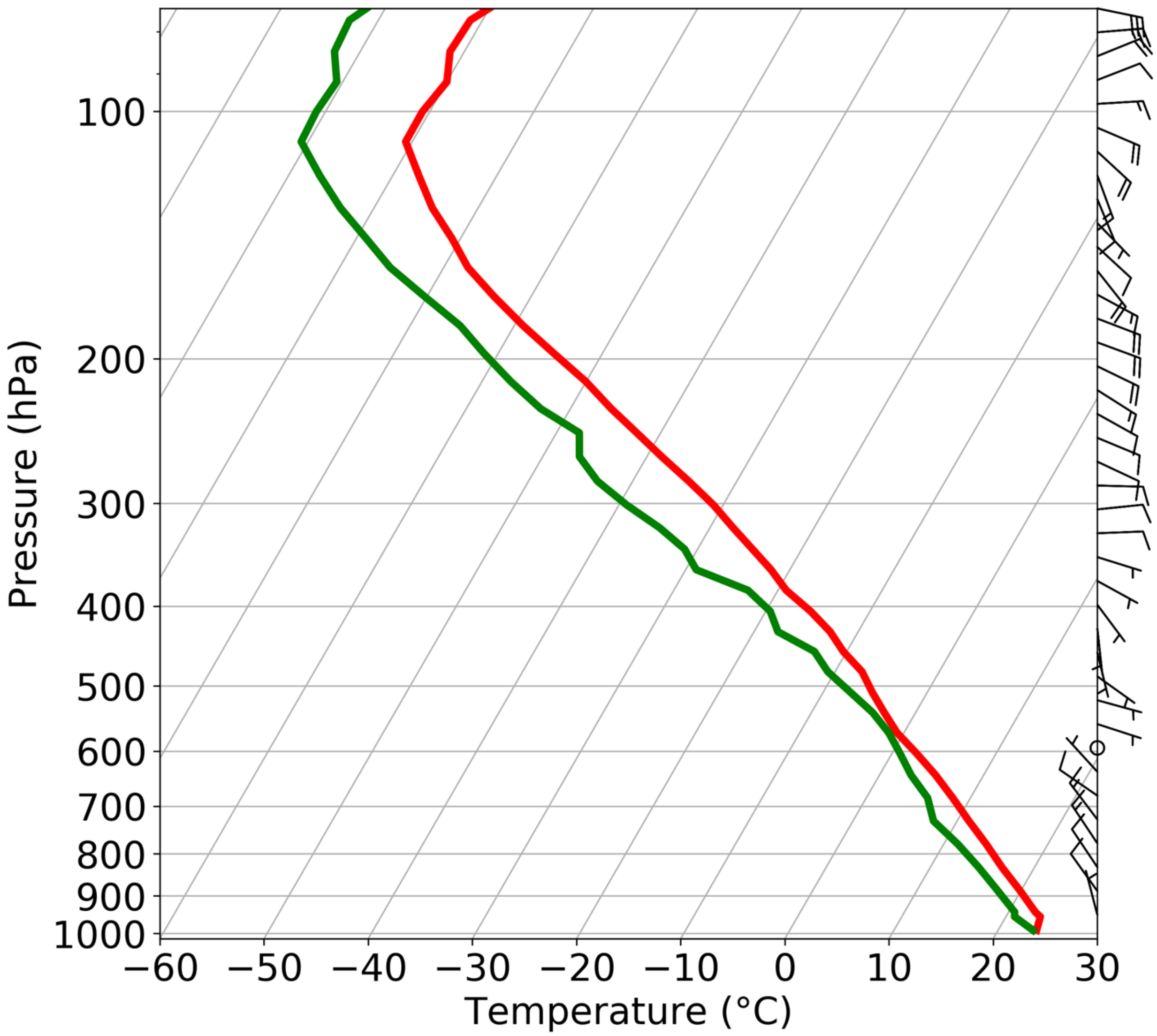

Figure 4.5: Skew T-log p diagram of the initial sounding.

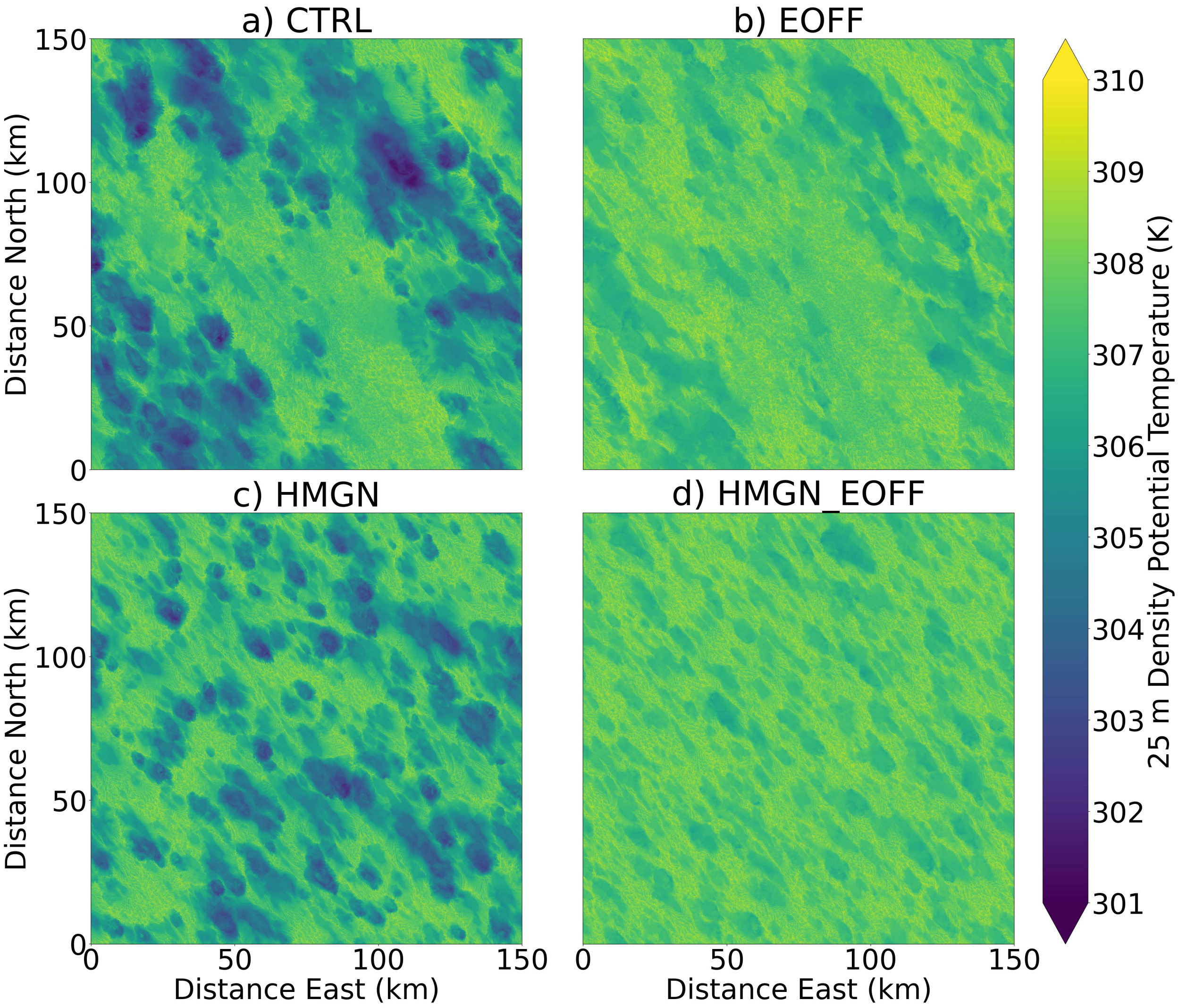

Figure 4.6: Density potential temperature at 25 m in all simulations at 1330 LT on day one.

Table 4.1: Select surface properties.

	Evergreen broadleaf tree	Wooded grassland	Crop/mixed farming	HMGN and HMGN_EOFF (all points)
Surface roughness length (m)	4.369	0.910	0.123	3.333
Albedo	0.159	0.180	0.192	0.166

Chapter 5: Conclusions

5.1 Summary of Results

Convective cold pools are an important atmospheric phenomenon as they are common, and can initiate and organize convection, create damaging wind gusts which may intensify wildfires, loft dust into the atmosphere, and alter the fluxes of energy between the atmosphere and Earth's surface (Purdom 1976; Johnson and Nicholls 1983; Rotunno et al. 1988; Knippertz et al. 2007; Bresch et al. 2021; Squitieri et al. 2023). Cold pools are difficult to study for multiple reasons. Targeted observations, such as coordinated radiosonde launches (van den Heever et al. 2021) or dense surface station networks (Kirsch et al. 2024), are often needed to appropriately observe cold pools. Numerically modeling cold pools requires fine grid spacings which increase the computational expense of such simulations (Straka et al. 1993; Grant and van den Heever 2016; Hirt et al. 2020; Fiévet et al. 2023). To overcome these challenges, the research presented in this dissertation has used such targeted observations and high-resolution simulations to investigate cold pool propagation and cold pool-land surface interactions.

While a theory exists around the propagation of density currents (Benjamin 1968), the applicability of this theory to cold pools has hitherto been unclear. Chapter 2 uses novel sonde observations of cold pools to evaluate this theory. Haboobs (dusty cold pools) are known to occur in areas of complex topography (Knippertz et al. 2007), but the effects of such topography on haboobs and the dust loft have not previously been examined in a systematic manner. Chapter 3 uses LES to explore topographic effects on haboobs and how these effects are modulated by other factors. Finally, both solenoidal circulations driven by land surface heterogeneity and cold pools are known to initiate convection (Purdom 1976; Chen and Avissar 1994), but the effects of the interactions between these phenomena on convection initiation are unclear. Chapter 4 uses LES to investigate such interactions. The findings of each chapter are detailed as follows.

First, in Chapter 2, the applicability of a cold pool propagation speed equation (EQ-RKW88) to observed cold pools is evaluated. Observations of cold pools from three field campaigns are used in this chapter. For each observed cold pool, a sonde-based propagation speed is calculated by applying EQ-RKW88 to a pair of sondes launched inside of and outside of the cold pool. For comparison, remote sensing data are used to calculate a radar/satellite-based propagation speed for each cold pool. The results of this study demonstrate that EQ-RKW88 is appropriate to apply to US High Plains cold pools as sonde-based and radar-based propagation speeds are highly correlated in this environment. A Froude number of 0.9-1.2 is recommended for parameterizing US High Plains cold pools. Similar recommendations could not be made for Philippine Sea and South China Sea cold pools due to the small sample size of observations in our database. It has also been found that sonde-based propagation speeds are insensitive to the method with which cold pool depth is calculated as cold pools usually have most of their negative buoyancy near the surface. The effects of the infinite channel depth assumption and the incompressible assumption used when deriving EQ-RKW88 are also explored. Both of these assumptions lead to greater sonde-based propagation speeds, with the former found to be more impactful than the latter. Finally, it is determined that sub-mesoscale variability may be important for cold pool propagation speeds, as sonde-based propagation speeds can vary by ~300% based on where and when the sondes were launched.

Second, the impacts of topographic slope, surface roughness, and dust-radiative interactions on daytime haboob propagation and dust lofting are examined in Chapter 3. Idealized LES of haboobs are conducted where the topographic slope, surface roughness, and dust-radiative interactions are varied. An algorithm is developed to track haboob boundaries and determine separate downslope and upslope propagation speeds. As surface roughness is increased, haboobs propagate slower and loft less dust on flat terrain due to faster dissipation from greater sensible heat fluxes. It is determined that steeper slopes and higher surface roughnesses both drive faster anabatic winds. These anabatic winds cause haboobs on sloped terrain to propagate faster upslope than they propagate downslope. Faster anabatic wind speeds also cause increasing amounts of dust to be lofted. The effects of dust-radiative interactions are found to be small, indicating that these effects are minimal for short-lived haboobs. The results of this chapter suggest that improving the representation of anabatic winds around complex topography, and improving how these winds interact with haboobs, may improve the representation of haboobs in forecast and climate models. The impacts of topographic slope on haboobs may be substantially different at night given the presence of katabatic winds and stable stratification.

Third, the individual and synergetic effects of cold pools and surface heterogeneity on convection initiation are explored in Chapter 4. Idealized LES of deep convection over the Amazon rainforest are conducted. Simulations vary two vegetation settings – realistic and homogenized – and two evaporation settings – realistic and disabled in the lowest 2 km to eliminate cold pools. Storm initiation locations are determined by tracking storms with *tobac*. The organization index is used to determine how aggregated the initiation locations are, and the factor separation method is used to disentangle the individual and synergistic effects of cold pools and heterogeneous vegetation on convection initiation. The findings from this study show that storms form more frequently over areas with rainforest than deforested areas due to the rainforest having more favorable thermodynamics and solenoidal circulations. However, cold pools can propagate into deforested areas and initiate convection. Thus, storm initiation locations are aggregated by heterogeneous surfaces, but the presence of cold pools disaggregate storm initiation locations and hence oppose the effect of heterogeneous surfaces. The impact of cold pools on disaggregation of convection initiation is only significant for heterogeneous surfaces: with homogeneous surfaces, initiation locations are approximately random, regardless of whether or not cold pools are present. The results of this chapter suggest that improving the representation of cold pool-solenoidal circulation interactions in climate models may improve these models' ability to represent convection initiation. Similar mechanisms may cause cold pools to disaggregate storm initiation locations in regions outside of the Amazon rainforest.

Taken together, the three studies of this dissertation indicate that the propagation of cold pools is theoretically well understood, can be strongly influenced by background winds, and can cause storms to initiate in otherwise unfavored locations. Land surface properties such as topographic slope, surface roughness, and vegetation play an important role in both directly and indirectly influencing cold pool propagation and convection initiation by cold pools. Beyond the avenues of research recommended within each individual chapter, the combined research in this dissertation leads to a number of further interesting scientific topics of exploration, discussed below.

5.2 Future Work

What controls cold pool body depth, cold pool head depth, and the ratio between the two? Cold pool depth is important for processes such as convection initiation, as it determines the depth to which ambient air is lifted (e.g. Weisman and Rotunno 2004). Factors such as vertical wind shear and static stability are known to impact the depth of cold pools (Liu and Moncrieff

2000; Weisman and Rotunno 2004; Seigel and van den Heever 2012b). However, as discussed in Chapter 2, cold pool depth is still understudied. This is complicated by the fact that cold pool depth is difficult to identify and, as such, is often determined in different ways by different studies. Observations of cold pool depth are limited, again because cold pool depth is difficult to explicitly identify and, as such, non-trivial to observe. Studies using instrumented towers often argue they have not observed the tops of cold pools unless the cold pool in question is clearly shallower than the tower (Charba 1974; Mai et al. 2023), while radiosondes require field campaign funds and only offer occasional observations of single profiles. Remote sensing techniques perhaps offer the best promise of expanded observations of cold pool depth. It may be possible to train a machine learning algorithm to automatically identify cold pool depth in remotely sensed data, which would greatly increase available cold pool depth observations. With such an expanded dataset, one could then thoroughly explore how environmental factors influence observed cold pool depths. However, it is unclear if creating such a dataset is possible given current remote sensing capabilities, or if new spaceborne instruments are needed.

What are the physical mechanisms by which the interactions between horizontal convective rolls and cold pools initiate convection? And what factors influence these mechanisms? Horizontal convective rolls are a form of dry convection which form in the planetary boundary layer (Weckwerth et al. 1997, 1999). Convection initiates due to enhanced moisture in the updrafts of horizontal convective rolls (Weckwerth et al. 1996; Weckwerth 2000). For example, cold pools and horizontal convective rolls were observed to interact and initiate convection during BACS IOP21. Analysis of data collected during IOP21 and case-study model simulations of this day could be used to understand the interactions between horizontal convective rolls and cold pools. From this initial investigation, future work could more fully explore the physical mechanisms and parameter space influencing cold pool-roll interactions.

Do cold pools reduce the size of rain shadows? It was shown in Chapter 4 that heterogeneous vegetation can create precipitation gaps (regions where little precipitation occurs), but that cold pools may reduce the size of precipitation gaps. These vegetation-driven precipitation gaps seem similar to rain shadows, except perhaps being on a smaller scale, which are known to form on the lee sides of mountain ranges. Thus, it would be interesting to investigate if cold pools also reduce the size of rain shadows. Like with vegetation-driven precipitation gaps, cold pools may propagate into rain shadows and help to initiate convection that would otherwise not occur. This hypothesis could be tested by running a set of idealized simulations with terrain and eliminating cold pools in some simulations by disabling low-level evaporation.

What are the effects of cold pools on a global scale? Global storm resolving models (GSRMs), which simulate the entire earth with a O(1km) horizontal grid spacing, are becoming increasingly common (Stevens et al. 2019). Such grid spacings are not ideal for simulating cold pools (Straka et al. 1993; Grant and van den Heever 2016; Hirt et al. 2020; Fiévet et al. 2023), but global simulations using finer grid spacings are still challenging. It would be elucidating to run a GSRM simulation with low-level evaporation disabled in order to eliminate cold pools. While this technique has been used in many previous studies, these studies have all been conducted with limited-area models. Comparing such a GSRM experiment in which cold pools have been removed to a control simulation containing cold pools would allow for the effects of cold pools on a global scale to be explored for the first time. Given that cold pools are known to be important for the initiation of tropical convection (Tompkins 2001; Torri et al. 2015; Feng et al. 2015), and that tropical convection helps drive the general circulation (Riehl and Malkus 1958), it is possible that the general circulation may be substantially different without cold pools.

There remain many unknowns about convective cold pools. Through carefully designed field experiments and numerical simulations, this dissertation research has clarified several points regarding cold pool propagation and cold pool-land surface interactions. Future studies should continue to use cutting edge field work, simulations, and laboratory experiments to study convective cold pools.

References

Adams, D. K., and A. C. Comrie, 1997: The north American monsoon. *Bull. Am. Meteorol. Soc.*, **78**, 2197–2213.

Adebiyi, A., and Coauthors, 2023: A review of coarse mineral dust in the Earth system. *Aeolian Research*, **60**, 100849.

Alvalá, R. C. S., and Coauthors, 2002: Intradiurnal and seasonal variability of soil temperature, heat flux, soil moisture content, and thermal properties under forest and pasture in Rondônia. *Journal of Geophysical Research: Atmospheres*, **107**, LBA 10-1-LBA 10-20.

Ansmann, A., and Coauthors, 2017: Profiling of Saharan dust from the Caribbean to western Africa -- Part 2: Shipborne lidar measurements versus forecasts. *Atmospheric Chemistry and Physics*, **17**, 14987–15006.

Ascher, B. D., S. M. Saleeby, P. J. Marinescu, and S. C. van den Heever, 2024: Forest Breeze - Cold Pool Interactions Drive Convective Organization over Heterogeneous Vegetation. *J. Atmos. Sci.*, https://doi.org/10.1175/JAS-D-24-0084.1.

Ashley, W. S., S. Strader, D. C. Dziubla, and A. Haberlie, 2015: Driving Blind: Weather-Related Vision Hazards and Fatal Motor Vehicle Crashes. *Bull. Am. Meteorol. Soc.*, **96**, 755–778.

Babin, S. M., J. A. Carton, T. D. Dickey, and J. D. Wiggert, 2004: Satellite evidence of hurricane-induced phytoplankton blooms in an oceanic desert. *Journal of Geophysical Research: Oceans*, **109**, https://doi.org/10.1029/2003JC001938.

Bao, X., and F. Zhang, 2013: Impacts of the mountain–plains solenoid and cold pool dynamics on the diurnal variation of warm-season precipitation over northern China. *Atmospheric Chemistry and Physics*, **13**, 6965–6982.

Benjamin, T. B., 1968: Gravity currents and related phenomena. *J. Fluid Mech.*, **31**, 209–248.

Bergametti, G., and Coauthors, 2017: Dust Uplift Potential in the Central Sahel: An Analysis Based on 10 years of Meteorological Measurements at High Temporal Resolution. *J. Geophys. Res.*, **122**, 12,433-12,448.

Birch, C. E., M. J. Roberts, L. Garcia-Carreras, D. Ackerley, M. J. Reeder, A. P. Lock, and R. Schiemann, 2015: Sea-Breeze Dynamics and Convection Initiation: The Influence of Convective Parameterization in Weather and Climate Model Biases. *J. Clim.*, **28**, 8093–8108.

Borque, P., S. W. Nesbitt, R. J. Trapp, S. Lasher-Trapp, and M. Oue, 2020: Observational Study of the Thermodynamics and Morphological Characteristics of a Midlatitude Continental Cold Pool Event. *Mon. Weather Rev.*, **148**, 719–737.

Branch, O., and V. Wulfmeyer, 2019: Deliberate enhancement of rainfall using desert plantations. *Proceedings of the National Academy of Sciences*, **116**, 18841–18847.

Bresch, J. F., J. G. Powers, C. S. Schwartz, R. A. Sobash, and J. L. Coen, 2021: Objective identification of thunderstorm gust fronts in numerical weather prediction models for fire weather forecasting. *Int. J. Wildland Fire*, **30**, 513–535.

Bristow, C. S., K. A. Hudson-Edwards, and A. Chappell, 2010: Fertilizing the Amazon and equatorial Atlantic with West African dust. *Geophysical Research Letters*, **37**, https://doi.org/10.1029/2010GL043486.

Bryan, G., D. Ahijevych, C. Davis, M. Weisman, and R. Przybylinski, 2004: An assessment of convective system structure, cold pool properties, and environmental shear using observations from BAMEX. *Preprints, 22nd Conf. on Severe Local Storms, Hyannis, MA, Amer. Meteor. Soc*.

Bryan, G., D. Ahijevych, C. Davis, S. Trier, and M. Weisman, 2005: Observations of cold pool properties in mesoscale convective systems during BAMEX. *Preprints, 11th Conf. on Mesoscale Processes, Albuquerque, NM, Amer. Meteor. Soc.*, ams.confex.com https://ams.confex.com/ams/32Rad11Meso/techprogram/paper_96718.htm.

Bryan, G. H., and R. Rotunno, 2008: Gravity Currents in a Deep Anelastic Atmosphere. *J. Atmos. Sci.*, **65**, 536–556.

——, and M. D. Parker, 2010: Observations of a Squall Line and Its Near Environment Using High-Frequency Rawinsonde Launches during VORTEX2. *Mon. Weather Rev.*, **138**, 4076–4097.

Bukowski, J., and S. C. van den Heever, 2020: Convective distribution of dust over the Arabian Peninsula: the impact of model resolution. *Atmospheric Chemistry and Physics*, **20**, 2967–2986.

——, and ——, 2021: Direct radiative effects in haboobs. *J. Geophys. Res.*, **126**, https://doi.org/10.1029/2021jd034814.

——, and ——, 2022: The Impact of Land Surface Properties on Haboobs and Dust Lofting. *J. Atmos. Sci.*, **79**, 3195–3218.

Byers, H. R., and R. R. Braham, 1949: *The Thunderstorm: Report of the Thunderstorm Project*. U.S. Government Printing Office, 287 pp.

Caton Harrison, T., R. Washington, and S. Engelstaedter, 2021: Satellite-derived characteristics of Saharan cold pool outflows during boreal summer. *J. Geophys. Res.*, **126**, https://doi.org/10.1029/2020jd033387.

Chagnon, F. J. F., R. L. Bras, and J. Wang, 2004: Climatic shift in patterns of shallow clouds over the Amazon. *Geophysical Research Letters*, **31**, https://doi.org/10.1029/2004GL021188.

Charba, J., 1974: Application of Gravity Current Model to Analysis of Squall-Line Gust Front. *Mon. Weather Rev.*, **102**, 140–156.

Chen, F., and R. Avissar, 1994: Impact of Land-Surface Moisture Variability on Local Shallow Convective Cumulus and Precipitation in Large-Scale Models. *J. Appl. Meteorol. Climatol.*, **33**, 1382–1401.

Chen, J., S. Hagos, H. Xiao, J. D. Fast, and Z. Feng, 2020: Characterization of Surface Heterogeneity-Induced Convection Using Cluster Analysis. *Journal of Geophysical Research: Atmospheres*, **125**, e2020JD032550.

Cheng, W. Y. Y., and W. R. Cotton, 2004: Sensitivity of a Cloud-Resolving Simulation of the Genesis of a Mesoscale Convective System to Horizontal Heterogeneities in Soil Moisture Initialization. *J. Hydrometeorol.*, **5**, 934–958.

Cheng, W.-Y., D. Kim, and A. Rowe, 2018: Objective quantification of convective clustering observed during the AMIE/DYNAMO two-day rain episodes. *J. Geophys. Res.*, **123**, 10,361-10,378.

Cioni, G., and C. Hohenegger, 2018: A simplified model of precipitation enhancement over a heterogeneous surface. *Hydrol. Earth Syst. Sci.*, **22**, 3197–3212.

Coniglio, M. C., and M. D. Parker, 2020: Insights into Supercells and Their Environments from Three Decades of Targeted Radiosonde Observations. *Mon. Weather Rev.*, **148**, 4893–4915.

——, S. F. Corfidi, and J. S. Kain, 2012: Views on Applying RKW Theory: An Illustration Using the 8 May 2009 Derecho-Producing Convective System. *Mon. Weather Rev.*, **140**, 1023–1043.

Cotton, W. R., and Coauthors, 2003: RAMS 2001: Current status and future directions. *Meteorol. Atmos. Phys.*, **82**, 5–29.

Craig Goff, R., 1976: Vertical Structure of Thunderstorm Outflows. *Mon. Weather Rev.*, **104**, 1429–1440.

Crook, N. A., and M. W. Moncrieff, 1988: The Effect of Large-Scale Convergence on the Generation and Maintenance of Deep Moist Convection. *J. Atmos. Sci.*, **45**, 3606–3624.

Da, C., 2015: Preliminary assessment of the Advanced Himawari Imager (AHI) measurement onboard Himawari-8 geostationary satellite. *Remote Sens. Lett.*, **6**, 637–646.

Dai, A., and Y.-L. Huang, 2016: High-resolution simulations of non-Boussinesq downslope gravity currents in the acceleration phase. *Phys. Fluids*, **28**, 026602.

——, C. E. Ozdemir, M. I. Cantero, and B. S., 2012: Gravity Currents from Instantaneous Sources Down a Slope. *Journal of Hydraulic Engineering*, **138**, 237–246.

De Falco, M. C., L. Ottolenghi, and C. Adduce, 2020: Dynamics of Gravity Currents Flowing Up a Slope and Implications for Entrainment. *Journal of Hydraulic Engineering*, **146**, 04020011.

Defant, F., 1951: Local Winds. *Compendium of Meteorology: Prepared under the Direction of the Committee on the Compendium of Meteorology*, T.F. Malone, Ed., American Meteorological Society, 655–672.

DeMott, P. J., K. Sassen, M. R. Poellot, D. Baumgardner, D. C. Rogers, S. D. Brooks, A. J. Prenni, and S. M. Kreidenweis, 2003: African dust aerosols as atmospheric ice nuclei. *Geophysical Research Letters*, **30**, https://doi.org/10.1029/2003GL017410.

Dhital, S., M. L. Kaplan, J. A. G. Orza, and S. Fiedler, 2022: The Extreme North African Haboob in October 2008: High-Resolution Simulation of Organized Moist Convection in the Lee of the Atlas, Dust Recirculation and Poleward Transport. *Journal of Geophysical Research: Atmospheres*, **127**, e2021JD035858.

Drager, A. J., and S. C. van den Heever, 2017: Characterizing convective cold pools. *J. Adv. Model. Earth Syst.*, **9**, 1091–1115.

——, L. D. Grant, and S. C. Heever, 2020: Cold pool responses to changes in soil moisture. *J. Adv. Model. Earth Syst.*, **12**, https://doi.org/10.1029/2019ms001922.

Droegemeier, K. K., and R. B. Wilhelmson, 1985: Three-dimensional numerical modeling of convection produced by interacting thunderstorm outflows. Part I: Control simulation and low-level moisture variations. *Journal of Atmospheric Sciences*, **42**, 2381–2403.

——, and ——, 1987: Numerical Simulation of Thunderstorm Outflow Dynamics. Part I: Outflow Sensitivity Experiments and Turbulence Dynamics. *J. Atmos. Sci.*, **44**, 1180–1210.

Durieux, L., L. A. T. Machado, and H. Laurent, 2003: The impact of deforestation on cloud cover over the Amazon arc of deforestation. *Remote Sens. Environ.*, **86**, 132–140.

Emmel, C., P. Knippertz, and O. Schulz, 2010: Climatology of convective density currents in the southern foothills of the Atlas Mountains. *Journal of Geophysical Research: Atmospheres*, **115**, https://doi.org/10.1029/2009JD012863.

Falk, N. M., and S. C. van den Heever, 2023: Environmental Modulation of Mechanical and Thermodynamic Forcing from Cold Pool Collisions. *J. Atmos. Sci.*, **80**, 375–395.

Farquharson, J. S., 1937: Haboobs and instability in the sudan. *Quart. J. Roy. Meteor. Soc.*, **63**, 393–414.

Fécan, F., B. Marticorena, and G. Bergametti, 1999: Parametrization of the increase of the aeolian erosion threshold wind friction velocity due to soil moisture for arid and semi-arid areas. *Ann. Geophys.*, **17**, 149–157.

Feng, Z., S. Hagos, A. K. Rowe, C. D. Burleyson, M. N. Martini, and S. P. Szoeke, 2015: Mechanisms of convective cloud organization by cold pools over tropical warm ocean during the AMIE/DYNAMO field campaign. *Journal of Advances in Modeling Earth Systems*, **7**, 357–381.

Field, P. R., O. Möhler, P. Connolly, M. Krämer, R. Cotton, A. J. Heymsfield, H. Saathoff, and M. Schnaiter, 2006: Some ice nucleation characteristics of Asian and Saharan desert dust. *Atmospheric Chemistry and Physics*, **6**, 2991–3006.

Fiévet, R., B. Meyer, and J. O. Haerter, 2023: On the Sensitivity of Convective Cold Pools to Mesh Resolution. *Journal of Advances in Modeling Earth Systems*, **15**, e2022MS003382.

Findell, K. L., and E. A. B. Eltahir, 2003a: Atmospheric controls on soil moisture-boundary layer interactions: Three-dimensional wind effects. *Journal of Geophysical Research: Atmospheres*, **108**, https://doi.org/10.1029/2001JD001515.

——, and ——, 2003b: Atmospheric Controls on Soil Moisture–Boundary Layer Interactions. Part I: Framework Development. *J. Hydrometeorol.*, **4**, 552–569.

Flamant, C., J.-P. Chaboureau, D. J. Parker, C. M. Taylor, J.-P. Cammas, O. Bock, F. Timouk, and J. Pelon, 2007: Airborne observations of the impact of a convective system on the planetary boundary layer thermodynamics and aerosol distribution in the inter-tropical discontinuity region of the West African Monsoon. *Quarterly Journal of the Royal Meteorological Society*, **133**, 1175–1189.

Garcia-Carreras, L., D. J. Parker, and J. H. Marsham, 2011: What is the Mechanism for the Modification of Convective Cloud Distributions by Land Surface–Induced Flows? *J. Atmos. Sci.*, **68**, 619–634.

Garcia-Carreras, L., and Coauthors, 2013: The impact of convective cold pool outflows on model biases in the Sahara. *Geophysical Research Letters*, **40**, 1647–1652.

Gentine, P., A. Garelli, S.-B. Park, J. Nie, G. Torri, and Z. Kuang, 2016: Role of surface heat fluxes underneath cold pools. *Geophys. Res. Lett.*, **43**, 874–883.

Ginoux, P., M. Chin, I. Tegen, J. M. Prospero, B. Holben, O. Dubovik, and S.-J. Lin, 2001: Sources and distributions of dust aerosols simulated with the GOCART model. *Journal of Geophysical Research: Atmospheres*, **106**, 20255–20273.

——, J. M. Prospero, T. E. Gill, N. C. Hsu, and M. Zhao, 2012: Global-scale attribution of anthropogenic and natural dust sources and their emission rates based on MODIS Deep Blue aerosol products. *Reviews of Geophysics*, **50**, https://doi.org/10.1029/2012RG000388.

Grabowski, W. W., and Coauthors, 2006: Daytime convective development over land: A model intercomparison based on LBA observations. *Quart. J. Roy. Meteor. Soc.*, **132**, 317–344.

Grant, L. D., and S. C. van den Heever, 2016: Cold pool dissipation. *Journal of Geophysical Research Atmospheres*, **121**, 1138–1155.

——, and ——, 2018: Cold pool-land surface interactions in a dry continental environment. *J. Adv. Model. Earth Syst.*, **10**, 1513–1526.

——, T. P. Lane, and S. C. van den Heever, 2018: The Role of Cold Pools in Tropical Oceanic Convective Systems. *J. Atmos. Sci.*, **75**, 2615–2634.

——, M. W. Moncrieff, T. P. Lane, and S. C. van den Heever, 2020: Shear-Parallel Tropical Convective Systems: Importance of Cold Pools and Wind Shear. *Geophysical Research Letters*, **47**, e2020GL087720.

——, B. Kirsch, J. Bukowski, N. M. Falk, C. A. Neumaier, M. Sakradzija, S. C. van den Heever, and F. Ament, 2024: How Variable Are Cold Pools? *Geophys. Res. Lett.*, **51**, e2023GL106784.

Griffin, D. W., 2007: Atmospheric Movement of Microorganisms in Clouds of Desert Dust and Implications for Human Health. *Clinical Microbiology Reviews*, **20**, 459–477.

Harrington, J. Y., 1997: Effects of radiative and microphysical processes on simulated warm and transition season Arctic stratus. Colorado State University, 289 pp.

Harvey, N. J., C. L. Daleu, R. A. Stratton, R. S. Plant, S. J. Woolnough, and A. J. Stirling, 2022: The impact of surface heterogeneity on the diurnal cycle of deep convection. *Quarterly Journal of the Royal Meteorological Society*, **148**, 3509–3527.

Haywood, J., and Coauthors, 2003: Radiative properties and direct radiative effect of Saharan dust measured by the C-130 aircraft during SHADE: 1. Solar spectrum. *Journal of Geophysical Research: Atmospheres*, **108**, https://doi.org/10.1029/2002JD002687.

He, Z., L. Zhao, T. Lin, P. Hu, Y. Lv, H.-C. Ho, and Y.-T. Lin, 2017: Hydrodynamics of Gravity Currents Down a Ramp in Linearly Stratified Environments. *Journal of Hydraulic Engineering*, **143**, 04016085.

van den Heever, S. C., and Coauthors, 2021: The Colorado State University Convective CLoud Outflows and UpDrafts Experiment (C3LOUD-Ex). *Bulletin of the American Meteorological Society*, **102**, E1283–E1305, https://doi.org/10.1175/bams-d-19-0013.1.

——, S. M. Saleeby, L. D. Grant, A. L. Igel, and S. W. Freeman, 2022: *RAMS - the Regional Atmospheric Modeling System*. Zenodo,.

——, ——, ——, ——, and ——, 2023: *RAMS - the Regional Atmospheric Modeling System*. Zenodo,.

Heikenfeld, M., P. J. Marinescu, M. Christensen, D. Watson-Parris, F. Senf, S. C. van den Heever, and P. Stier, 2019: Tobac 1.2: Towards a flexible framework for tracking and analysis of clouds in diverse datasets. *Geosci. Model Dev.*, **12**, 4551–4570.

Heinold, B., P. Knippertz, J. H. Marsham, S. Fiedler, N. S. Dixon, K. Schepanski, B. Laurent, and I. Tegen, 2013: The role of deep convection and nocturnal low-level jets for dust emission in summertime West Africa: Estimates from convection-permitting simulations. *J. Geophys. Res. Atmos.*, **118**, 4385–4400.

Hersbach, H., and Coauthors, 2020: The ERA5 global reanalysis. *Quarterly Journal of the Royal Meteorological Society*, **146**, 1999–2049.

Hill, G. E., 1974: Factors Controlling the Size and Spacing of Cumulus Clouds as Revealed by Numerical Experiments. *Journal of Atmospheric Sciences*, **31**, 646–673.

Hirt, M., G. C. Craig, S. A. K. Schäfer, J. Savre, and R. Heinze, 2020: Cold-pool-driven convective initiation: using causal graph analysis to determine what convection-permitting models are missing. *Quarterly Journal of the Royal Meteorological Society*, **146**, 2205–2227.

Hoeller, J., J. O. Haerter, and N. A. Da Silva, 2024: Characteristics of Station-Derived Convective Cold Pools Over Equatorial Africa. *Geophysical Research Letters*, **51**, e2023GL107308.

Hong, X., M. J. Leach, and S. Raman, 1995: A Sensitivity Study of Convective Cloud Formation by Vegetation Forcing with Different Atmospheric Conditions. *J. Appl. Meteorol. Climatol.*, **34**, 2008–2028.

Houston, A. L., and R. B. Wilhelmson, 2011: The Dependence of Storm Longevity on the Pattern of Deep Convection Initiation in a Low-Shear Environment. *Mon. Weather Rev.*, **139**, 3125–3138.

Huang, Q., J. H. Marsham, W. Tian, D. J. Parker, and L. Garcia-Carreras, 2018: Large-eddy simulation of dust-uplift by a haboob density current. *Atmos. Environ.*, **179**, 31–39.

Huppert, H. E., and J. E. Simpson, 1980: The slumping of gravity currents. *J. Fluid Mech.*, **99**, 785–799.

Intrieri, J. M., A. J. Bedard, and R. M. Hardesty, 1990: Details of Colliding Thunderstorm Outflows as Observed by Doppler Lidar. *J. Atmos. Sci.*, **47**, 1081–1099.

Jeevanjee, N., and D. M. Romps, 2013: Convective self-aggregation, cold pools, and domain size. *Geophys. Res. Lett.*, **40**, 994–998.

Johnson, R. H., and M. E. Nicholls, 1983: A Composite Analysis of the Boundary Layer Accompanying a Tropical Squall Line. *Mon. Weather Rev.*, **111**, 308–319.

——, R. S. Schumacher, J. H. Ruppert, D. T. Lindsey, J. E. Ruthford, and L. Kriederman, 2014: The Role of Convective Outflow in the Waldo Canyon Fire. *Mon. Weather Rev.*, **142**, 3061–3080.

Kanatani, K. T., I. Ito, W. K. Al-Delaimy, Y. Adachi, W. C. Mathews, and J. W. Ramsdell, 2010: Desert Dust Exposure Is Associated with Increased Risk of Asthma Hospitalization in Children. *American Journal of Respiratory and Critical Care Medicine*, **182**, 1475–1481.

von Kármán, T., 1940: The engineer grapples with nonlinear problems. *Bull. Am. Math. Soc.*, **46**, 615–683.

Keenan, T. D., and R. E. Carbone, 1992: A preliminary morphology of precipitation systems in tropical northern Australia. *Quart. J. Roy. Meteor. Soc.*, **118**, 283–326.

Khairoutdinov, M., and D. Randall, 2006: High-resolution simulation of shallow-to-deep convection transition over land. *J. Atmos. Sci.*, **63**, 3421–3436.

Khanna, J., D. Medvigy, S. Fueglistaler, and R. Walko, 2017: Regional dry-season climate changes due to three decades of Amazonian deforestation. *Nat. Clim. Chang.*, **7**, 200–204.

Kirsch, B., C. Hohenegger, D. Klocke, R. Senke, M. Offermann, and F. Ament, 2022: Sub-mesoscale observations of convective cold pools with a dense station network in Hamburg, Germany. *Earth System Science Data*, **14**, 3531–3548.

Kirsch, B., C. Hohenegger, and F. Ament, 2024: Morphology and growth of convective cold pools observed by a dense station network in Germany. *Quart. J. Roy. Meteor. Soc.*, **150**, 857–876.

Knippertz, P., and M. C. Todd, 2012: Mineral dust aerosols over the Sahara: Meteorological controls on emission and transport and implications for modeling. *Reviews of Geophysics*, **50**, https://doi.org/10.1029/2011RG000362.

——, Deutscher, C, K. Kandler, T. Müller, O. Schulz, and L. Schütz, 2007: Dust mobilization due to density currents in the Atlas region: Observations from the Saharan Mineral Dust Experiment 2006 field campaign. *Journal of Geophysical Research: Atmospheres*, **112**, https://doi.org/10.1029/2007JD008774.

Kok, J. F., T. Storelvmo, V. A. Karydis, A. A. Adebiyi, N. M. Mahowald, A. T. Evan, C. He, and D. M. Leung, 2023: Mineral dust aerosol impacts on global climate and climate change. *Nat. Rev. Earth Environ.*, **4**, 71–86.

Kurowski, M. J., K. Suselj, W. W. Grabowski, and J. Teixeira, 2018: Shallow-to-Deep Transition of Continental Moist Convection: Cold Pools, Surface Fluxes, and Mesoscale Organization. *J. Atmos. Sci.*, **75**, 4071–4090.

Lader, G., A. Raman, J. T. Davis, and K. Waters, 2016: Blowing dust and dust storms: One of Arizona's most underrated weather hazards. *NOAA technical memorandum NWSWR-290*.

Lafore, J.-P., and M. W. Moncrieff, 1989: A Numerical Investigation of the Organization and Interaction of the Convective and Stratiform Regions of Tropical Squall Lines. *J. Atmos. Sci.*, **46**, 521–544.

Li, J., T. Kandakji, J. A. Lee, J. Tatarko, J. Blackwell, T. E. Gill, and J. D. Collins, 2018: Blowing dust and highway safety in the southwestern United States: Characteristics of dust emission "hotspots" and management implications. *Sci. Total Environ.*, **621**, 1023–1032.

Lilly, D. K., 1962: On the numerical simulation of buoyant convection. *Tellus A*,.

Lima, M. A., and J. W. Wilson, 2008: Convective Storm Initiation in a Moist Tropical Environment. *Mon. Weather Rev.*, **136**, 1847–1864.

Liu, C., and M. W. Moncrieff, 2000: Simulated Density Currents in Idealized Stratified Environments. *Mon. Weather Rev.*, **128**, 1420–1437.

Liu, H., Q. Huang, Y. Chou, H. Tian, Y. Zhang, X. Wu, J. Zhang, and M. Wang, 2022: A Numerical Study of Downbursts Using the BLASIUS Model. *J. Appl. Meteorol. Climatol.*, **61**, 1065–1076.

Lombardi, V., C. Adduce, G. Sciortino, and M. La Rocca, 2015: Gravity currents flowing upslope: Laboratory experiments and shallow-water simulations. *Phys. Fluids*, **27**, 016602.

Lombardo, K., and M. R. Kumjian, 2022: Observations of the Discrete Propagation of a Mesoscale Convective System during RELAMPAGO–CACTI. *Mon. Weather Rev.*, **150**, 2111–2138.

Lothon, M., B. Campistron, M. Chong, F. Couvreux, F. Guichard, C. Rio, and E. Williams, 2011: Life Cycle of a Mesoscale Circular Gust Front Observed by a C-Band Doppler Radar in West Africa. *Mon. Weather Rev.*, **139**, 1370–1388.

Luchetti, N. T., K. Friedrich, and C. E. Rodell, 2020a: Evaluating Thunderstorm Gust Fronts in New Mexico and Arizona. *Mon. Weather Rev.*, **148**, 4943–4956.

——, ——, ——, and J. K. Lundquist, 2020b: Characterizing Thunderstorm Gust Fronts near Complex Terrain. *Mon. Weather Rev.*, **148**, 3267–3286.

Lugauer, M., and Coauthors, 2003: An overview of the VERTIKATOR project and results of Alpine pumping. International Conference Alpine Meteorology.

Lynn, B. H., W.-K. Tao, and P. J. Wetzel, 1998: A Study of Landscape-Generated Deep Moist Convection. *Mon. Weather Rev.*, **126**, 928–942.

Maddox, E. M., and G. L. Mullendore, 2018: Determination of Best Tropopause Definition for Convective Transport Studies. *J. Atmos. Sci.*, **75**, 3433–3446.

Mahowald, N. M., and Coauthors, 2010: Observed 20th century desert dust variability: impact on climate and biogeochemistry. *Atmospheric Chemistry and Physics*, **10**, 10875–10893.

Mai, C., Y. Du, and M. Li, 2023: Processes of Colliding Cold Pools Derived from a 356-m-High Shenzhen Met-Tower during an Extremely Heavy Rainfall Event. *Mon. Weather Rev.*, **151**, 1571–1585.

Marleau, L. J., M. R. Flynn, and B. R. Sutherland, 2014: Gravity currents propagating up a slope. *Phys. Fluids*, **26**, 046605.

Marsham, J. H., and Coauthors, 2013: Meteorology and dust in the central Sahara: Observations from Fennec supersite-1 during the June 2011 Intensive Observation Period. *Journal of Geophysical Research: Atmospheres*, **118**, 4069–4089.

Marticorena, B., and G. Bergametti, 1995: Modeling the atmospheric dust cycle: 1. Design of a soil-derived dust emission scheme. *J. Geophys. Res.*, **100**, 16415–16430.

Martin, J. H., R. M. Gordon, and S. E. Fitzwater, 1990: Iron in antarctic waters. *Nature*, **345**, 156–158.

Mascart, P., O. Taconet, J.-P. Pinty, and M. B. Mehrez, 1991: Canopy resistance formulation and its effect in mesoscale models: A HAPEX perspective. *Agric. For. Meteorol.*, **54**, 319–351.

Meyer, B., and J. O. Haerter, 2020: Mechanical Forcing of Convection by Cold Pools: Collisions and Energy Scaling. *J Adv Model Earth Syst*, **12**, e2020MS002281.

Miller, S. D., A. P. Kuciauskas, M. Liu, Q. Ji, J. S. Reid, D. W. Breed, A. L. Walker, and A. A. Mandoos, 2008: Haboob dust storms of the southern Arabian Peninsula. *J. Geophys. Res.*, **113**, https://doi.org/10.1029/2007jd008550.

Moncrieff, M. W., and T. P. Lane, 2015: Long-Lived Mesoscale Systems in a Low–Convective Inhibition Environment. Part II: Downshear Propagation. *J. Atmos. Sci.*, **72**, 4319–4336.

Mulholland, J. P., S. W. Nesbitt, and R. J. Trapp, 2019: A Case Study of Terrain Influences on Upscale Convective Growth of a Supercell. *Mon. Weather Rev.*, **147**, 4305–4324.

Munson, S. M., J. Belnap, and G. S. Okin, 2011: Responses of wind erosion to climate-induced vegetation changes on the Colorado Plateau. *Proceedings of the National Academy of Sciences*, **108**, 3854–3859.

Neff, J. C., and Coauthors, 2008: Increasing eolian dust deposition in the western United States linked to human activity. *Nat. Geosci.*, **1**, 189–195.

Pantillon, F., P. Knippertz, J. H. Marsham, and C. E. Birch, 2015: A Parameterization of Convective Dust Storms for Models with Mass-Flux Convection Schemes. *J. Atmos. Sci.*, **72**, 2545–2561.

——, ——, ——, H.-J. Panitz, and I. Bischoff-Gauss, 2016: Modeling haboob dust storms in large-scale weather and climate models. *Journal of Geophysical Research: Atmospheres*, **121**, 2090–2109.

Pielke, R. A., and Coauthors, 1992: A comprehensive meteorological modeling system—RAMS. *Meteorol. Atmos. Phys.*, **49**, 69–91.

Pierre, C., G. Bergametti, B. Marticorena, E. Mougin, C. Bouet, and C. Schmechtig, 2012: Impact of vegetation and soil moisture seasonal dynamics on dust emissions over the Sahel. *Journal of Geophysical Research: Atmospheres*, **117**, https://doi.org/10.1029/2011JD016950.

Pincus, R., E. J. Mlawer, and J. S. Delamere, 2019: Balancing Accuracy, Efficiency, and Flexibility in Radiation Calculations for Dynamical Models. *Journal of Advances in Modeling Earth Systems*, **11**, 3074–3089.

Pokharel, A. K., M. L. Kaplan, and S. Fiedler, 2017: Subtropical Dust Storms and Downslope Wind Events. *Journal of Geophysical Research: Atmospheres*, **122**, 10,191-10,205.

Potvin, C. K., K. L. Elmore, and S. J. Weiss, 2010: Assessing the Impacts of Proximity Sounding Criteria on the Climatology of Significant Tornado Environments. *Weather Forecast.*, **25**, 921–930.

Pscheidt, I., F. Senf, R. Heinze, H. Deneke, S. Trömel, and C. Hohenegger, 2019: How organized is deep convection over Germany? *Quart. J. Roy. Meteor. Soc.*, **145**, 2366–2384.

Purdom, J. F. W., 1976: Some Uses of High-Resolution GOES Imagery in the Mesoscale Forecasting of Convection and Its Behavior. *Mon. Weather Rev.*, **104**, 1474–1483.

Rabin, R. M., S. Stadler, P. J. Wetzel, D. J. Stensrud, and M. Gregory, 1990: Observed Effects of Landscape Variability on Convective Clouds. *Bull. Am. Meteorol. Soc.*, **71**, 272–280.

Reid, J. S., and Coauthors, 2023: The Coupling Between Tropical Meteorology, Aerosol Lifecycle, Convection, and Radiation during the Cloud, Aerosol and Monsoon Processes Philippines Experiment (CAMPEx). *Bull. Am. Meteorol. Soc.*, **104**, E1179–E1205.

Rieck, M., C. Hohenegger, and C. C. van Heerwaarden, 2014: The Influence of Land Surface Heterogeneities on Cloud Size Development. *Mon. Weather Rev.*, **142**, 3830–3846.

——, ——, and P. Gentine, 2015: The effect of moist convection on thermally induced mesoscale circulations. *Quarterly Journal of the Royal Meteorological Society*, **141**, 2418–2428.

Riehl, H., and J. S. Malkus, 1958: On the heat balance in the equatorial trough zone. *Geophysica*, **6**, 503–537.

Robe, F. R., and K. A. Emanuel, 2001: The Effect of Vertical Wind Shear on Radiative–Convective Equilibrium States. *J. Atmos. Sci.*, **58**, 1427–1445.

Rooney, G. G., A. J. Stirling, R. A. Stratton, and M. Whitall, 2022: C-POOL: A scheme for modelling convective cold pools in the Met Office Unified Model. *Quart. J. Roy. Meteor. Soc.*, **148**, 962–980.

Rotunno, R., J. B. Klemp, and M. L. Weisman, 1988: A Theory for Strong, Long-Lived Squall Lines. *J. Atmos. Sci.*, **45**, 463–485.

Saleeby, S. M., and S. C. van den Heever, 2013: Developments in the CSU-RAMS Aerosol Model: Emissions, Nucleation, Regeneration, Deposition, and Radiation. *J. Appl. Meteorol. Climatol.*, **52**, 2601–2622.

Saleeby, S. M., and Coauthors, 2019: The influence of simulated surface dust lofting and atmospheric loading on radiative forcing. *Atmospheric Chemistry and Physics*, **19**, 10279–10301.

Saxen, T. R., and S. A. Rutledge, 1998: Surface Fluxes and Boundary Layer Recovery in TOGA COARE: Sensitivity to Convective Organization. *J. Atmos. Sci.*, **55**, 2763–2781.

Schlemmer, L., and C. Hohenegger, 2014: The Formation of Wider and Deeper Clouds as a Result of Cold-Pool Dynamics. *J. Atmos. Sci.*, **71**, 2842–2858.

Seifert, A., and T. Heus, 2013: Large-eddy simulation of organized precipitating trade wind cumulus clouds. *Atmos. Chem. Phys.*, **13**, 5631–5645.

Seigel, R. B., and S. C. van den Heever, 2012a: Dust Lofting and Ingestion by Supercell Storms. *J. Atmos. Sci.*, **69**, 1453–1473.

——, and ——, 2012b: Simulated Density Currents beneath Embedded Stratified Layers. *J. Atmos. Sci.*, **69**, 2192–2200.

——, and ——, 2013: Squall-Line Intensification via Hydrometeor Recirculation. *J. Atmos. Sci.*, **70**, 2012–2031.

Seigel, R. B., S. C. van den Heever, and S. M. Saleeby, 2013: Mineral dust indirect effects and cloud radiative feedbacks of a simulated idealized nocturnal squall line. *Atmos. Chem. Phys.*, **13**, 4467–4485.

Simoes-Sousa, I. T., A. Tandon, J. Buckley, D. Sengupta, L. J. Sree, E. Shroyer, and S. P. de Szoeke, 2022: Atmospheric Cold Pools in the Bay of Bengal. *J. Atmos. Sci.*, **80**, 167–180.

Simpson, J. E., 1969: A comparison between laboratory and atmospheric density currents. *Quart. J. Roy. Meteor. Soc.*, **95**, 758–765.

——, 1997: *Gravity Currents*. Cambridge University Press, 244 pp.

Slingo, A., and Coauthors, 2006: Observations of the impact of a major Saharan dust storm on the atmospheric radiation balance. *Geophysical Research Letters*, **33**, https://doi.org/10.1029/2006GL027869.

Smagorinsky, J., 1963: GENERAL CIRCULATION EXPERIMENTS WITH THE PRIMITIVE EQUATIONS: I. THE BASIC EXPERIMENT. *Mon. Weather Rev.*, **91**, 99–164.

Smith, M. A., 2007: Evaluation of mesoscale simulations of dust sources, sinks and transport over the Middle East. Colorado State University, 126 pp.

Sokolik, I. N., and O. B. Toon, 1996: Direct radiative forcing by anthropogenic airborne mineral aerosols. *Nature*, **381**, 681–683.

Sokolowsky, G. A., and Coauthors, 2024: \textittobac v1.5: introducing fast 3D tracking, splits and mergers, and other enhancements for identifying and analysing meteorological phenomena. *Geosci. Model Dev.*, **17**, 5309–5330.

Souza, E. P., N. O. Rennó, and M. A. F. S. Dias, 2000: Convective Circulations Induced by Surface Heterogeneities. *J. Atmos. Sci.*, **57**, 2915–2922.

Squitieri, B. J., A. R. Wade, and I. L. Jirak, 2023: A Historical Overview on the Science of Derechos: Part II: Parent Storm Structure, Environmental Conditions, and History of Numerical Forecasts. *Bull. Am. Meteorol. Soc.*, **104**, E1734–E1763.

Stein, U., and P. Alpert, 1993: Factor Separation in Numerical Simulations. *Journal of Atmospheric Sciences*, **50**, 2107–2115.

Stensrud, D. J., M. C. Coniglio, R. P. Davies-Jones, and J. S. Evans, 2005: Comments on "'A Theory for Strong Long-Lived Squall Lines' Revisited." *J. Atmos. Sci.*, **62**, 2989–2996.

Stevens, B., and Coauthors, 2019: DYAMOND: the DYnamics of the Atmospheric general circulation Modeled On Non-hydrostatic Domains. *Prog. Earth Planet. Sci.*, **6**, 61.

Stokowski, D., 2005: The addition of the direct radiative effect of atmospheric aerosols into the Regional Atmospheric Modeling System (RAMS). Colorado State University, 81 pp.

Straka, J. M., R. B. Wilhelmson, L. J. Wicker, J. R. Anderson, and K. K. Droegemeier, 1993: Numerical solutions of a non-linear density current: A benchmark solution and comparisons. *International Journal for Numerical Methods in Fluids*, **17**, 1–22.

Sutton, L. J., 1925: Haboobs. *Quarterly Journal of the Royal Meteorological Society*, **51**, 25–30.

Tanaka, T. Y., and M. Chiba, 2006: A numerical study of the contributions of dust source regions to the global dust budget. *Glob. Planet. Change*, **52**, 88–104.

Taylor, C. M., R. A. M. de Jeu, F. Guichard, P. P. Harris, and W. A. Dorigo, 2012: Afternoon rain more likely over drier soils. *Nature*, **489**, 423–426.

Tegen, I., and I. Fung, 1994: Modeling of mineral dust in the atmosphere: Sources, transport, and optical thickness. *Journal of Geophysical Research: Atmospheres*, **99**, 22897–22914.

Tompkins, A. M., 2001: Organization of Tropical Convection in Low Vertical Wind Shears: The Role of Water Vapor. *J. Atmos. Sci.*, **58**, 529–545.

Tong, D. Q., and Coauthors, 2023: Health and safety effects of airborne soil dust in the Americas and beyond. *Rev. Geophys.*, **61**, https://doi.org/10.1029/2021rg000763.

Torri, G., Z. Kuang, and Y. Tian, 2015: Mechanisms for convection triggering by cold pools. *Geophys. Res. Lett.*, **42**, 1943–1950.

Trier, S. B., C. A. Davis, D. A. Ahijevych, M. L. Weisman, and G. H. Bryan, 2006: Mechanisms Supporting Long-Lived Episodes of Propagating Nocturnal Convection within a 7-Day WRF Model Simulation. *J. Atmos. Sci.*, **63**, 2437–2461.

Twohy, C. H., and Coauthors, 2009: Saharan dust particles nucleate droplets in eastern Atlantic clouds. *Geophysical Research Letters*, **36**, https://doi.org/10.1029/2008GL035846.

UCAR/NCAR-Earth Observing Laboratory, 2024: BioAerosols and Convective Storms. https://www.eol.ucar.edu/field_projects/bacs (Accessed December 12, 2024).

Vogel, R., H. Konow, H. Schulz, and P. Zuidema, 2021: A climatology of trade-wind cumulus cold pools and their link to mesoscale cloud organization. *Atmos. Chem. Phys.*, **21**, 16609–16630.

Wade, A. R., M. C. Coniglio, and C. L. Ziegler, 2018: Comparison of Near- and Far-Field Supercell Inflow Environments Using Radiosonde Observations. *Mon. Weather Rev.*, **146**, 2403–2415.

Wakimoto, R. M., 1982: The Life Cycle of Thunderstorm Gust Fronts as Viewed with Doppler Radar and Rawinsonde Data. *Mon. Weather Rev.*, **110**, 1060–1082.

Walker, A. L., M. Liu, S. D. Miller, K. A. Richardson, and D. L. Westphal, 2009: Development of a dust source database for mesoscale forecasting in southwest Asia. *Journal of Geophysical Research: Atmospheres*, **114**, https://doi.org/10.1029/2008JD011541.

Walko, R. L., and Coauthors, 2000: Coupled Atmosphere–Biophysics–Hydrology Models for Environmental Modeling. *J. Appl. Meteorol. Climatol.*, **39**, 931–944.

Wang, J., and Coauthors, 2009: Impact of deforestation in the Amazon basin on cloud climatology. *Proceedings of the National Academy of Sciences*, **106**, 3670–3674.

Weaver, J. F., and S. P. Nelson, 1982: Multiscale Aspects of Thunderstorm Gust Fronts and Their Effects on Subsequent Storm Development. *Mon. Weather Rev.*, **110**, 707–718.

Webster, P. J., and Coauthors, 2002: The JASMINE Pilot Study. *Bull. Am. Meteorol. Soc.*, **83**, 1603–1630.

Weckwerth, T. M., 2000: The effect of small-scale moisture variability on thunderstorm initiation. *Mon. Weather Rev.*, **128**, 4017–4030.

——, and R. M. Wakimoto, 1992: The Initiation and Organization of Convective Cells atop a Cold-Air Outflow Boundary. *Mon. Weather Rev.*, **120**, 2169–2187.

——, J. W. Wilson, and R. M. Wakimoto, 1996: Thermodynamic Variability within the Convective Boundary Layer Due to Horizontal Convective Rolls. *Mon. Weather Rev.*, **124**, 769–784.

——, ——, ——, and N. A. Crook, 1997: Horizontal convective rolls: Determining the environmental conditions supporting their existence and characteristics. *Mon. Weather Rev.*, **125**, 505–526.

——, T. W. Horst, and J. W. Wilson, 1999: An observational study of the evolution of horizontal convective rolls. *Mon. Weather Rev.*, **127**, 2160–2179.

Weger, R. C., J. Lee, T. Zhu, and R. M. Welch, 1992: Clustering, randomness and regularity in cloud fields: 1. Theoretical considerations. *J. Geophys. Res.*, **97**, 20519–20536.

Weisman, M. L., 1992: The Role of Convectively Generated Rear-Inflow Jets in the Evolution of Long-Lived Mesoconvective Systems. *Journal of Atmospheric Sciences*, **49**, 1826–1847.

——, and R. Rotunno, 2004: "A Theory for Strong Long-Lived Squall Lines" Revisited. *J. Atmos. Sci.*, **61**, 361–382.

——, J. B. Klemp, and R. Rotunno, 1988: Structure and Evolution of Numerically Simulated Squall Lines. *J. Atmos. Sci.*, **45**, 1990–2013.

Wills, S. M., M. F. Cronin, and D. Zhang, 2021: Cold pools observed by uncrewed surface vehicles in the central and eastern tropical pacific. *Geophys. Res. Lett.*, **48**, https://doi.org/10.1029/2021gl093373.

——, ——, and ——, 2023: Air-Sea Heat Fluxes Associated With Convective Cold Pools. *Journal of Geophysical Research: Atmospheres*, **128**, e2023JD039708.

Wilson, J. W., and W. E. Schreiber, 1986: Initiation of Convective Storms at Radar-Observed Boundary-Layer Convergence Lines. *Mon. Weather Rev.*, **114**, 2516–2536.

Wu, C., Z. Lin, and X. Liu, 2020: The global dust cycle and uncertainty in CMIP5 (Coupled Model Intercomparison Project phase 5) models. *Atmospheric Chemistry and Physics*, **20**, 10401–10425.

Xue, M., 2002: Density currents in shear flows: Effects of rigid lid and cold-pool internal circulation, and application to squall line dynamics. *Quart. J. Roy. Meteor. Soc.*, **128**, 47–73.

Young, G. S., S. M. Perugini, and C. W. Fairall, 1995: Convective Wakes in the Equatorial Western Pacific during TOGA. *Mon. Weather Rev.*, **123**, 110–123.

Zuidema, P., and Coauthors, 2012: On Trade Wind Cumulus Cold Pools. *J. Atmos. Sci.*, **69**, 258–280.